1-1-2013

The Rational Synthesis of Supported Noble Single Or Bimetallic Catalysts by Electrostatic Adsorption

HYERAN CHO
University of South Carolina - Columbia

The Rational Synthesis of supported Noble Single or Bimetallic Catalysts by Electrostatic Adsorption

by

Hye-Ran Cho

Bachelor of Engineering
Chung-Ang University, 2003

Submitted in Partial Fulfillment of the Requirements

For the Degree of Doctor of Philosophy in

Chemical Engineering

College of Engineering and Computing

University of South Carolina

2013

Accepted by:

John R. Regalbuto, Major Professor

John R. Monnier, Committee Member

Miao Yu, Committee Member

Douglas Blom, Committee Member

John W. Weidner, Committee Member

Lacy Ford, Vice Provost and Dean of Graduate Studies

DEDICATION

I dedicate this thesis to my parents for raising me as an independent and enthusiastic woman with countless love and affection. They never say no whenever I want to discuss about my future with them and always encourage me not to afraid my choice.

I also dedicate this thesis to my lovely friends and colleagues at UIC and at USC. I would not handle lonely PhD student life without them. Especially my old friends (Siyeon and Jungeun), they had given me a dream and never stop cheer me up until I achieve it.

I would like to thank to Shin who support my dreams all the way and makes me happy smile.

ACKNOWLEDGEMENTS

First of all, I am earnest grateful to my advisor, Dr. John R. Regalbuto, for guide me to achieve my dream.

I wish to express my sincere thanks to committee members; Dr. John. R. Monnier, Dr. Miao Yu, Dr. John W. Weidner and Dr. Douglas Blom,

I place on record, my sincere gratitude to Johnson Matthey Technology Centre at UK for supporting my chapter 3 work of this thesis and evaluating my Pt-Pd bimetallic catalysts.

I also thank Dr. Hutchings group in Cardiff University at UK for the reaction work of benzyl alcohol oxidation and Steven A. Bradley in UOP Honeywell for STEM images of Au-Pd bimetallic catalysts.

I am extremely grateful and indebted to Ke-Bin Low in RRC at UIC who suffered to catch the good images of tiny particles of my Pt-Pd bimetallic catalysts and finally got sick.

ABSTRACT

Many catalysts are today prepared by impregnation (also called incipient wetness or dry impregnation) in which nominal amounts of metals are placed into the amount of solution just necessary to fill the pore volume of the support material. While dry impregnation (DI) is simple and the amounts of metals easily controlled, no attention is paid to metal-support or metal-metal interaction. When DI-deposited metal precursors are reduced, the particles tend to be large in size and there is often ppor contact between two metals in a bimetallic system. In this work we demonstrate the application of "strong electrostatic adsorption" (SEA) for the rational synthesis of inorganic metallic catalysts with high metal dispersion and intimate metal1-metal2 interaction of bimetallic catalysts. For monometallic catalysts, we suggested charge-enhanced dry impregnation (CEDI) which can produce highly dispersed single metal catalysts by inducing electrostatic interaction between dissolved precursor and support while using a simple DI method.

Two variations will be demonstrated that produce bimetallic catalysts: using simultaneous or co-SEA, two metal precursors are simultaneously placed in solution and electrostatically adsorbed onto a support in a mixed monolayer of precursors. This produces homogeneously alloyed bimetallic particles when the precursor layer is reduced. On the other hand, SEA can be applied in a two step sequence (seq-SEA); the core metal precursor is electrostatically adsorbed onto the support and oxidized, and then the shell metal precursor is selectively adsorbed onto the core metal oxide and not onto the support.

A core-shell morphology persists after the reduction step.

Pt/Pd bimetallic catalysts supported by oxidized and unoxidized carbon, alumina and silica have been synthesized by co-SEA. Seq-SEA has been used to produce Pd cores/Pt shell (Pd@Pt) on silica and alumina, and Pt cores/Pd shell (Pt@Pd) on alumina. These are compared with DI-prepared catalysts of the same nominal composition. Seq-SEA can also produce well-dispersed uniform Pd@Au catalysts for Benzyl alcohol oxidation. Catalysts synthesized using this method, have 10 times the activity of comparable DI-prepared catalysts, while using 25 times less gold. The materials were characterized by powder XRD, STEM, EDXS nanoparticle mapping, and TPR. Au/Pd/C catalysts were evaluated by benzyl alcohol oxidation reaction at Cardiff University, England.

TABLE OF CONTENTS

LIST OF TABLES

LIST OF FIGURES

CHAPTER 1

INTRODUCTION

Catalytic processes are of great importance to the economy of many industrialized nations. The majority of products and goods we use in daily life contain compounds that have at some point in their production life cycle been in contact with a catalyst. Seventy percent of all commercial chemical processes involve some catalytic application [1]. A few of the more common applications of catalytic processes include water treatment, air pollution control (for example, automotive exhaust catalysis) and many processes in the petroleum industry. The common methods of industrial catalyst preparation are to a large degree based on experience rather than fundamental understanding of the processes involved, and are oftentimes referred to as an art. It is the primary objective of this study to help build a fundamental understanding of supported metal catalyst preparation, in other words, to turn the art of catalyst preparation into a science.

1.1 PREPARATION OF SUPPORTED METAL CATALYSTS

There are a multitude of catalyst preparation methods, such as impregnation, co-precipitation, deposition-precipitation, sol-gel, chemical vapor deposition, etc. Among all these catalyst preparation methods, impregnation is the simplest, least expensive, and most prevalent method, in which a high surface area oxide or carbon support is contacted with a liquid solution containing precursor dissolved metal ions or coordination complexes. After impregnation, various drying and pretreatment steps can be employed

to remove the metal ligands and to reduce the metal to its catalytically active metallic state. About 30% of literatures of 3 biggest catalysis research centers in USA still used an impregnation method for within the last 5 years.

Impregnation methods can further be divided into dry impregnation and wet impregnation. Dry impregnation is often termed “incipient wetness impregnation (IWI)” or “pore filling”. In wet impregnation (WI), the support material is contacted with an excess of a solution containing the metal precursor, the metal precursor species may or may not diffuse into the pore system of the solid during the equilibration period, in only some cases, leading to homogeneous distribution of the metal throughout the support. In contrast, in the incipient wetness impregnation technique an amount of solution that corresponds to the total pore volume of the support material is mixed with support and capillary action provides the driving force for the imbibition of the impregnation solution into the porous solid. However, a non-uniform metal precursor distribution may develop as the metal complex remains in solution and is carried to the surface during drying. In neither IWI nor WI is any provision made for interaction of the metal precursor with the support surface.

1.2 STRONG ELECTROSTATIC ADSORPTION

In the above methods, pH is generally not controlled, and the final pH of the impregnation solution can vary quite dramatically. If the metal solution is adjusted before contact, for example by adding acid or base so as to promote metal sorption onto the support, the concept of “strong electrostatic adsorption (SEA) method” can be introduced. In this case the interaction between the charged metal complex and the support is strong electrostatic adsorption.

The electrostatic mechanism had been postulated for catalyst preparation in the land mark paper of Brunelle [2] and the pioneering work of Schwarz [3-6]. As depicted in Figure 1.1, hydroxyl groups on the surface of an oxide can be protonated or de-protonated depending on the pH of the contacting solution. The pH at which the hydroxyl groups are neutral and no precursor-support interaction occurs is termed the point of zero charge (PZC) [7]. Below the PZC, the hydroxyl groups protonate and become positively charged, and the surface can adsorb anionic metal complexes such as PHC ($[PtCl_6]^{2-}$). Above the PZC, the hydroxyl groups de-protonate and become negatively charged, and the cations such as PTA ($[(NH_3)_4Pt]^{2+}$) can be strongly adsorbed. In both case, the metal complex deposit onto the surface via strong electrostatic adsorption (SEA).

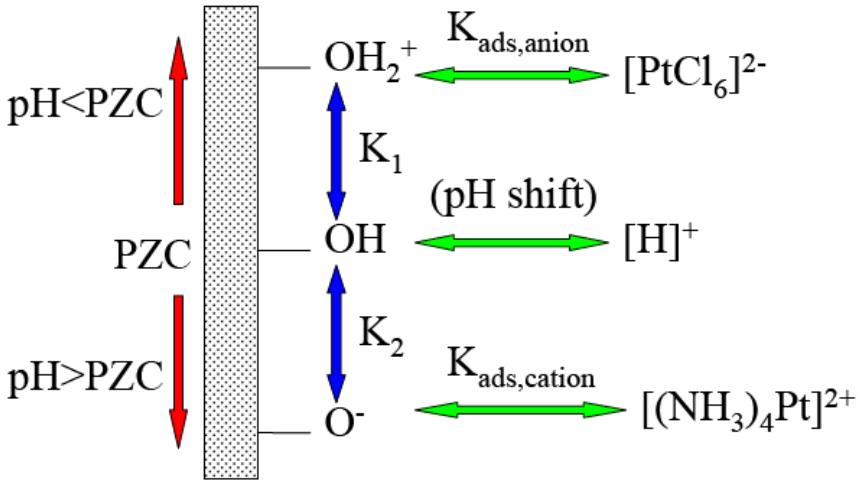

Figure 1.1 Electrostatic adsorption mechanism

The first step in the SEA method is to determine the PZC of the support, which is easily determined by measuring final pH versus initial pH at high surface loading. Surface loading (SL) is defined at the amount of support surface per liter of solution, and can be calculated by equation 1.

$$\text{Surface loading } (m^2/L) = \frac{\text{Surface Area of support } \left(\frac{m^2}{g}\right) * \text{grams of support(g)}}{\text{Volume of Precursor Solution (L)}} \qquad \text{(eqn 1)}$$

The second step of SEA is to perform an uptake-pH survey to determine the pH of strongest interaction. The overriding hypothesis of the SEA approach is that with metals, the simplest and most effective way to synthesize highly dispersed metal particles is to achieve a high dispersion of the metal precursors on the support during impregnation. Once strongly adsorbed, the idea is to perform the pretreatment steps of calcinations or reduction, often referred to in industry as catalyst finishing, in such a way that the monolayer morphology of the precursor is maintained as the metal is reduced, such that high metal dispersion is achieved [8,9].

Our research group has proposed a parameter-free Revised Physical Adsorption Model (RPA) based on a purely physical adsorption scheme, as opposed to a chemical mechanism [11]. The pH shift model was put forward by Park and Regalbuto [7], who were the first to simulate the pH shifts in bulk solution which occur when aqueous solutions are contacted with various amounts of oxides. This model was proposed as a simple and novel technique to determine the PZC of oxides. This PZC measurement method differs from traditional titration experiments in that the initial solutions of varying pH are contacted with oxides at various surface loadings. The equilibrium pH of the solution is then measured. Thus the model predicts the pH buffering effects of oxides at specific surface loadings. Figure 1.2 illustrates the pH shift and adsorption calculations for the uptake of PHC on alumina as a function of surface loading, which

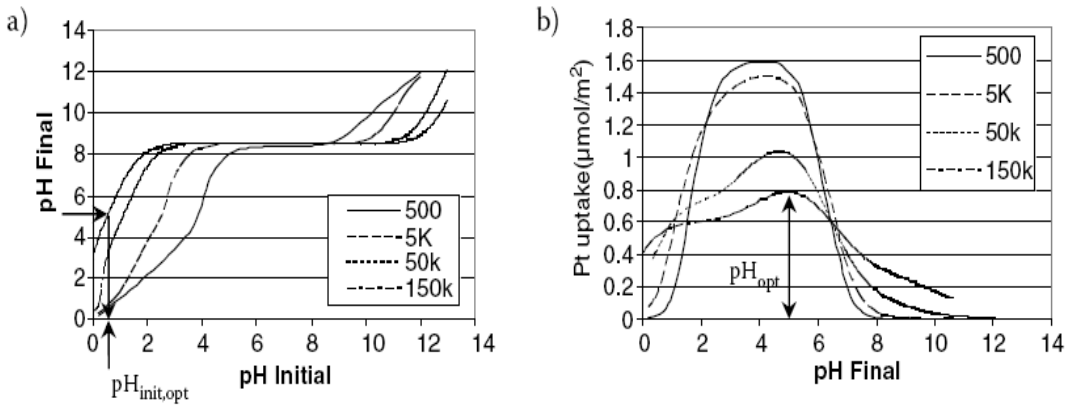

Figure 1.2 Simulation of SEA at high surface loadings (a) pH shift simulation, (b) uptake-pH simulation [20]
is the area of support per volume of solution.

From the pH shift plot in figure 1.2a, the plateaus of final pH are seen to widen at higher surface loading. Uptake curves figure in 1.2b, at all SLs, show a typical characteristic of SEA, being a volcano shape in metal uptake. An optimal pH exists at which point has the strongest electrostatic attraction. This occurs far enough from the PZC so that the surface is strongly charged. The maximum obtainable uptake decreases at the highest SL due to the higher concentration of Pt, which must be employed to achieve the same surface density. It also decreases at extremely acidic (and basic) pH when the ionic concentration of the solution is high which causes the adsorption equilibrium constant to become very small due to electric double layer screening.

The RPA model shows different adsorption survey curve depended on different PZC support materials (Figure1.3).

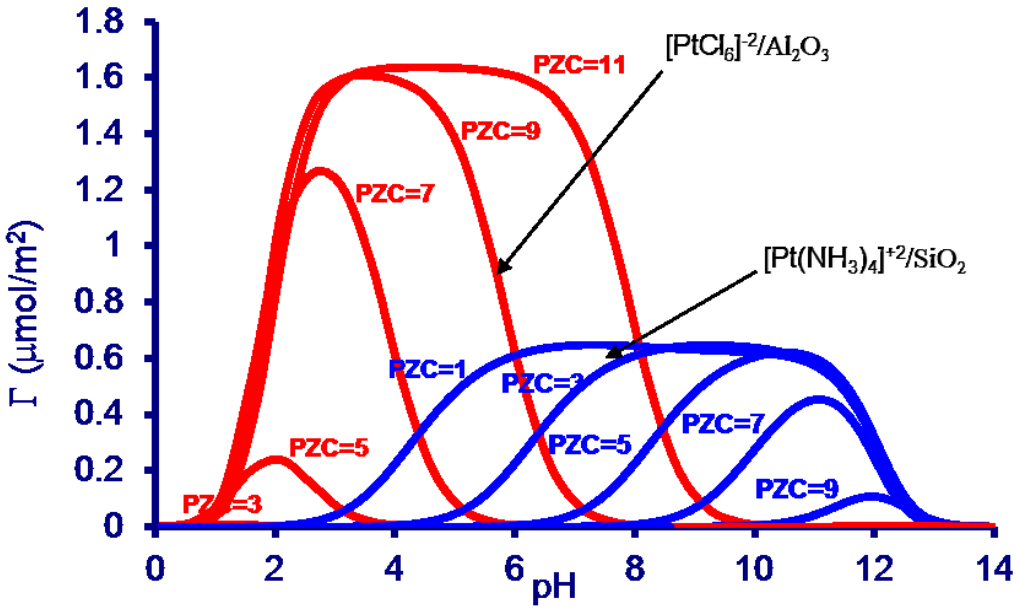

Figure 1.3 RPA simulation of Pt adsorption over supports with different PZC [10]

Supports with very low PZC have a broad PTA adsorption plateau from the PZC to pH12 since it has electrostatic potential just after the PZC [11]. Maximum adsorption density of PHC is double that of PTA because PHC is assumed to have one hydration sheath, and PTA two.

1.3 EXTENSION OF THE SEA APPROACH TO BIMETALLIC CATALYSTS

The SEA method can be applied to the synthesis of bimetallic catalysts by exploiting the difference in surface charging parameters of a composite surface. If a low PZC support is supporting a high PZC oxide, in the acidic pH range the density of the protonated hydroxyl groups on the high PZC oxide will be greater than that of the low PZC oxide. The first metal might itself may be deposited by SEA in well-dispersed form by precursors such as cationic cobalt hexaammine on silica. Next the second metal complex, such as $[PtCl_6]^2$, should selectively adsorb to the cobalt oxide rather than silica (figure 1.4).

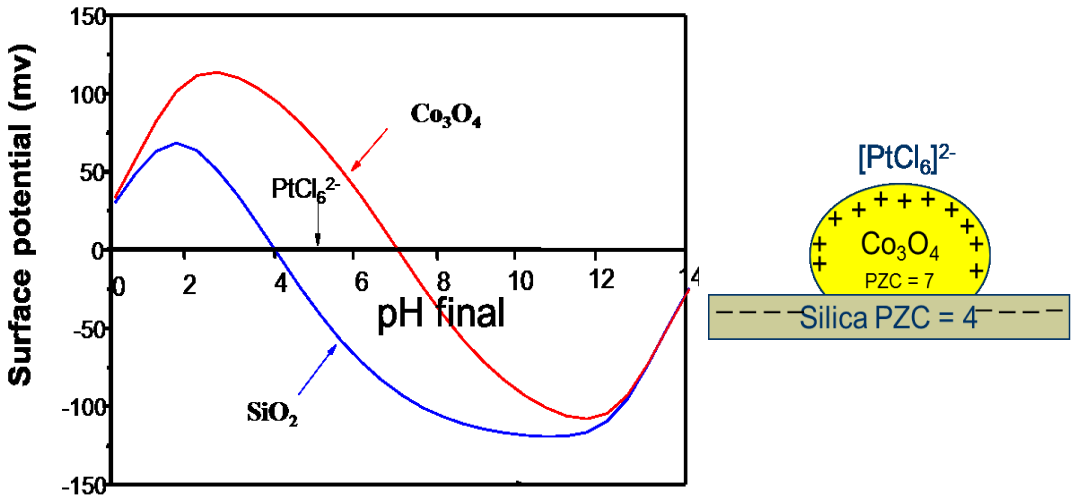

Figure 1.4 Schematic of proposed selective adsorption

Pioneering research began with Schwarz et al. [3-6] and their attempt to selectively adsorb Co^{2+} or Pd^{2+} onto one of two composite oxides. Unfortunately, their choice in using bare metal ions as their precursor introduced problems in that these species tend to hydrolyze and precipitate over a wide pH range. This can be circumvented by using metal ammine, chloride or oxide coordination complexes as the precursor. These metal precursor compounds are generally stable over a broad range of pH and concentration.

This work will apply the rational synthesis of single and bimetallic catalysts by electrostatic adsorption. In chapter 2, I will demonstrate a hybrid synthesis method we have termed "charge-enhanced dry impregnation (CEDI)" as a simple method to prepare highly dispersed monometallic Pt catalysts by inducing electrostatic interaction between support and metal precursor. Chapter 3 will show my work at Johnson Matthey Technology Centre (JMTC) for measurement of PZC of noble metal (NM) oxides and adsorption surveys of NM precursors onto NM oxides. Chapter 4 will describe the synthesis of several sets of Pt/Pd bimetallic catalysts with oxides or carbon support by

simultaneous SEA and sequential SEA. The final chapter will utilize seq-SEA to synthesis Au-Pd/carbon catalyst for benzyl alcohol oxidation.

CHAPTER 2

SUPPORTED PLATINUM CATALYSTS PREPARED BY DI AND CEDI

Dry impregnation (also called pore filling or incipient wetness) is the simplest, least expensive, and most prevalent way to prepare supported metal catalysts. In this method a desired amount of metal precursor, typically a coordination complex such as platinum hexachloride (PHC, $[PtCl_6]^{-2}$) or platinum tetraammine (PTA, $[(NH_3)_4Pt]^{-2}$), is dissolved in water and the solution added to an oxide or carbon support in the amount just sufficient to fill the pore volume of the support. The thick slurry/paste is dried and then heated in oxidizing and/or reducing gases to remove the ligands of the precursor and to reduce the metal to its active elemental state. This method requires no filtration, eliminates wasted metal and yields a precise metal loading. The most common catalysis metric of metal utilization is dispersion: the fraction of metal atoms appearing at the surfaces of metal crystallites (and available as catalytically active sites), divided by the total number of atoms. Metal nanoparticles one nanometer in diameter have a dispersion of approximately 100%; high dispersion is very often the goal of synthesis.

In dry impregnations no provision is made for the metal precursor complexes to interact with the support surface, and without such interaction, metal complexes agglomerate into large particles either before or during reduction. Unlike supported metal oxides, which can be easily dispersed on oxide supports by thermal spreading from mixtures of bulk oxide powders [12], obtaining high dispersion of supported

metals requires high dispersion of metal precursors.

Precursor - support interactions in many common catalyst preparations can be envisioned in light of the electrostatic adsorption mechanism [2-6] depicted in figure 1.1. Oxide and carbon surfaces terminate in functional groups such as hydroxyls and carboxylic acids which can protonate or deprotonate as a function of solution pH. At these conditions the surface can electrostatically adsorb precursors of opposite charge; anions adsorb over a protonated surface below the PZC, cations over a deprotonated surface above the PZC.

While it is easy to understand electrostatic adsorption as a function of pH in figure 1.1, appreciating the extent of proton transfer in dry impregnation is much less intuitive. Consider, for example, impregnating a typical alumina with a surface area 200 m^2/g, pore volume 1.0 ml/g and a hydroxyl density of 8 OH/nm^2, with a pH 3 solution. This is five pH units below alumina's PZC of about 8.5; it may be assumed that the low pH solution will protonate the surface and enable adsorption of anions per figure 1.1. The number of protons in 1.0 ml (1.0×10^{-3} L) of pH 3 (10^{-3} molar) solution is 1.0×10^{-6} moles. The number of hydroxyl groups on the surface of one gram of alumina support is

$$1\ g \times 200\ m^2/g \times 1018\ nm^2/m^2 \times 8\ OH/nm^2 \times 1\ mole/(6.02 \times 10^{23}\ OH)$$

$$= 2660 \times 10^{-6}\ moles.$$

With only 1/2660 hydroxyl groups protonated, the surface will be negligibly charged. Enough acid in 1.0 ml of solution to protonate all the surface OH groups would require a concentration of 2.67 mol H/L, or an initial pH of -0.41.

The strong buffering capacity of oxide surfaces at incipient wetness has been pointed out in the past [13]; at this condition the final pH of impregnating solution is

almost always at the PZC of the surface and no electrostatic metal precursor - support interaction occurs unless the impregnation solution is made extremely acidic or basic.

2.1 EXPERIMENTS

2.1.1 Catalysts Preparation

Oxidized carbon (Darco G-60, BET area: 617 m^2/g) and SiO_2 (BET area: 330 m^2/g) were used as low PZC supports with which platinum tetraammine (PTA, $[Pt(NH_3)_4]Cl_2$, 99.9%) was used as the precursor. Sodium tetrachloroplatinate(ll) (PTC, Na_2PtCl_4 nH_2O, 99.9%) from Aldrich were used as the platinum precursor on the high PZC support, a gamma-alumina (BET area: 274 m^2/g) support.

The water accessible pore volume was measured with one gram of oxide and deionized water (pH of 5.6). pH measurements at incipient wetness were made with a spear tip combination pH probe.

DI samples were prepared by adding metal precursor solution for 2 wt% Pt loading. The pastes were dried at room temperature in air and then reduced in hydrogen for 1 hr at 200°C. The same process was used to prepare CEDI samples, with the exception that optimal initial pH values were used (as described later).

2.1.2 Catalysts Characterization

BET surface area measurements were obtained using an automated adsorption system (ASAP, 2100, Micromeritics). After degassing at 150ºC, the samples were transported from degassing port to analysis port and doping with N_2 in liquid nitrogen pool. Surface area were calculated by the linear relation between P/Po and 1/ [v(P/Po-1)] with 8 points from 0~0.35 of P/Po values.

Powder X-ray diffraction analysis was performed using a Siemens D5000

diffractometer with Cu Kα radiation (λ = 1.5406 Å) operated at 30kV and 40mA, operating in Bragg–Brentano geometry. Scans were made in the 10^o-90^o 2θ range, with step size of 0.02^o, and 2s exposure at each step. Z-contrast STEM imaging for particle size determination in the materials was conducted with a JEOL JEM-2010F FasTEM with a probe size of 0.14-0.2 nm. The catalyst samples were sonicated in isopropanol for 15 min and the slurry was deposited onto a carbon-coated copper grid (200 mesh, Cu PK/100), supplied by SPI, USA. The applied voltage was 200 kV and extracting voltage of 4500 V. Approximately 500 particles were counted for size distribution. Carbon monoxide chemisorption was used to determine the accessible Pt surface using a Micromeritics ASAP 2020 instrument. The samples were first dried at 110 °C in a He flow for 30min and subsequently reduced in a 50% H_2/He flow at 350 °C for 2 h (ramp = 10°C/min).

Carbon monoxide chemisorptions was used to determine the accessible Pt surface (Micromeritics ASAP 2020). The samples were first dried at 110 °C in a He flow for 30min and subsequently reduced in a 50% H_2/He flow at 350 °C for 2 h (ramp = 10°C/min).

2.2 RESULT

The amount of acid or base needed to sufficiently charge a surface at incipient wetness, and the effect of the high concentrations of acid and base on metal precursor uptake, can be estimated with the revised physical adsorption (RPA) model [7].

The simulation for PHC adsorption over alumina is given in figures 2.1a (potential) and 1b (uptake) at various values of a parameter we call “surface loading,” with units m^2/L.

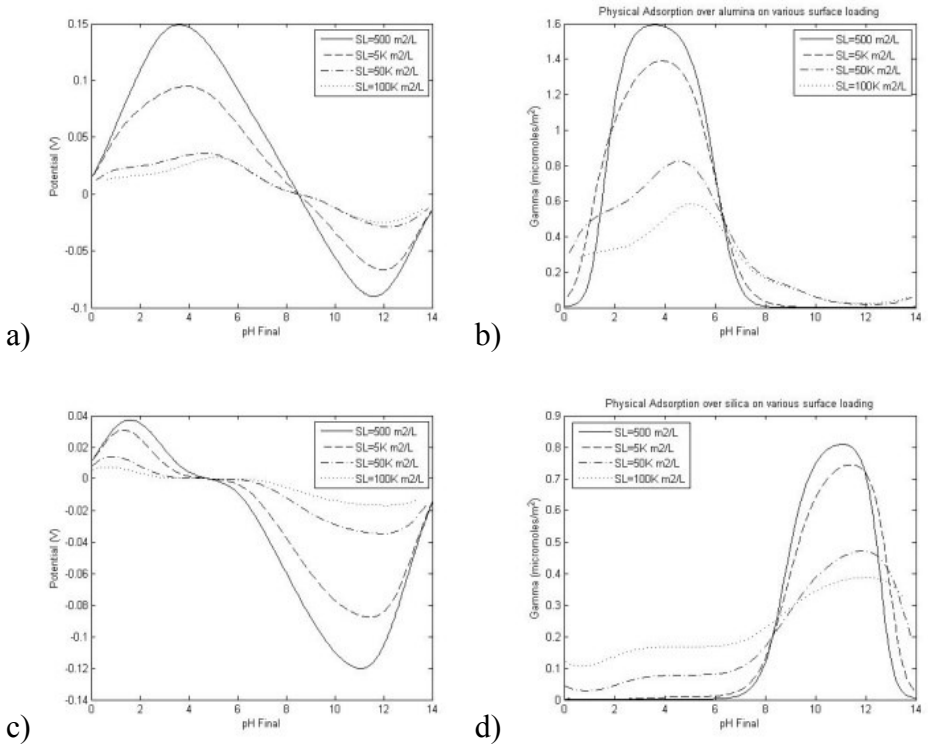

Figure 2.1 Simulation of SEA at high surface loadings; (a) alumina surface potential (b) PHC uptake (PHC adsorption, PZC 8.5, dpk=5 and Ns= 8 OH/nm^2) (c) silica surface potential (d) uptake (PTA adsorption, PZC= 4.8, dpk=8 and Ns= 8 OH/nm^2) [14]

For any value of surface loading, surface potential and metal uptake are zero at the PZC of 8.5. As the pH decreases, uptake initially increases as the surface potential rises, but at the pH extreme, high ionic strength drastically diminishes the adsorption equilibrium constant by electric screening [3-5]. Thus metal uptake is a volcano-shaped curve and there exists an optimal pH at which adsorption is strongest. An analogous set of potential and uptake curves are seen for PTA uptake over silica in figures 2.1c and 1d.

Now we consider the effect of surface loading. Thin slurries and correspondingly low surface loadings are convenient for laboratory studies, as low loadings minimize the pH shifts from buffering and make it easy to sample the liquid phase for pH and metal concentration. Most of our studies of "strong electrostatic adsorption" (SEA) [15-19] have employed surface loadings of 500 - 1000 m^2/L.

There is no reason why electrostatic SEA cannot be employed at higher surface loadings with incipient wetness representing the highest obtainable surface loading for a particular solid. In figure 2.1 it is seen that for both alumina and silica, surface potential and metal uptake decrease as surface loading is increased. This decrease is again the result of high ionic strength caused by the balancing electrolytes from the higher concentrations of metal and acid or base. Nonetheless, the simulations predict a final pH at which electrostatic adsorption is strongest at high surface loading.

The new method is illustrated in figure 2.2. SEA has traditionally featured the thin slurry/low surface loading depicted in figure 2.2, with pH controlled to the optimal value. (The more general case of "wet impregnation" would be that employing excess solution, but without controlling pH; solution pH still tends greatly to the PZC [13].)

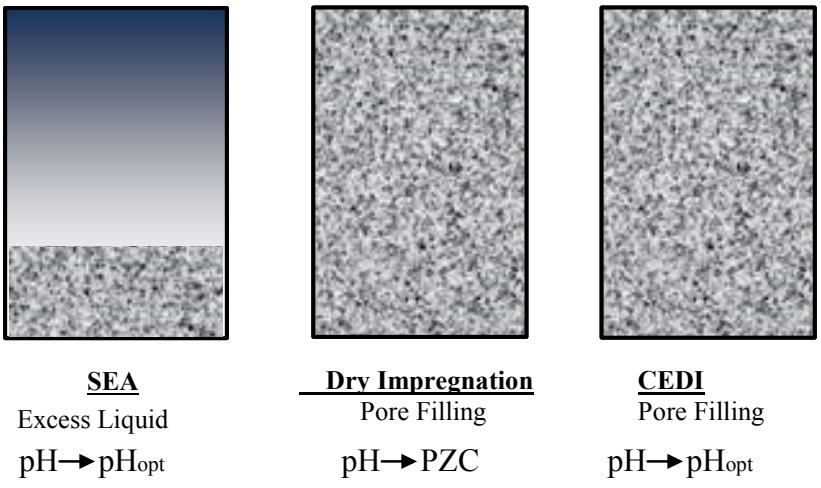

Figure 2.2 Illustration of a)SEA, b) DI, and c) CEDI impregnations.

Dry impregnation has no excess solution and the pH is almost always at the PZC (figure 2.2b). However, with enough acid or base, final pH can be taken to the optimal value. We call this "charge-enhanced dry impregnation" (CEDI) (figure 2.2c).

We have demonstrated CEDI for improving metal dispersion with three catalyst supports and two metal complexes. Table 2.1 gives the properties of these materials. For the oxidized carbon and silica surfaces that have low PZC, cationic PTA was chosen as the metal precursor, and for alumina, which has a high PZC, the anionic PTC complex was used.

Table 2.1 Properties of Supports

Supports	BET Surface area (m^2/g)	Pore Volume (ml/g)	PZC	Optimal pH (Final pH)
Carbon	617	1.46	1.5	11
SiO_2	330	0.55	3.9	11
Al_2O_3	274	1.85	8.3	3

STEM analysis was performed on the supported 2wt% Pt catalysts after impregnation, drying, and reduction at 200^{o}C for 1 hour at a ramp rate of 5^{o}C/min. Figure 2.3 shows the respective Z contrast STEM images for synthesis by DI and CEDI and particle sizes with standard deviations are given in table 2.2. The average size of nanoparticles prepared by CEDI are 1.5 nm for carbon, 1.8 for silica, and 2.9 for alumina, and are much smaller particles than those prepared by DI, 10.3, 10, and 10 nm, respectively.

Particle size was also characterized by powder XRD; these results are shown in figures2.4a, b, and c for carbon, silica and alumina, respectively. The upper diffractogram of each set is the pure support. Peaks at 21, 22.5 and 27^o 2θ in figure 2.4a can be assigned

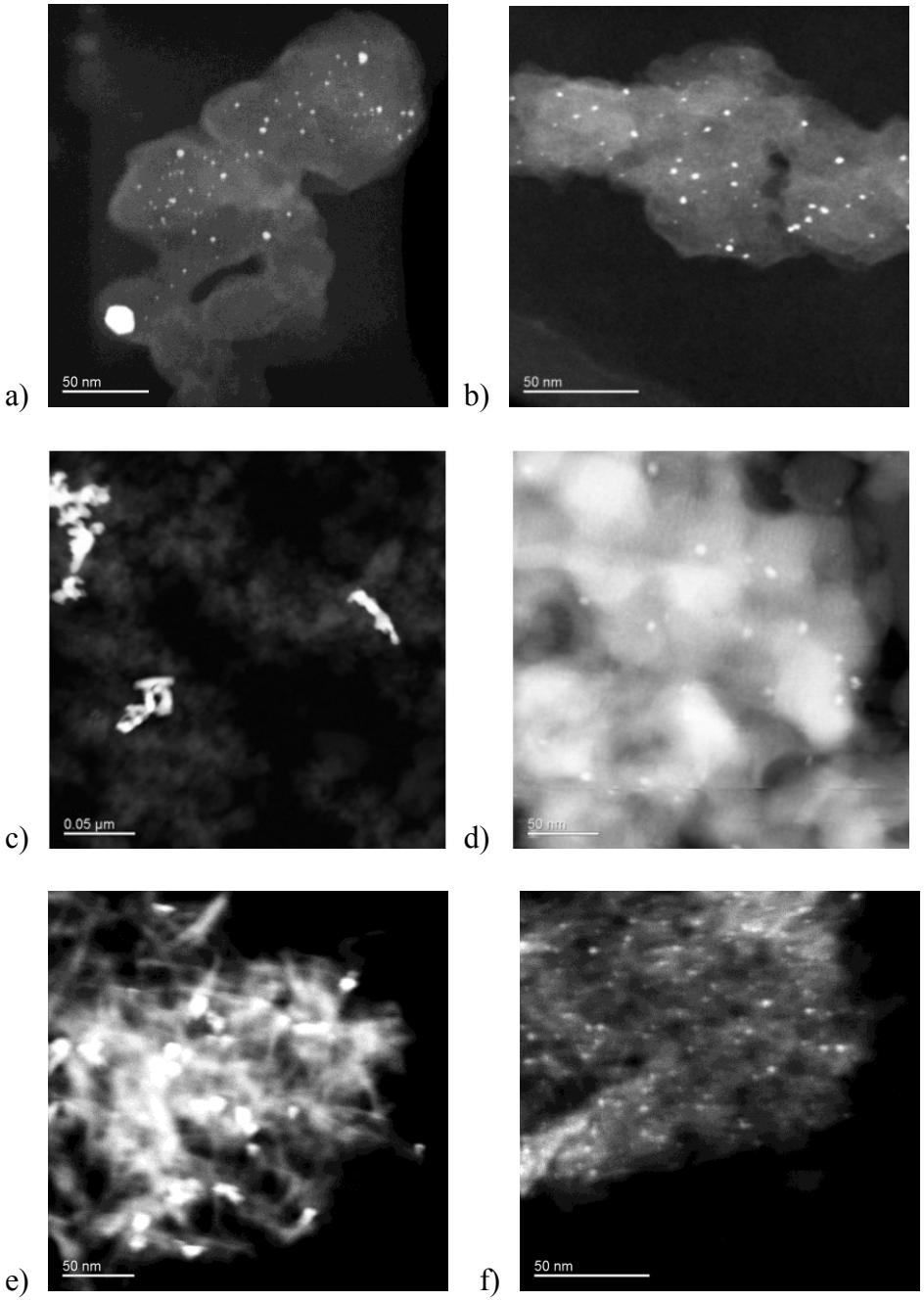

Figure 2.3 STEM image of Pt catalysts after reduced at 200°C (a) Pt/C DI (b) Pt/C CEDI (c) Pt/SiO_2 DI (d) Pt/SiO_2 CEDI (e) Pt/Al_2O_3 DI (f) Pt/Al_2O_3 CEDI

to graphite. After reduction, the Pt on carbon by DI clearly shows fcc Pt with peaks at at 39.7° 2θ (111), 46.2° (200), and 67.4° (220). For the CEDI sample, the small peak at 33.02° 2θ suggests the presence of PtO_2 (from the (110) plane). It is known that the

smallest Pt nanoparticles spontaneously oxidize [94]. The absence of significant Pt peak intensity results from small average particle size. In figure 2.4b, on silica the DI sample again clearly exhibits metallic Pt, and again in the CEDI sample only PtO_2 peaks of lower intensity are seen.

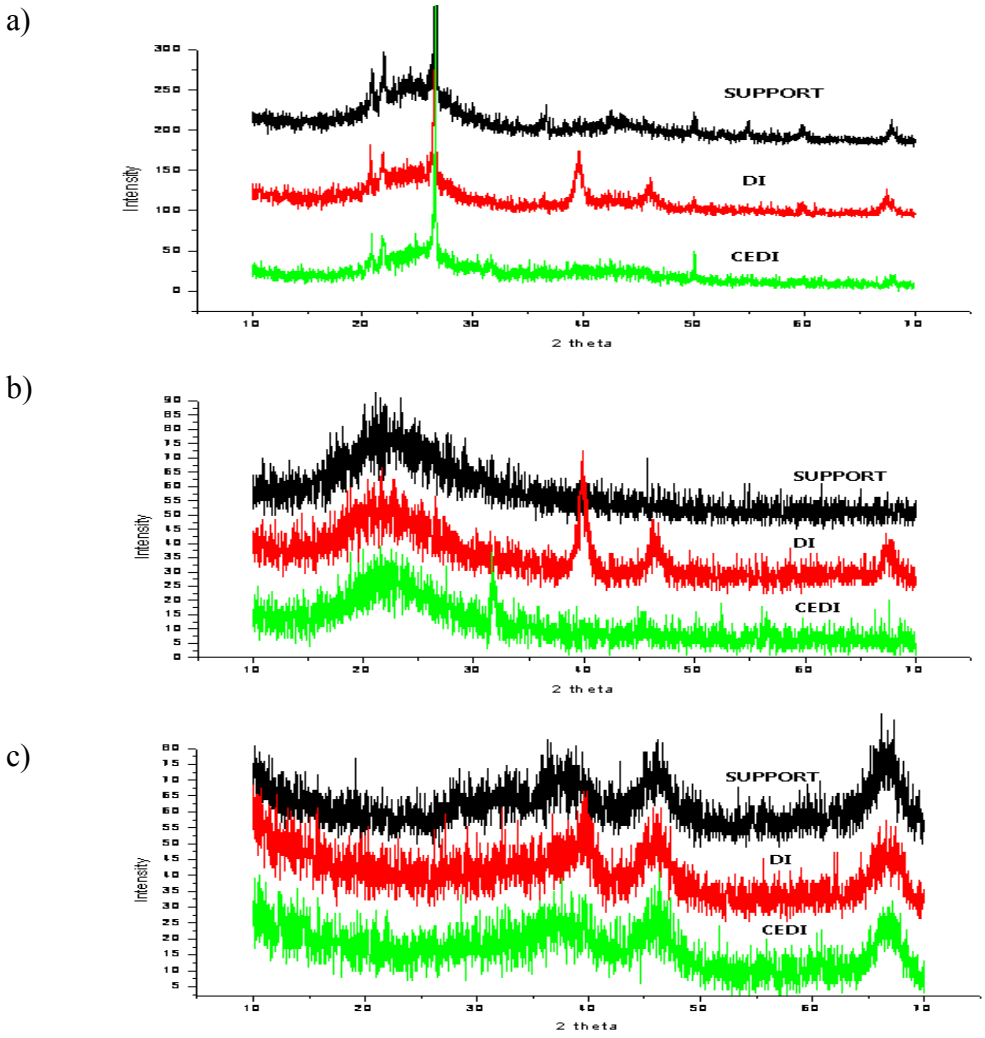

Figure 2.4 XRD pattern of a) Pt/C, b) Pt/SiO_2 and c) Pt/Al_2O_3, which prepared by DI and CEDI reduced at 200 ^oC

In figure2.4c, fcc Pt peaks overlap the Al_2O_3 support peaks but the Pt(111) peak at 39.7^o 2θ for the DI sample is still noticeable, while no Pt peaks are observed for the CEDI sample. Pt particle sizes estimated from the Scherrer equation are given in Table

2.2 for comparison with the STEM results, especially the XRD value for the Pt/Al_2O_3 sample is rough given the poor signal/noisy ratio.

Table 2.2 Final pH and particle size analysis for DI and CEDI samples

	Pt/C DI	Pt/C CEDI	Pt/SiO_2 DI	Pt/SiO_2 CEDI	Pt/Al_2O_3 DI	Pt/Al_2O_3 CEDI
pH_{final}	(1.5)	11.0	(3.9)	11.0	(8.3)	3.0
XRD[a]	14.1	<3	7.7	<3	7.9	<3
STEM[a]	10	1.8	7.5	1.5	11.2	2.9
STEM[b]	10%	56%	9%	34%	13%	67%
CO Chem.[c]	2%	21%	7.6%	71%	32%	56%

[a] reduced at 200°C, particle size (nm)
[b] dispersion based on STEM analysis
[c] reduced at 350°C, dispersion based on CO chemisoprtion

Results of CO chemisorption are also included in table 2.2. A reduction of 350°C was employed so that for the alumina sample all residual chloride would be removed. The CEDI samples for each support exhibited higher CO uptake compared to the DI samples, although the agreement between chemisorption-estimated particle sizes (size in nm = 1/dispersion) is only semiquantitative compared to the XRD and STEM values. The latter two sets of particle sizes are in reasonable agreement.

2.3 DISCUSSION

The key to obtaining maximum metal dispersion with a dry impregnation synthesis procedure is to anticipate the initial pH needed for the impregnating solution. By sufficiently acidifying or basifying the solutions, for a high PZC or low PZC support, respectively, electrostatic adsorption can be achieved.

A potential concern when working with highly acidic or basic solutions is the dissolution of the support at pH extremes. It should be noted, however, that pH equilibration is relatively rapid, typically on the order of minutes, and the support surface will quickly buffer the pH up or down to levels at which the certain charge is high enough for the strong electrostatic adsorptions, but moderate enough so that no dissolution occurs. In practice, the dropwise or sprayed application of the solution with reasonable mixing of the support should prevent significant support dissolution.

Electrostatic adsorption has been shown to occur over a wide variety of oxides and carbon support materials [21,22]. In many cases, it is the sole adsorption mechanism or it can occur in the conjunction with other mechanism such as ion exchange and deposition [23]. CEDI can be generalized to all materials by employing the RPA model to anticipate the correct initial pH necessary for a particular support material. What needs to be known are the support PZC, which is easily found with pH shift measurements [24,25], the BET surface area, and the water-accessible pore volume which can be done with a quick water titration. The latter two properties determine the surface loading at dry impregnation, where

$$\text{SL } (m^2/L) = \quad [\text{BET surface area } (m^2/g)]/[\text{pore volume } (L/g)]$$

Once the PZC and surface loading of the impregnation system are known, the RPA model, which predicts both pH shifts and metal uptake, can be consulted for the proper selection of initial pH. In figure 2.5 are presented pH shifts and metal uptakes for a range of PZC materials from 2 to 12 (figures 2.5a-f). Over the low PZC materials (2, 4, and 6 in figure 2.5a, b, and c), representative of niobia, silica, and anatasetitania, a cationic

complex such as PTA, $[(NH_3)_4Pt]^{2+}$, would be chosen as precursor. Over high PZC supports (PZCs 8, 10, and 12 are representative of alumina, carbon black, and magnesia) an anion such as PHC, $[PtCl_6]^{2-}$, should be chosen.

a)

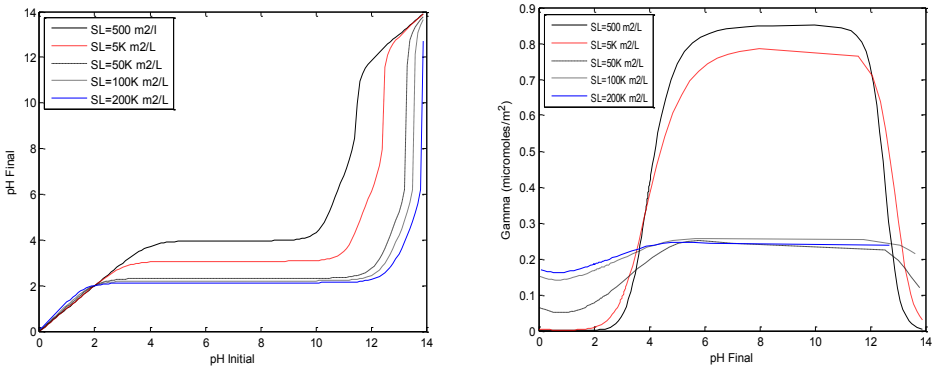

b)

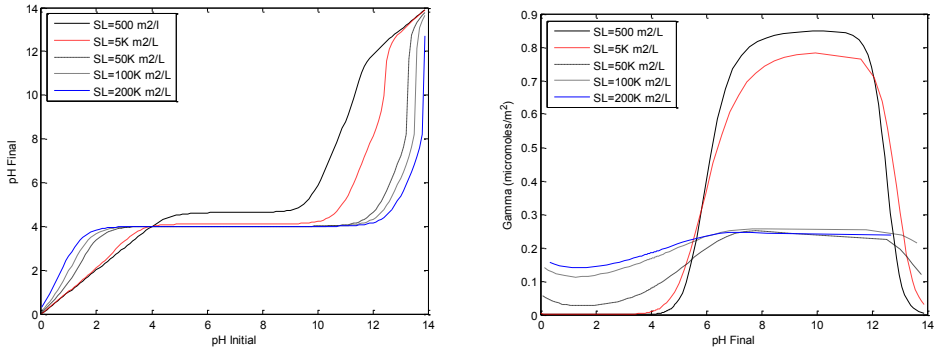

c)

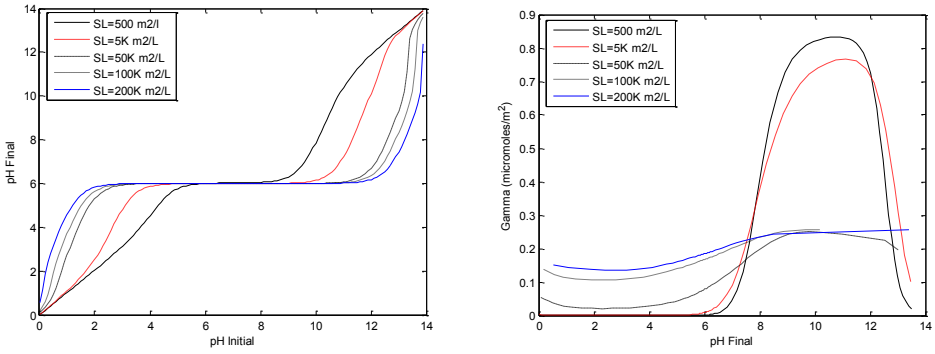

d)

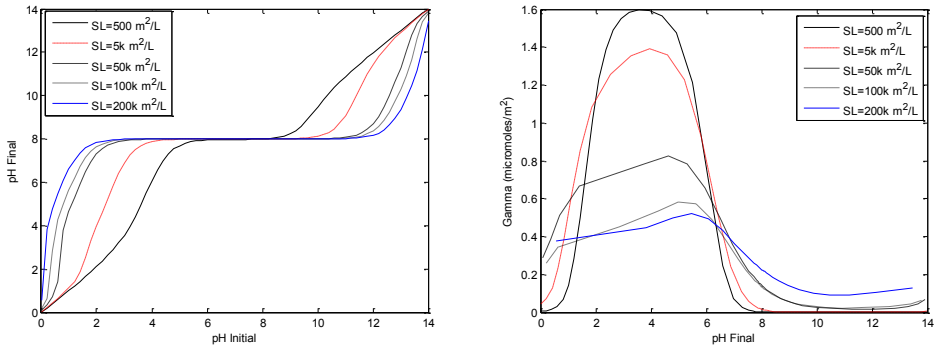

e)

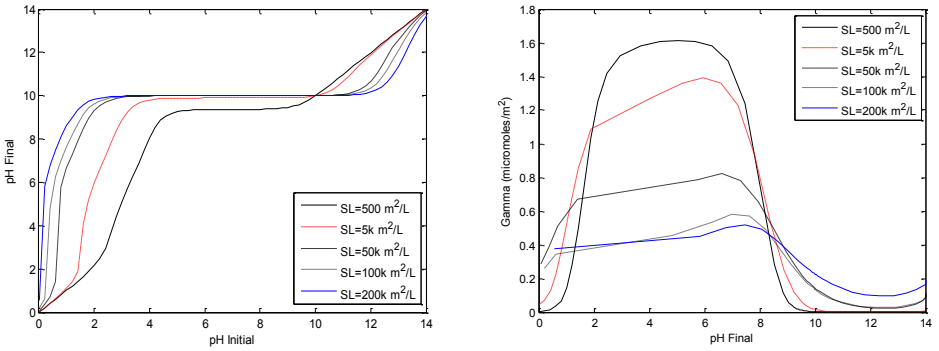

f)

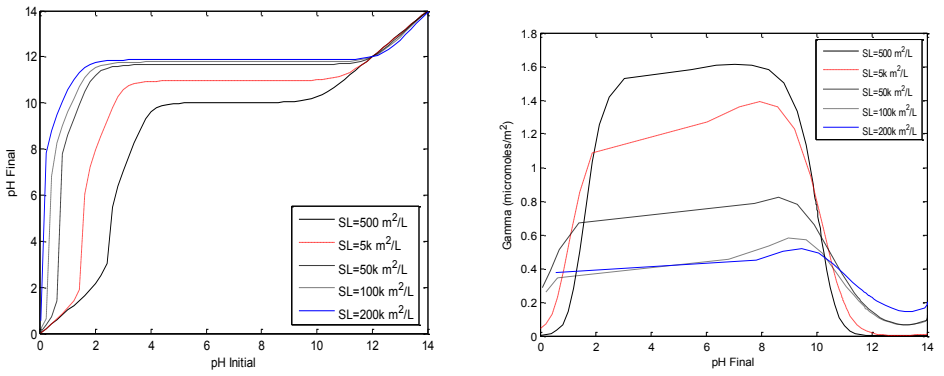

Figure 2.5 RPA prediction of Pt adsorption over oxides of various PZC surface with different surface loading from 500-200,000 m^2/L: a) PZC=2, b) PZC=4, c) PZC=6, d) PZC=8, e) PZC=10, f) PZC=12

The desired final pH can be chosen first with reference to the uptake-pH plot, as illustrated in figure 2.6. For a PZC 2 support, the desired final pH would be 9. (The final pH for this material could actually be in a wider range, as seen in the wide uptake plateau typical of a very low PZC material.) Second, knowing the surface loading which

corresponds to dry impregnation, the plot of the pH shift for that material is consulted (figure2.6a) and the initial pH is which corresponds to the desired final pH at the known surface loading is selected. In the supporting material we provide large, gridded versions of the plots in figure 2.5 for convenience.

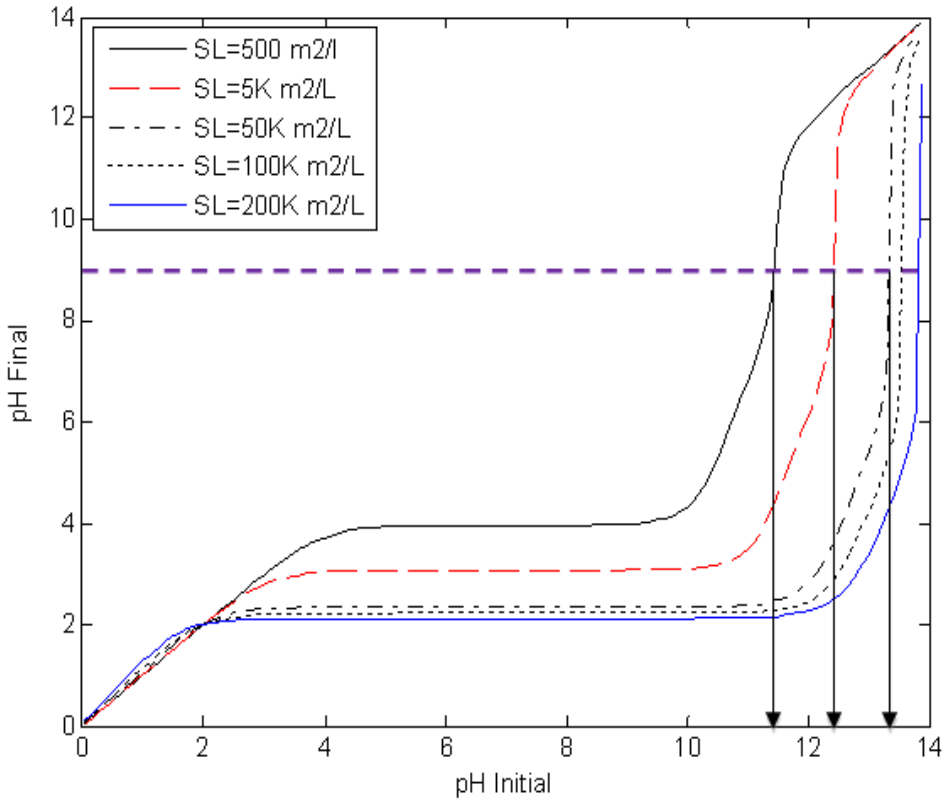

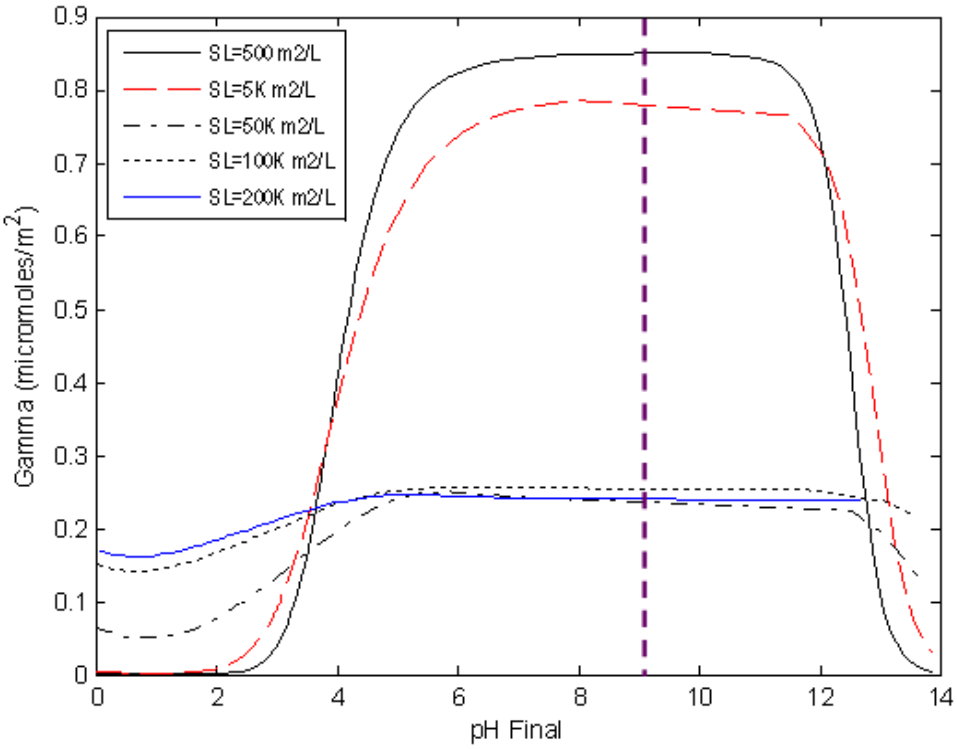

Figure 2.6 Example for how to predict initial pH for optimal adsorption

The accuracy of the pH shift prediction is a logarithmic function of the assumed hydroxyl density, and is thus only weakly dependent on this value. A typical value of 5 OH/nm^2 was used to generate the plots of figure 2.5 and should be sufficient in most cases for a reasonable accurate prediction of the pH shift. In some cases such as unoxidized carbon supports, which have an order of magnitude lower density of surface function groups at low pH than corresponding oxide surfaces [14], the pH prediction may be off by one pH unit or so. In any case, the final pH of the dry impregnation paste can be measured with a semi-solid pH electrode, of the type used to measure pH in semi-solids such as soil and food. With figure 2.5 for guidance and a few experimental measurements as confirmation, the initial impregnation pH can be quickly determined.

In this way, charged enhanced dry impregnation can be simply applied to many metals and carbon and oxide supports to optimize metal dispersion in laboratory scale as well as industrial preparations.

CHAPTER 3

NOBLE METAL OXIDES PZCS AND ADSORPTION OF NOBLE METAL PRECURSORS

Strong electrostatic adsorption (SEA) has been established for the synthesis of single metal catalysts with a multitude of common supports [16,26]. Job et al. demonstrated that the method of SEA allows for fine control of both the structure and morphology of supported metal nanoparticles (average particle size, size distribution, degree of agglomeration) and it may then be used to minimize the amount of metallic Pt used in PEM fuel cells [26]. Jiao et al. demonstrated that SEA appears to be a rational procedure for the cost effective, repeatable and scalable preparation of highly dispersed mono-metallic supported catalysts for all metal ammine complexes adsorbed on multiple varieties of silica [16].

More recently, SEA has been applied to selective adsorption over promoted oxides [17,27]. Feltes et al. investigated the fundamental surface charging properties of an oxide in solution to achieve the selective adsorption of a Mn promoter onto the supported Co_3O_4 and not onto the TiO_2 support material for Fisher-Tropsch synthesis [17]. Zhao et al. also confirmed Mn is selectively adsorbed on Co and not on SiO_2 support with the impregnation of Mn onto Co/SiO_2 by selective SEA of the Mn [27].

Noble metal bimetallic catalysts have been chosen as the materials to be investigated for this proposal. Noble metals were chosen to maximize impact among the catalysis community and for ease of experimentation through the use of SEA, especially

the use of a core-shell structure of noble metals (referred by NMs) which has been shown to significantly increase reactivity for reactions such as oxygen reduction reaction and oxidation of carbon monoxide [28-31]. Pd core@Pt shell catalysts synthesized by the method of electroless deposition have demonstrated better activity for the oxygen reduction reaction when compared to a 20wt% commercial Pt catalyst [28]. Ru@Pt and Rh@Pt nanoparticles (NPs) show increased performance for CO oxidation than traditional PtRu and PtRh alloy catalyst [29,30] Au metal core covered by PdO thin shells by deposition-precipitation (DP) demonstrated a synergetic effect in the selective arabinose oxidation by molecular oxidation [31].

Although SEA also has the potential for the preparation of noble bimetallic catalysts, the point of zero charge (PZC) of NM oxides To determine an appropriate precursor to selectively adsorb noble metals, the PZC value of the noble metal oxides involved are required. For an accurate measurement, large quantities of noble metal oxides are needed to measure PZCs at high surface loading. The problem in experimental determination is the cost of materials such as Pt which costs in excess of $50,000 (USD)/kg.

Johnson Matthey provided access to the large amounts of NM oxide powders needed to perform there measurements at the JMTC in the UK. We measured the PZCs of many NM oxides and in addition conducted uptake surveys of NM cationic complexes over the NM oxides which neutral to acidic PZCs.

3.1 EXPERIMENTS

3.1.1 Materials

All chemicals and characterization equipment were graciously provided by JMTC,

Sonning Common, UK. The characteristics of the NM oxides studied are summarized in table 3.1, and the NM precursor complexes are listed in table 3.2.

Table 3.1 Surface are and pore volume of noble metal oxides

Oxide	**PtO_2 H_2O**	**Rh_2O_3**	**RuO_2**	**PdO H_2O**	**IrO_2**	**Ag_2O**
Surface Area(m^2/g)	104	11	98	118	71	0.2
Pore Volume (ml/g)	0.85	0.40	0.75	0.2	0.25	0.30

Table 3.2 Cation noble metal complex precursors

#	Cation precursor	Structure	r_{ion}	Valence	MW
1	Pd tetraamine hydrogen carbonate	$[Pd(NH_3)_4](HCO_3)_2$	2.55	+2	296.57
2	Pt tetraamine hydroxide solution	$[Pt(NH_3)_4](OH)_2$	2.41	+2	297.22
3	Ru hexaamine trichloride	$[Ru(NH_3)_6]Cl_3$	2.79	+3	294.42
4	Rh ethylenediamine chloride	$[Rh(en)_2Cl_2]Cl$ H_2O	3.12	+1	329.33
5	Ir ethylenediamine chloride	$[Ir(en)_2Cl_2]Cl$	3.22	+1	418.77
6	Au ethylenediamine chloride	$[Au(en)_2]Cl_3$	3.00	+3	423.52

r_{ion} is a radius (A) of cationic atom.

3.1.2 PZC Measurement of NM Oxides

Three point PZC measurements were used to accurately determine oxide PZCs. After adding distilled water (pH 5.6) and pH adjusted water (pH 3 and 9) to exactly fill the measured pore volume of the oxide at each pH value. At incipient wetness the pH of

thick NM oxide slurry was measured through the use of a spear tip combination pH probe. The pH meter was calibrated at pH values of 4, 7 and 10 before measurements.

3.1.3 Uptake Survey of NM Oxides with NM Cation Precursors

20ml of each precursor solution was prepared in HDPE bottles and pH of the solutions was adjusted over the range 2 to 13. NM oxides (except Ag_2O) were then added to the pH adjusted solutions to achieve a surface loading of $1000 m^2/L$. The slurries were filtered after 1 hour contact time and then the NM concentration was determined pre and post oxide contact by the ICP-OES (Thermo iCAP 6500).

3.1.4 Characterization

A. XRD

Powder XRD measurements were made using a Bruker AXS D8 with 45 position sample changer. XRD patterns were compared to reference spectra using Bruker AXS Diffrac Plus, Eva V16 software. The radiation source was Cu Kα radiation ($\lambda = 1.5406$ Å) at operating condition of 40kV and 40mA. All patterns were taken in the 10^o-80^o 2θ range whith a scan rate of 1^o/min and sampling width of 0.02^o. A representative pattern is shown in Figure 3.1.

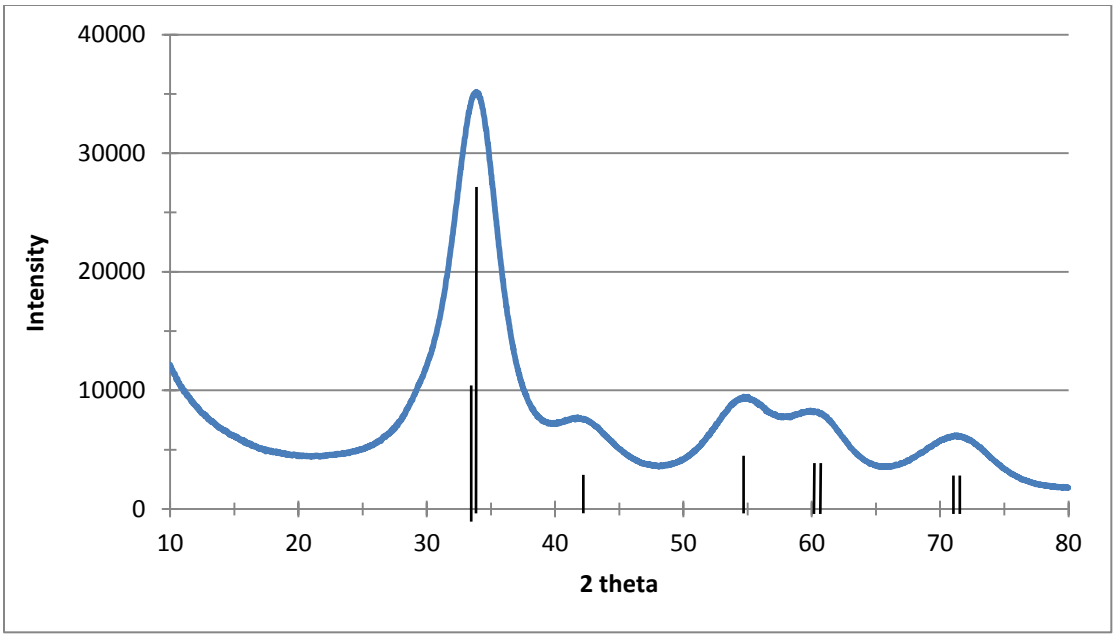

Figure 3.1 Example of XRD ($PdO \cdot H_2O$)

B. BET

BET surface area measurements were obtained using an automated adsorption system (ASAP, 2100, Micromeritics). After degassing at 150ºC, the samples were transported from degassing port to analysis port and doping with N_2 in liquid nitrogen pool. Surface area were calculated by the linear relation between P/P_o and $1/ [v(P/P_o-1)]$ with 8 points from 0~0.35 of P/P_o values.

C. XPS

XPS measurements were carried out using a Thermo VG Scientific Escalab 250 operated with monochromatized aluminum Kα radiation and the magnetic lens system activated. Charge compensation was provided by an in-lens electron flood gun at 2 V and a low-energy argon ion flood source. Survey spectra were collected with a pass energy of 150 V and detail spectra with a pass energy of 30 V. The samples were dusted onto carbon tape and thereby mounted on a standard sample stub.

3.2 RESULT

3.2.1 XPS

XPS analysis of the NM oxides was performed to confirm the oxidation state of the metals and to investigate the impurity of the surface. The XPS spectra are shown in figure 3.2. The survey spectrum for PtO_2 in figure 3.2a confirms the presence of Pt in the +4 oxidation state with $Pt4f_{5/2}$ and $Pt4f_{7/2}$ binding energies at 76.7 and 73.4 eV, respectively. Trace impurity of Cl $2p_{3/2}$ (198.1 eV) is indicated in the survey scan.

The spectra of Rh_2O_3 are shown in figure 3.2b. Trace impurities of N 1s (402.9 eV) and Cl $2p_{3/2}$ (197.9 eV) are seen in the surface scan. The Rh $3d_{3/2}$ and $3d_{5/2}$ peaks at 313.3 and 308.5 eV correspond to Rh +3. Spectra for RuO_2 are shown in figure 3.2c. The Ru $3p_{1/2}$ and $3p_{3/2}$ peaks at 485.7 eV and 463.4 eV reveal Ru +4. Trace impurity of Cl $2p_{3/2}$ (199.1 eV) is confirmed in the survey scan. Figure 3.2d shows the survey spectrum of PdO. The binding energies of Pd $3d_{1/2}$ and $Pd3d_{3/2}$ at 342.4 and 337 eV are indicated +2 oxidation state of Pd. The impurities of Si 2s (150.8 eV) and Cl $2p_{3/2}$ (198.6 eV) are shown in survey scan. The spectra of IrO2 in figure 3.2e demonstrated that the oxidation state of Ir is +4 because $Ir4d_{3/2}$ and $Ir4d_{5/2}$ peaks are existed at 313.8 eV and 297.8 eV. Trace impurities of Na 1s (1071.1 eV) and Cl $2p_{3/2}$ (197.6 eV) are strongly indicated.
XPS confirmed every NM oxide has right metal valence and oxygen state. I will further discuss about contamination of IrO_2 at 3.2.3.

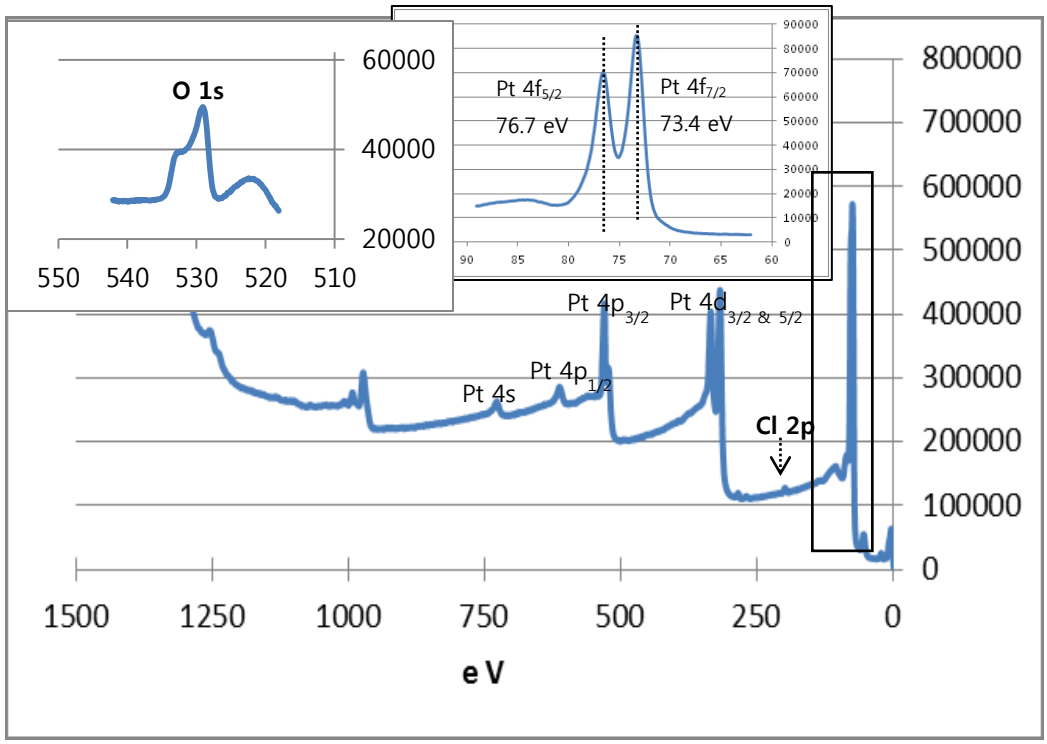
O 1s
60000
40000
20000
550 540 530 520 510
Pt 4f5/2
76.7 eV
Pt 4f7/2
73.4 eV
90000
80000
70000
60000
50000
40000
30000
20000
10000
0
90 85 80 75 70 65 60
Pt 4p3/2
Pt 4d3/2 & 5/2
Pt 4p1/2
Pt 4s
Cl 2p
800000
700000
600000
500000
400000
300000
200000
100000
0
1500 1250 1000 750 500 250 0
e V

a)

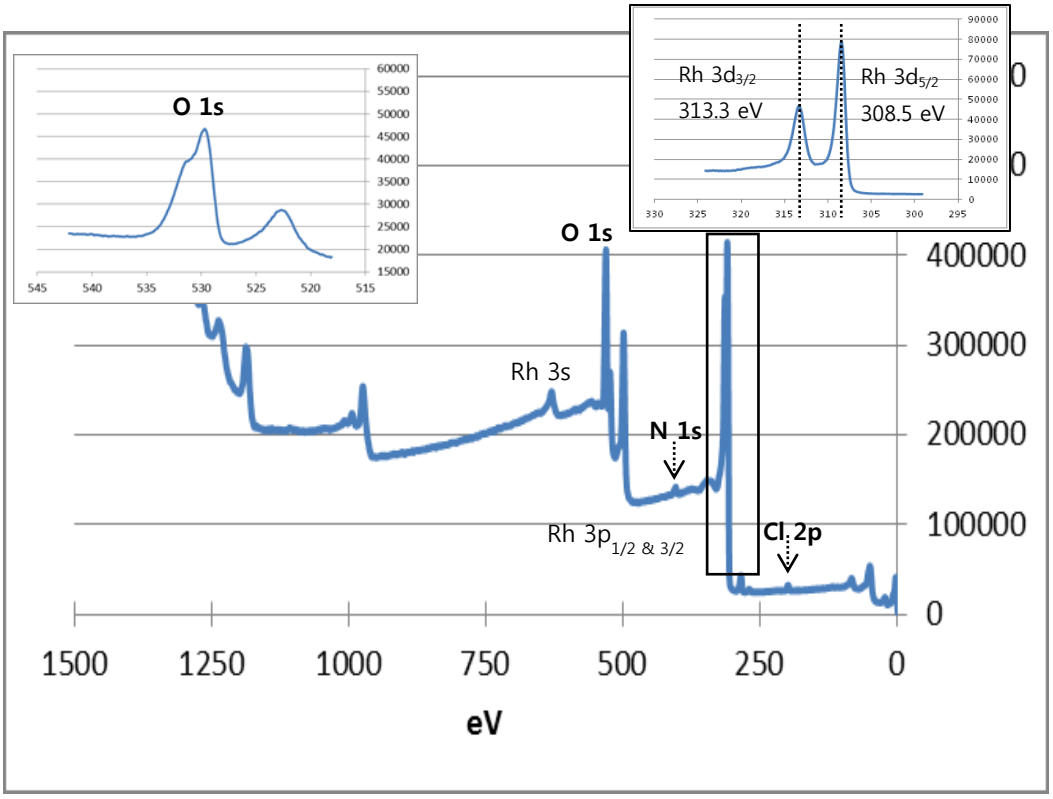
O 1s
60000
55000
50000
45000
40000
35000
30000
25000
20000
15000
545 540 535 530 525 520 515
Rh 3d3/2
313.3 eV
Rh 3d5/2
308.5 eV
90000
80000
70000
60000
50000
40000
30000
20000
10000
0
330 325 320 315 310 305 300 295
O 1s
Rh 3s
N 1s
Rh 3p1/2 & 3/2
Cl 2p
400000
300000
200000
100000
0
1500 1250 1000 750 500 250 0
eV

b)

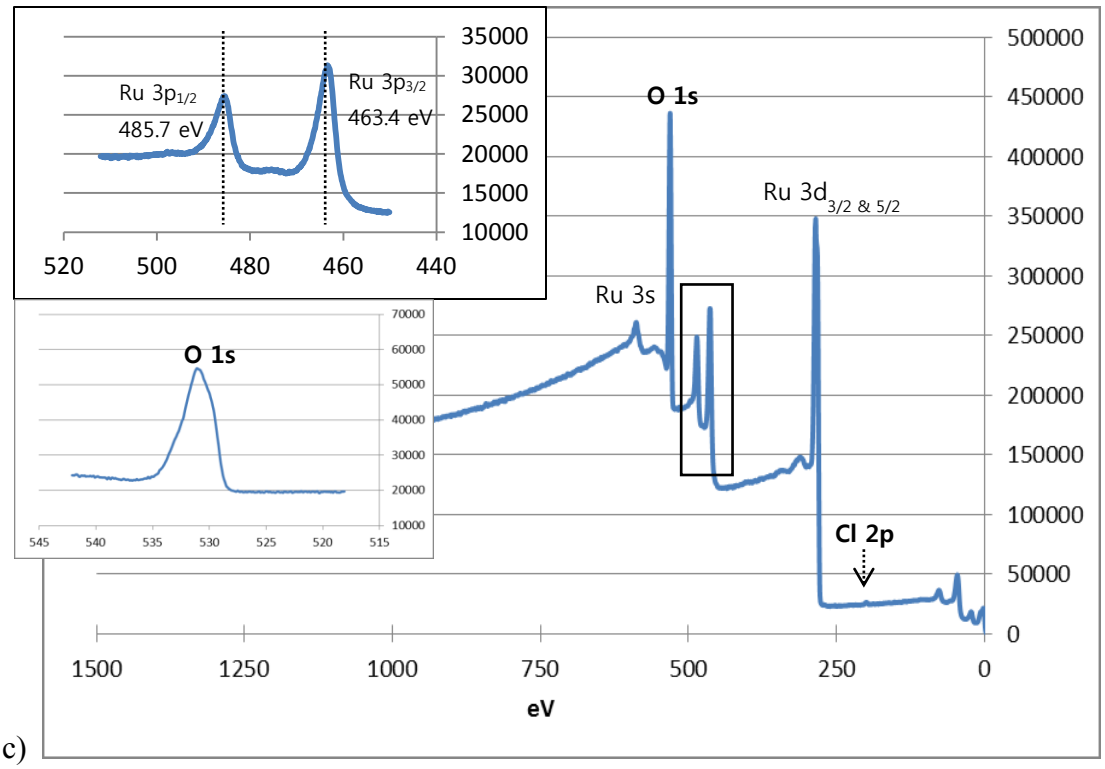
Ru 3p1/2
485.7 eV
Ru 3p3/2
463.4 eV
O 1s
Ru 3d3/2 & 5/2
Ru 3s
Cl 2p
eV

c)

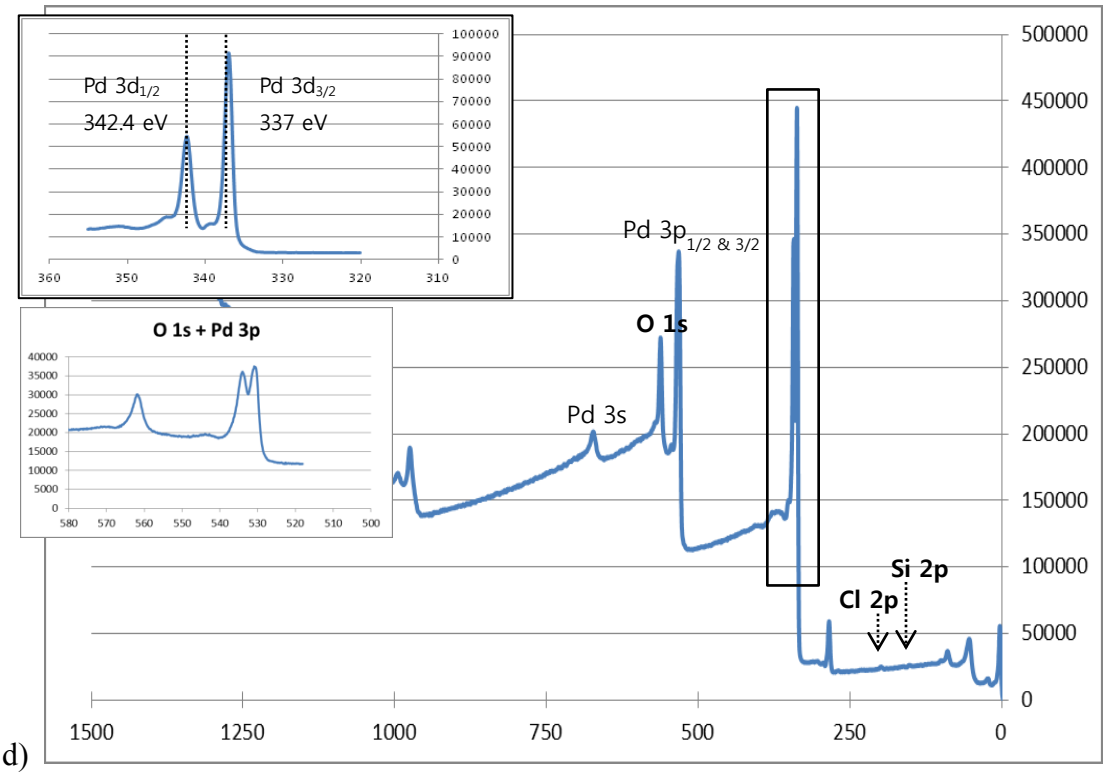
Pd 3d1/2
342.4 eV
Pd 3d3/2
337 eV
O 1s + Pd 3p
Pd 3p1/2 & 3/2
O 1s
Pd 3s
Si 2p
Cl 2p

d)

e)

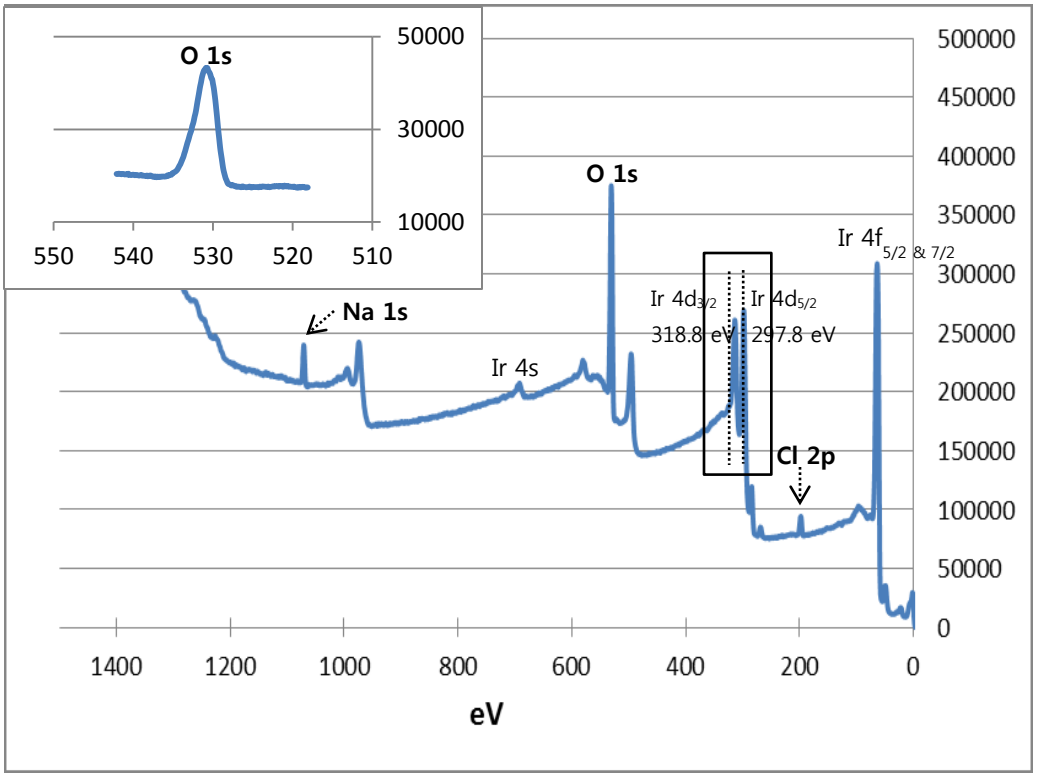

Figure 3.2 XPS survey of NM oxides a) PtO_2 b) Rh_2O_3 c) RuO_2 d) PdO e) IrO_2.

3.2.2 PZC of NM Oxide

PZC determination by the three point method is shown in figure 3.3. Each of the 3 different points of initial pH equilibrated to a similar final pH after the surface hydroxyl groups of NM oxide became saturated due to the high surface loading and the accompanying buffering effect of the pH adjusted solution.[6]. The average value of final pH is then regarded as the PZC of each corresponding NM oxide.

The averaged PZC value of PtO_2 is 1.0, Rh_2O_3 is 2.2 and RuO_2 is 2.7. These NM oxides are low or acidic PZC materials. PdO has an averaged value of 4.0, while that of IrO_2 is 6.0. Both are identified as materials with mid-range or neutral PZCs. Ag_2O has a PZC value of 9.6 and can be regarded as high or basic PZC material. The determination

of PZC of OsO_4 was not obtained due to its high toxicity. Finally, that of gold oxide cannot be obtained as it is unstable.

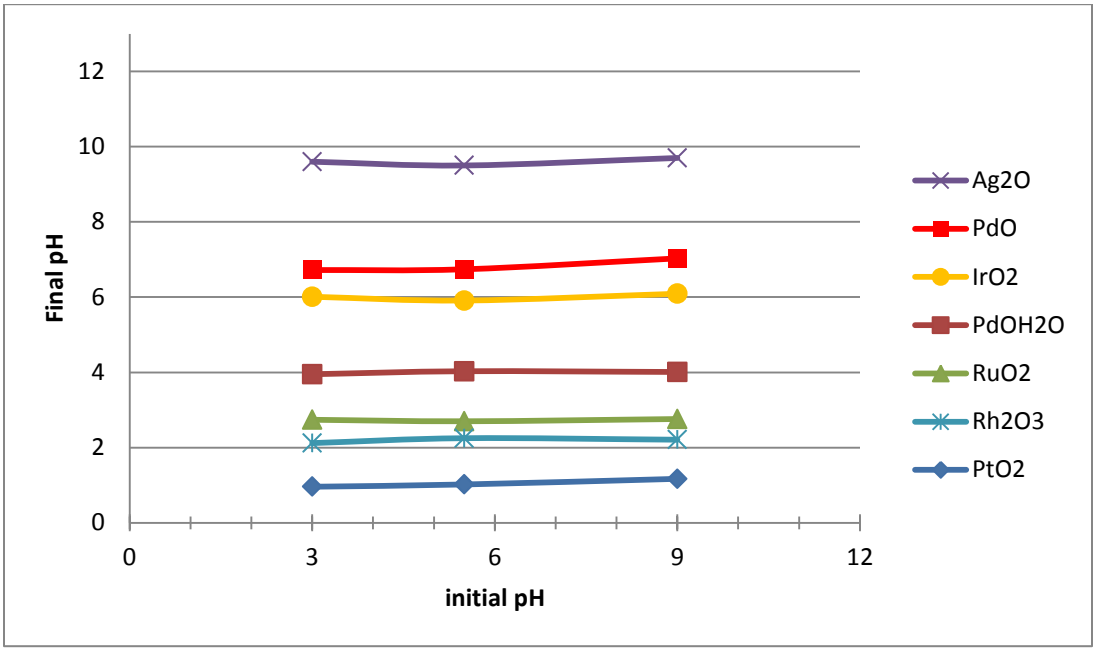

Figure. 3.3 3 points measurement for PZCs of NM oxide

Based on these PZC measurements, we are able to determine the valence of NM precursors appropriate for selective adsorption over each NM oxide. Cationic NM precursors can be electrostatically adsorbed effectively over neutral and acidic PZC NM oxides (PtO_2, Rh_2O_3, RuO_2, PdO and IrO_2) in the basic pH range by the interaction between cationic precursors (positively charged) and deprotonated surface hydroxyl groups (negatively charged) of the metal oxide. Anionic NM precursors will adsorb strongly when coupled with neutral and basic PZC NM oxides (IrO_2 and Ag_2O) due to the surface hydroxyl groups of these NM oxides becoming protonated over the acidic pH range.

3.2.3 Uptake Surveys

The adsorption of the noble metal cationic complexes listed in table 3.2 was then

measured as a function of pH over each noble metal oxide. The results are plotted for each NM oxide.

A. PtO_2 (PZC=1.0)

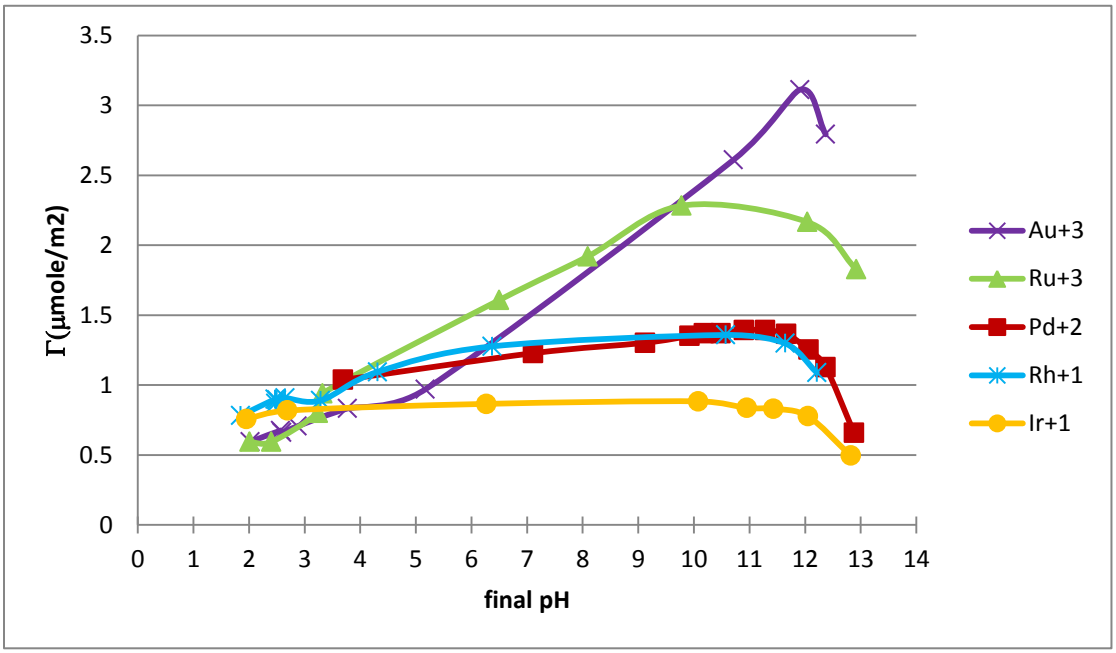

Figure 3.4 Uptake survey of NM cation precursors with PtO_2

Since PtO_2 has an extremely low PZC, every noble metal complex used was adsorbed over the entire range of pH values from 2-13. The uptake plots have a corresponding wide plateau at the maximum adsorption of metal precursors except for the Au and Ru cationic precursors which display unusually high uptake values. The adsorption-retarding effect of high ionic strength at extreme values of pH that occur at high pH are apparent for all metal complexes studied. The +3 complexes of Au and Ru show relatively higher uptake with a maximum surface densities of 3.1 and 2.3 µmole/m^2. One of the singly valent cations, Ir, exhibits the lowest level of uptake, while the other +1 cation, of Rh, exhibits about the same uptake as the doubly valent Pd cation.

The maximum surface density of each species might be related to the degree of hydration retained by each respective complex. The maximum density of the Ir complex, at about 0.88 μmole/m^2, corresponds to a close packed monolayer of Ir complexes which retains one or two hydration sheaths. Given the size of the complex at 3.22 Å (table 2.2) and the diameter of water, 2.76 Å, this maximum value with two hydration sheaths is calculated to be 0.64 μmole/m^2. The maximum surface density of the +2 Pd complex and the +1 Rh complex, on the other hand, are closer to a layer of complexes which retain one hydration sheath. For the 2.55 Å Pd tetraammine complex, this value is 1.87 μmole/m^2 and for the approximately 3.12 Å diameter Rh ethylenediammine complex, this value is 1.53 μmole/m^2. The very high values of the +3 Au and Ru complexes are between the values expected for one and zero hydration sheathes. For example, the maximum adsorption density of the cationic Au precursor is 5.9 μmole/m^2, if no hydration sheaths are retained among the adsorbed complexes. The number of hydration sheaths can be used as an adjustable parameter to fit the maximum surface density. The average number of hydration sheaths of the Au complex is calculated to be 0.4, while the average number of sheaths retained by the Ru complex is calculated to be 0.7. Over PtO_2 it appears in general that the higher the valence, the lower the number of hydration sheaths retained by the adsorbing complex.

B. Rh_2O_3 (PZC=2.2)

Rh_2O_3 is an optimal support for the adsorption of noble metal cation precursors over the pH range of 3 – 13 because Rh_2O_3 also has an acidic PZC. The +3 Ru cation again displays a relatively high maximum uptake and achieves about the same surface density (2.3 μmole/m^2) as over PtO_2, corresponding to an average number of hydration

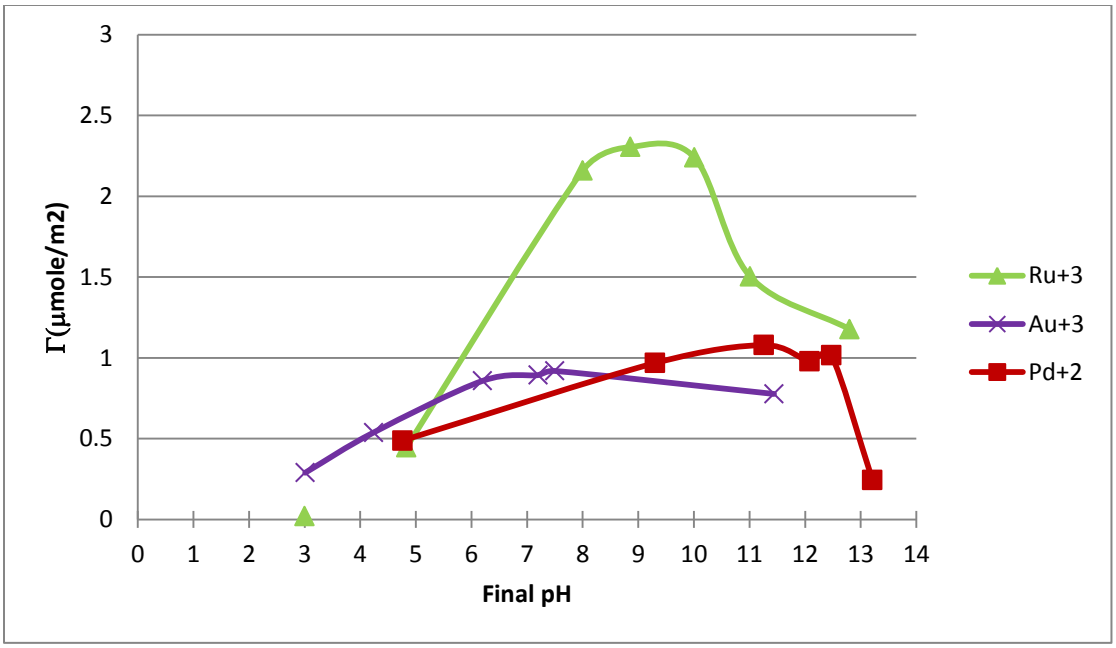

Figure 3.5 Uptake survey of NM cation precursors with Rh_2O_3

sheaths retained of 0.7 The +3 Au complex does not adsorb to the same high extent over Rh_2O_3 as over PtO2; uptake tops off at 0.9 µmole/m^2 and corresponds to the retention of an average of 1.7 hydration sheaths. The Pd tetraammine complex adsorbs to a slightly lower level than over PtO2, and appears to retain 1.6 hydration sheaths.

C. RuO_2 (PZC=2.7)

When RuO_2 was contacted for adsorption surveys, every cationic NM precursor adsorbed over a wide pH range. Since the PZC of RuO_2 is 2.7, uptake is minimal at pH values in the range of 2-3 and high ionic strength is the cause of decreased uptake at the higher pHs. Therefore, most of the uptake graphs of NM precursors have a wide volcano shape which is typical of SEA. Both +1 precursors (Rh and Ir) again exhibit the lowest relative surface densities, which correspond to the retention of 1 or 2 hydration sheaths (2.2 and 1.5 for Ir and Rh, respectively). Most notable is the high adsorption density of

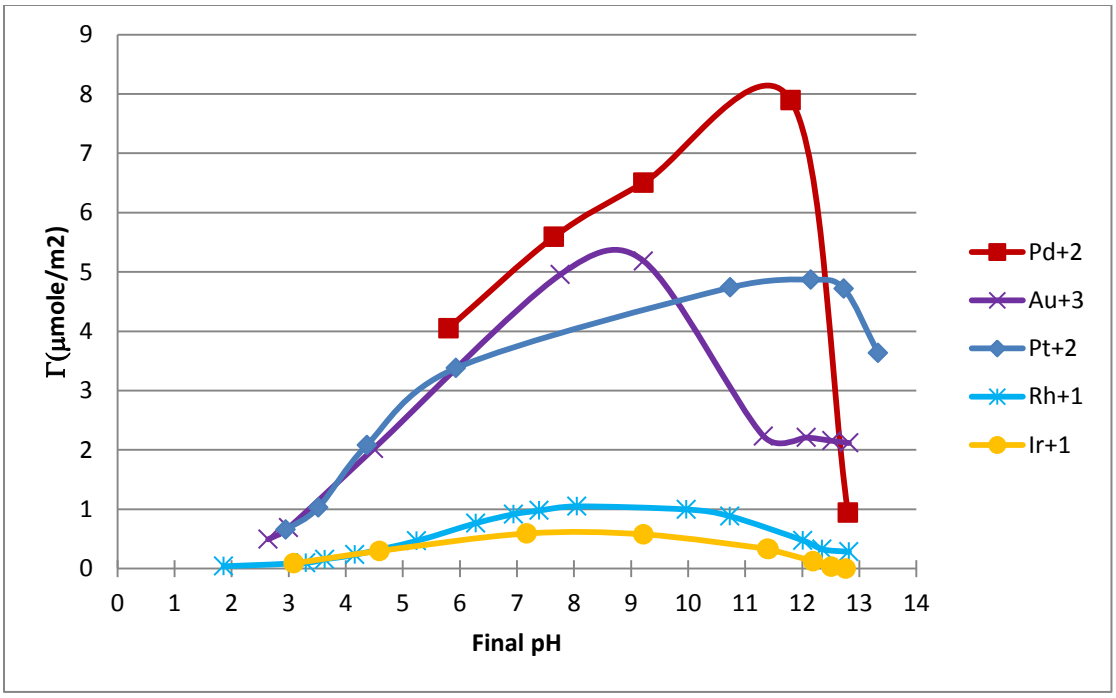

Figure 3.6 Uptake survey of NM cation precursors with RuO_2

the +2 Pd and +3 Au cations. The experimentally determined value for maximum uptake of 7.9 μmole/m^2 and 5.2 μmole/m^2 (for Pd and Au, respectively) is very near the close-packed density of complexes retaining no hydration sheaths, 8.1 μmole/m^2 and 5.9 μmole/m^2. The +2 Pt complex also adsorbs at an unusually high value, 4.9 μmole/m^2, corresponding to the retention of an average of 0.3 hydration sheaths.

D. PdO(PZC=4)

The volcano-shaped adsorption profiles over PdO are all reflective of the electrostatic mechanism; however the trends with precursor valence seen over other NM oxides do not appear here. The uptake of the +3 Au precursor is lowest, while that of the +1 Rh complex is highest. The maximum surface density is relatively low; the number of hydration sheaths retained is calculated to be 1.7, 2.3, 1.4, and 1.2 for the Pt, Au, Ru, and Rh precursors, respectively. The higher PZC of PdO may not give rise to as strong a

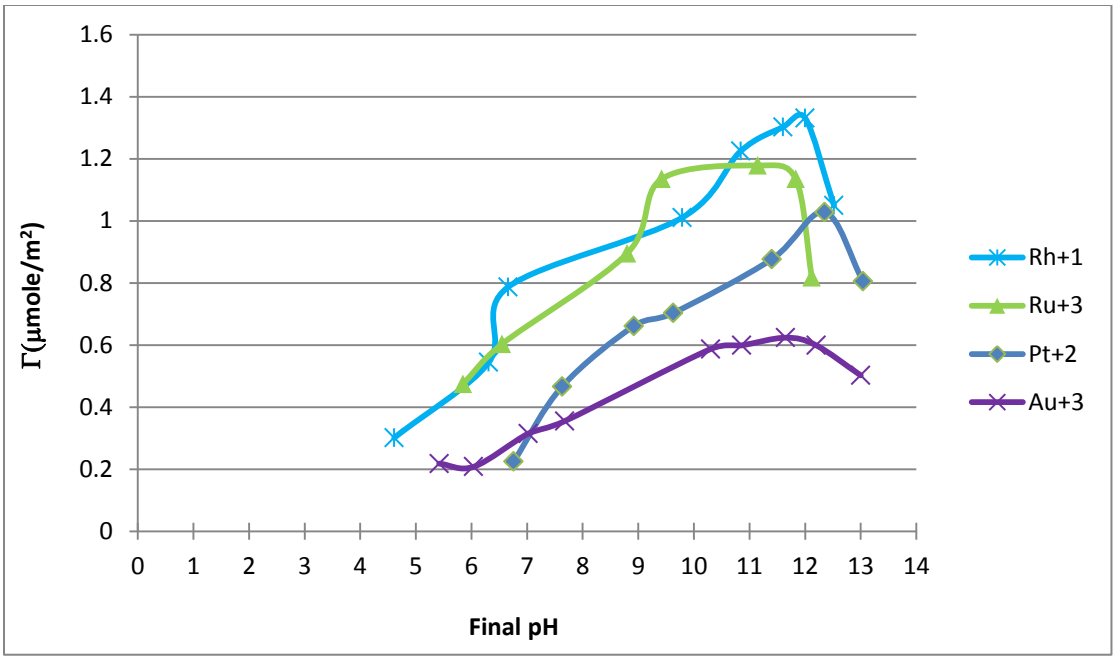

Figure. 3.7 Uptake survey of NM cation precursors with PdO

coulombic interaction with the surface, allowing more hydration sheaths to be retained by the adsorbed complexes.

E. IrO_2 (PZC=6)

The maximum surface density of all complexes is less than 1 μmole/m^2, and like PdO it appears that the higher PZC material allows more hydration sheaths (all around 2, table 3.3) to be retained by the adsorbing complexes. The +3 Au complex adsorbs to the highest extent and the +1 Rh complex to the lowest extent. On the other hand, three of the four precursors (Au, Pt, and Rh) appear to adsorb to a significant extent near the measured PZC of Ir. Either the measured PZC of IrO_2 is incorrect, or there may be more than electrostatic interactions between some of the noble metal cationic precursors and IrO_2. It it noted that in the XPS survey of IrO_2 (figure 3.2e) there are significant amounts of chloride (197.6 eV) and even more sodium (1071.1 eV). In past research [32], ion doping of oxides have been shown to alter PZC; the PZC silica can altered from the

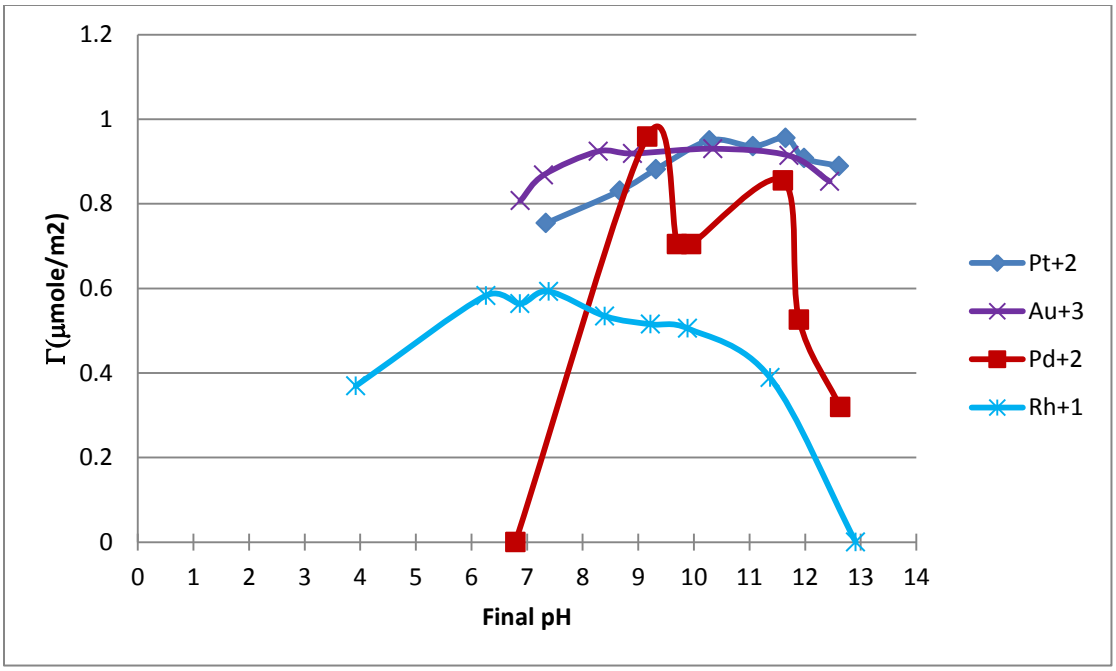

Figure 3.8 Uptake survey of NM cation precursors with IrO_2

typical of 4 to near 8 by K doping. In this case, IrO_2 has both Na and Cl contamination but Na is observed to be at a concentration roughly double that of Cl, and the net effect might be a measured IrO_2 PZC higher than the actual value. The previous study [32] also showed that the dopant had no effect on adsorption.

Moreover, PZC tends to vary dramatically with the metal valence; silica (Si^{4+}) is about 4, alumina (Al^{+3}) is about 8, and magnesia (Mg^{+2}) is about 12. Compared with PtO_2 (Pt^{4+}, PZC=1) and RuO_2 (Ru^{4+}, PZC=2.7), IrO_2 (Ir^{4+}) expected to have a more acidic PZC than measured PZC 6. It may thus be the case that the PZC of IrO2 is below the measured value; the adsorption trends would indicate a PZC of perhaps 2-3.

It is noted that galvanic replacement has not been observed in the entirety of the experiments. This mechanism would have been detected by the presence of the dissolving metal oxide in solution and no such dissolved metals were ever detected.

3.3 DISCUSSION

Two general trends were observed in the noble adsorption surveys. First, the maximum adsorption density was usually in proportion to the valence of the adsorbing precursor. The +1 Rh and Ir precursors most often exhibited the lowest maximum uptake, while the +3 Au and Ru complexes often adsorbed at the highest density. One exception was RuO_2, over which the Au and Pd precursors lost all hydration and the maximum surface density was dictated by the size of the NM complex itself. Another exception was PdO, over which the +1 Rh complex adsorbed at the highest density and the +3 Au complex at the lowest. Over PdO all precursors appear to retain 2 hydration sheaths, so once again the surface density is dictated primarily by the size of the respective complexes. A second general trend is that over the lowest PZC NM oxides Rh_2O_3, PtO_2, and particularly RuO_2, the electrostatic interaction appeared so strong that the adsorbing complexes lost their hydration sheaths to a considerable extent. Normal values for the number of hydration sheaths retained by NM and base metal ammine complexes over silica (PZC near 4) is 1 to 2 [15,16]. Either the lower PZCs of the acidic PZC NM oxides, or a non-electrostatic mechanism present over NM oxide surfaces might account for this effect. Future modeling efforts will be directed toward a more precise understanding of the interrelationship between size, valence, the number of hydration sheaths and PZC.

The experimental results of NM precursor adsorption onto NM oxides can be used to guide the rational synthesis of supported noble metal bimetallic particles, if the assumption is made that nanoparticulate noble metal oxides exhibit the same adsorptive properties as the bulk noble metal oxides tested here. (In fact, the high surface area PtO_2 and PdO materials at 104 and 118 m^2/g, respectively, do have small primary particle size,

on the order of 5.7 and 6.1 nm.) The maximum adsorption density achievable over a particular NM oxide by another NM precursor and the final solution pH at which this occurs, are known. These data are collected in table 3.3. Thus the amount of NM precursor deposited onto a NM oxide nanoparticle surface is known, and accounting for the dispersion of the NM oxide nanoparticle, the amount of NM precursor adsorbed per total NM oxide particle can be calculated. Assuming that NM oxides shrink about 20% as they are reduced, the shellNM/coreNM molar (or atomic) ratio for various core NM particle sizes can be further calculated.

Table 3.3 Maximum adsorption densities and associated pH values

Precursor	PtO_2			Rh_2O_3			RuO_2			PdO			IrO_2		
	G_{max}	#HS	pH_{opt}	G_{max}	#HS	pH_{opt}	G_{max}	#HS	pH_{opt}	G_{max}	#HS	pH_{opt}	G_{max}	#HS	pH_{opt}
Pt							4.9	0.3	12	1	1.7	12.5	0.9	1.9	11.7
Pd	1.4	1.3	11.6	1.1	1.6	11.2	7.9	0	11.8				1	1.7	9.2
Au	3.1	0.4	11.9	0.9	1.7	7.2	5.2	0	9.2	0.6	2.3	11.7	0.9	1.7	10.3
Ru	2.28	0.7	10	2.3	0.7	8.7				1.2	1.4	11.2			
Ir	0.88	1.6	10				0.6	2.2	9.2						
Rh	1.36	1.1	10.6				1	1.5	10	1.3	1.2	12	0.6	2.3	7.4

The idea is illustrated in figure 3.9. For smaller NM oxide (core) particles, the amount of adsorbing NM precursor (NM shell) will be relatively high compared to larger NM oxide cores.

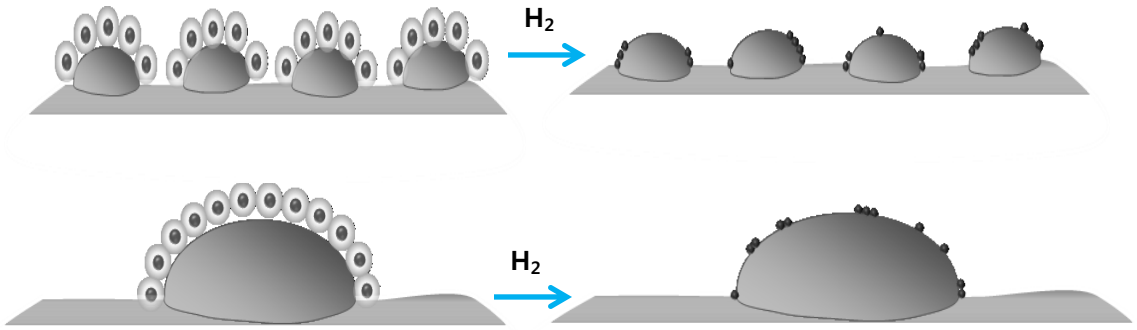

Figure 3.9 Schematic of the adsorption over small size support vs big size support

As an example, for a 2 nm core of PtO_2 (with a dispersion of 0.5, or one surface Pt atom per 2 total atoms), the Rh complex adsorbs at 1.36 μmol/m^2 at a solution pH of 11. The NM site density in the oxide particles is assumed to be the typically employed value of 1 x 10^{19} sites/m^2. The molar ratio of shell Rh/core Pt is therefore

$$\left(\frac{1.36\mu mole\ Rh}{m^2\ of\ PtO2}\right)\left(\frac{m^2 of\ Pt}{1*10^{19}\ Pt\ surface\ sites}\right)\left(\frac{m^2\ of\ PtO2}{0.8\ m^2\ of\ Pt}\right)\left(\frac{6.02*10^{23} of\ Pt\ atoms}{1\ mole\ of\ Pt}\right)\left(\frac{Pt\ surface\ sites}{2\ Pt\ atoms}\right)\left(\frac{mole}{10^6\mu mole}\right)$$

For a 1 nm particle (100% versus 50% dispersion), this ratio will be double to 0.05. For a 10 nm particle (10% versus 50% dispersion), the ratio will be five times lower at 0.05.

Plots calculated for a single SEA application of the various NM precursors are shown in figure 3.10. For PtO_2 (figure 3.10a), molar ratios of 0.21 to 0.06 can be achieved with the various NM precursors if the Pt phase is very well dispersed (1 nm particles). Over poorly dispersed, 10 nm particles, the molar ratios drop to 0.025 – 0.001. Similar loadings are seen over Rh_2O_3 (figure 3.10b), while for RuO_2, over which most

NM precursors lost the entirely of their hydration sheaths, ratios as high a 0.54 can be achieved for the multivalent precursors, with the smallest RuO_2 particles. PdO and IrO_2, which adsorbed the lowest density of NM precursors, have the lowest molar ratios of shell to core metal.

a)

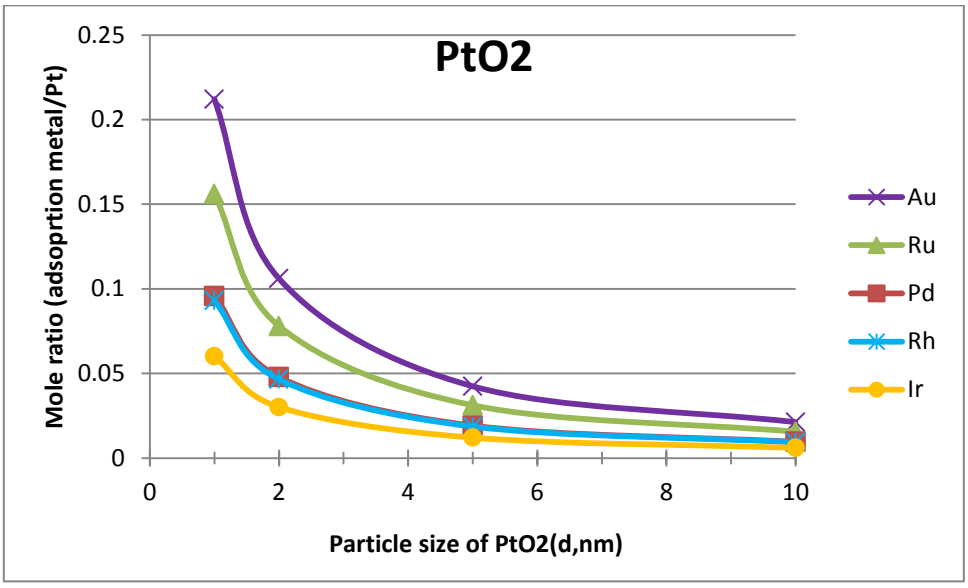

b)

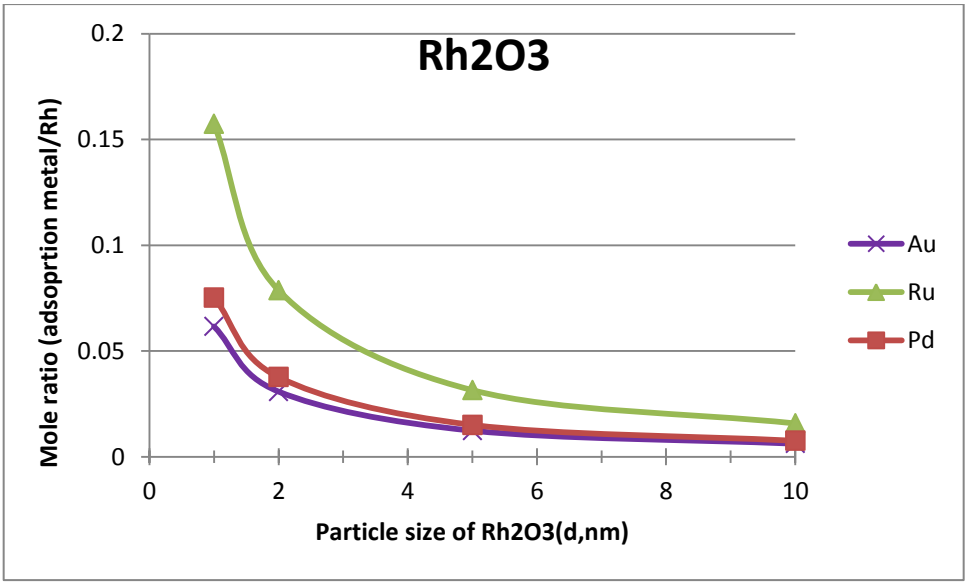

c)

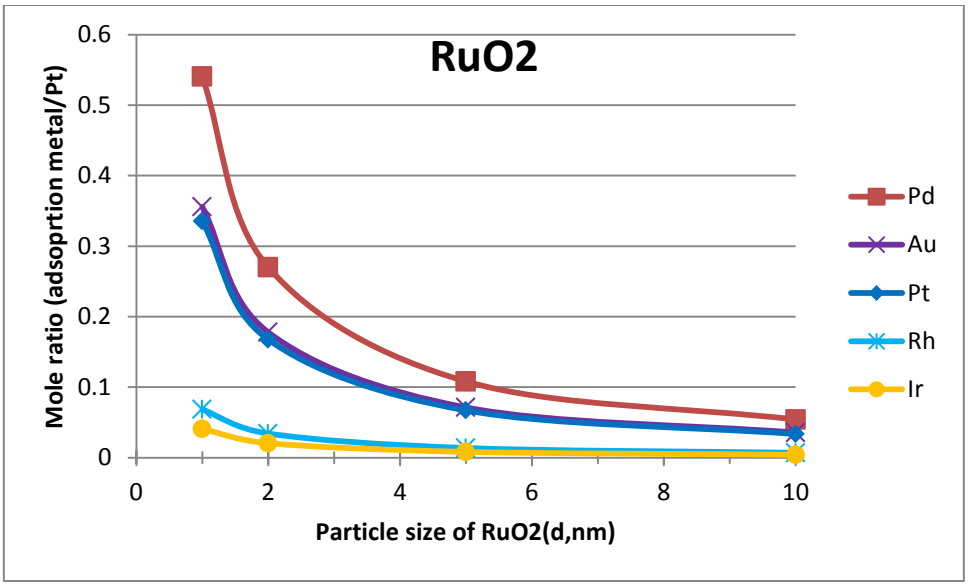
RuO2
Mole ratio (adsoprtion metal/Pt)
0.6
0.5
0.4
0.3
0.2
0.1
0
0
2
4
6
8
10
Particle size of RuO2(d,nm)
Pd
Au
Pt
Rh
Ir

d)

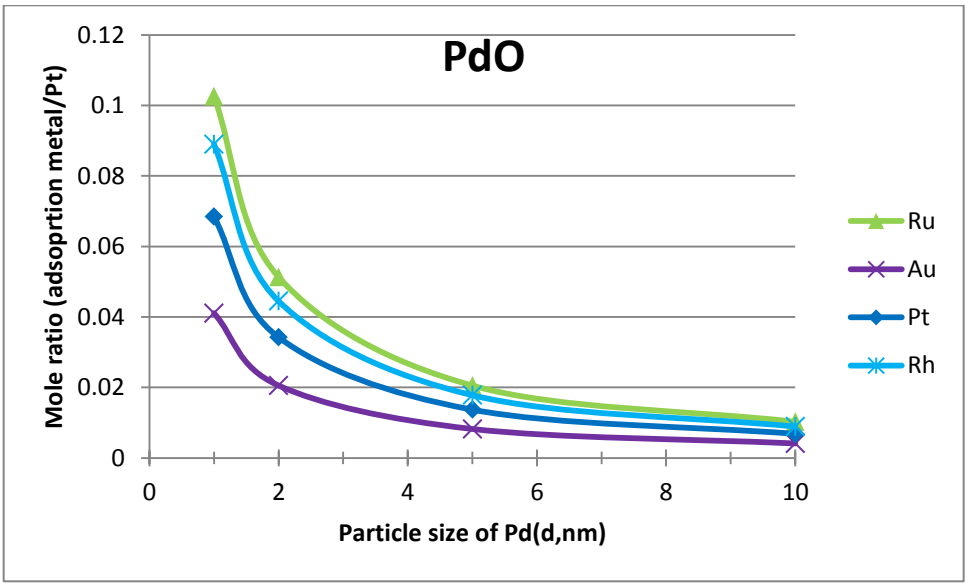
PdO
Mole ratio (adsoprtion metal/Pt)
0.12
0.1
0.08
0.06
0.04
0.02
0
0
2
4
6
8
10
Particle size of Pd(d,nm)
Ru
Au
Pt
Rh

e)

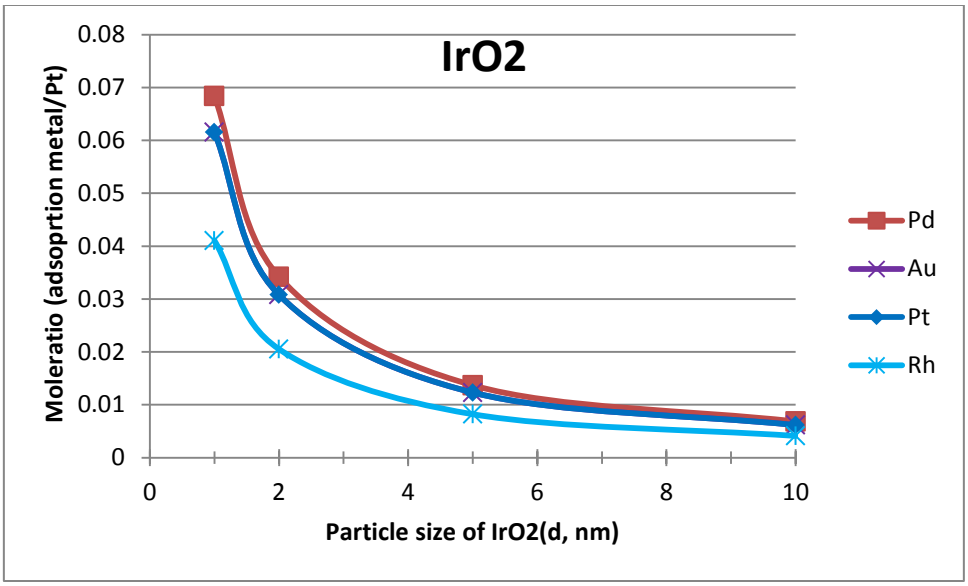

Figure 3.10 Max. shell metal ratio vs particles size of core metal oxide a) PtO_2 b) Rh_2O_3 c) RuO_2 d) PdO e) IrO_2

Applying a shell of NM onto a core of supported NM oxide nanoparticles can be termed "sequential SEA" or seq-SEA, if the first NM oxide is itself deposited by SEA. This method is demonstrated in the next two chapters, and is applied by reference to figure 3.10 and table 3.3 to identify the attainable molar ratios of shell metal and the pH at which the deposition must occur.

3.4 CONCLUSION

Table 3.4 lists the measured PZCs of most NM oxides. Most possess acidic PZC

Table 3.4 Measured PZCs of NM oxides

Oxide	PtO_2 H_2O	Rh_2O_3	RuO_2	PdO (H_2O)	IrO_2	Ag_2O
PZC	1.0	2.2	2.7	4.0 – 7.0	(6.0)	9.7

values are readily adsorb cationic precursors over a wide pH range. The PZC measurement is questionable for IrO_2, which contained significant Na^+ and Cl^- impurities; adsorption trends suggest a PZC of 2-3. PdO is unusual in that its hydrated and non-hydrated forms appear to exhibit different PZCs (4 and 7 respectively).

Two general trends were observed in the noble adsorption surveys. First, the maximum adsorption density was usually in proportion to the valence of the adsorbing precursor. Second, over the lowest PZC NM oxides Rh_2O_3, PtO_2, and particularly RuO_2, the electrostatic interaction appeared so strong that the adsorbing complexes lost their hydration sheaths to a considerable extent.

Continuing work includes surveys of noble metal anions onto neutral and basic PZC materials. The PZC and adsorption results presented here will give great guidance to those who wish to employ SEA to synthesize bimetallic catalysts. Future modeling efforts will be directed toward a more precise understanding of the interrelationship between size, valence, the number of hydration sheaths and PZC.

CHAPTER 4

Pd-Pt BIMETALLIC CATALYSTS

Noble bimetallic catalysts are ubiquitous in both academia and industry. A survey of the literature covering catalysis reveals over two hundreds articles and a similar number of patents pertaining to a multitude of bimetallic systems, with applications in air pollution abatement, petroleum refining, Fisher Tropsch synthesis, as well as fuel cell catalysts for both reactions occurring at the anodes and cathodes. A system of great interest are Pt-Pd bifunctional catalysts that impart improved performance for methane combustion [33-38], improved sulfur tolerance in the hydrogenation of aromatics [39-50], destruction of volatile organic compounds (VOCs) which are considered to be one of the major contributors to industrial air pollution [51-53], electrocatalysts for fuel cell [54-56] and hydrodeoxygenation of benzonfuran for biomass conversion [57]. In almost all cases just referenced, Pt-Pd bimetallic catalysts show increased activity and improved catalyst stability when compared with single Pt or Pd catalysts.

More than 50% of the literature surveyed employed dry impregnation to synthesize Pt-Pd bimetallic catalysts. Dry impregnation is used most often for the synthesis of bimetallic catalysts due to the simplicity of synthesis; two metal precursors are dissolved into the amount of solution just necessary to fill the pore volume of the support. The solution is contacted with the support, and the thick paste formed is dried and pretreated. However, when using dry impregnation, the intimate interaction of the two cannot be

well controlled and usually occurs only to a minimal extent.

Several types of catalyst synthesis methods have been developed to ensure metal-metal interaction. First, bimetallic particles can be produced as colloids [58-59] or in dendrimers [60-62]. The advantage of these preparations is that bimetallic particles of a precisely controlled composition and size can be synthesized. However, problems exist even with these "template" preparations since thermochemical treatments are needed to react away the template and this treatment invariably leads to sintering of the supported metal particles.

Direct metal-metal interactions can be arranged electrochemically [63]; yet a more ingenious method is that of electroless deposition or surface redox preparations [28,63-65], in which a reduced metal surface has sufficient reduction potential to reduce a dissolved cation of a second metal which in turn can form core-shell particles. High loading of the shell metal can be achieved, however, the depositing metal can also absorb onto itself and this autocatalytic deposition can make the formation of a contiguous metallic shell difficult. Another minor practical drawback of this method is the complexity in establishing a metastable deposition bath in some systems.

In this chapter it will be demonstrated that Strong Electrostatic Adsorption (SEA) can be applied to the synthesis of bimetallic nanoparticles. The manner in which SEA can be applied to bimetallic catalysts is depicted in figure 4.1. For the sake of completeness, in figure 4.1a dry impregnation (DI) is shown. In this method, two metal precursors are placed in solution but no provision is made for the metal precursors to interact with the support surface, and often the result is large, poorly dispersed and poorly distributed aggregates of separate metal particles. On the other hand if a mixture of

cationic precursors is placed in solution above a negatively charged surface (figure 4.1b), a mixed monolayer of precursors will be electrostatically adsorbed onto the surface and upon reduction, small, well dispersed particles with even distribution and homogeneous alloying will result. This method can be termed simultaneous or co-SEA. If instead of homogeneously alloyed particles, core-shell morphologies are desired, the sequential-SEA (seq-SEA) procedure of figure 4.1c can be followed. The core metal is initially deposited by SEA and then oxidized. With the judicious selection of a support that has a different PZC than the supported metal oxide, opposite charges can be induced on them such that a second metal precursor, the shell metal, can be selectively deposited onto the core metal oxide, which after reduction, reverts to a metal core and shell.

In this chapter, the degree of control represented in figure 4.1 will be demonstrated for several real, high surface area catalyst systems by the extension of SEA; at the same nominal catalyst composition, the plausibility of synthesizing well dispersed homogeneously alloyed or core-shell nanoparticles will be demonstrated. These “rational” preparations will be compared to the common procedure of dry impregnation.

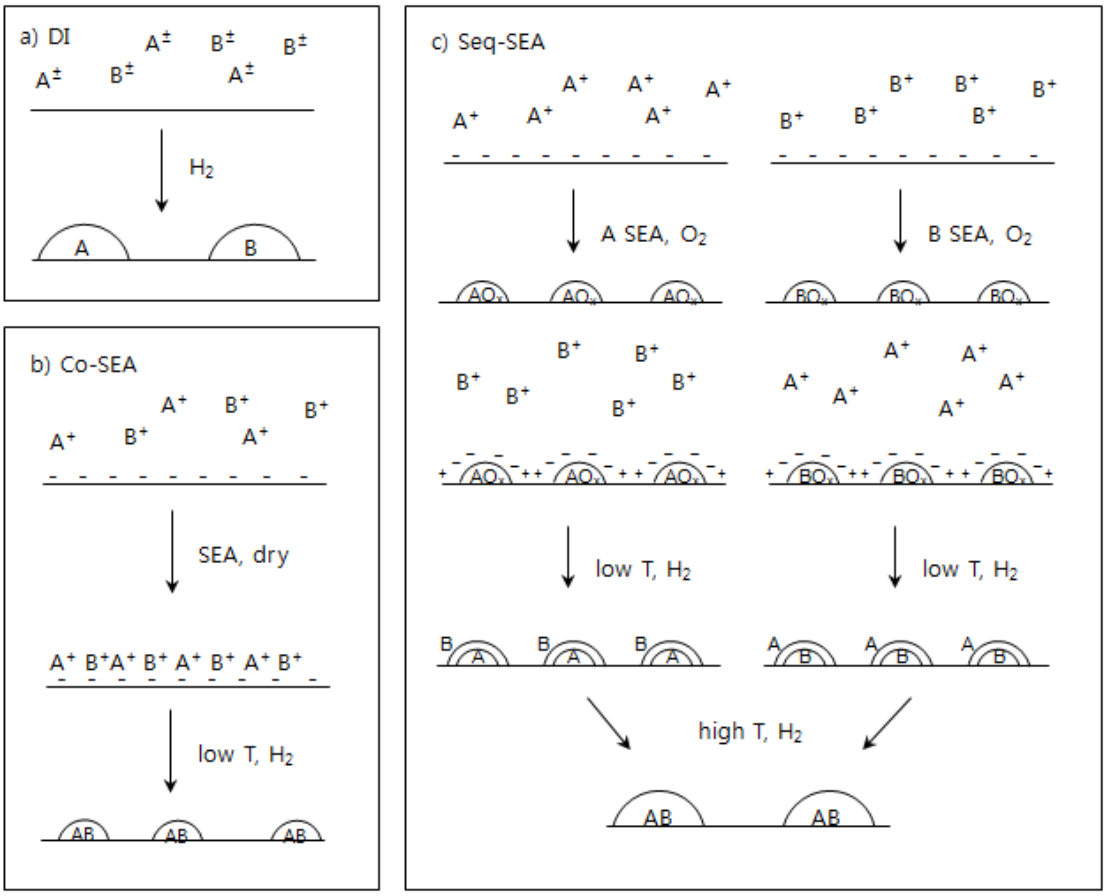

Figure 4.1 Schematic of working hypothesis for bimetallic catalyst preparation: (a) DI will produce separate metal particles, (b) co-SEA will yield highly dispersed, alloyed metal particles with low T reductions, (c) sequential SEA will give rise to highly dispersed, core-shell structures at low reduction T, and larger, alloyed particles at high reduction T.

4.1 SUPPORTED SINGLE Pt OR Pd METAL CATALYST BY SEA AND Pt/Pd ALLOY CATALYST BY CO-SEA

4.1.1 Experiments

In order to determine the optimal pH leading to maximum metal loading, adsorption surveys were conducted according to the PZC value of the supports. Oxidized Carbon -Vulcan-72ox (oxC, BET area: 170 m^2/g) and Aerosil 300 (SiO_2, BET area: 330 m^2/g) from Evonik were used as low PZC supports for the adsoprtion of cation precursors; TetraamminePlatinum(ll) Chloride([PTA, $Pt(NH_3)_4]Cl_2$, 99.999%) or Tetraamine

Palladium(ll) Chloride(PdTA, $[Pd(NH_3)_4]Cl_2$, 99.9%). Chloroplatinic acid (PHC, $H_2[PtCl_6]$, 99.9%) or Sodium tetrachloropalladium (PdTC, $Na_2[PdCl_4]$, 99.9%) were used as the anion precursors on high PZC support; a commercial γ-alumina (Al_2O_3, BET area: 277 m^2/g) from UOP and carbon (Vulcan-XC72, BET area: 254 m^2/g) from Cabot. To produce a low PZC oxidized carbon (oxC), 5-10g of C was mixed with 300ml of concentrated nitric acid and heated to around 90-95°C for 3 hours. After cooling to room temperature the slurry was repeatedly washed and filtered with deionized water until the pH of the filtrate was near a pH value of 5. The slurry was dried at room temperature overnight and then placed in a furnace with air at 300°C for 1hr.

Table 4.1 Supports and precursors

Support	PZC	Surface Area	Precursor
Silica (Aerosil 300)	3.3	330 m^2/g	PTA and PdTA
Oxidized Carbon(oxVulcan-XC72)	2	170 m^2/g	
Γ−Alumina (VGL-25)	8.5	277 m^2/g	PHC and PdTC
Carbon (Vulcan-XC72)	8.9	254 m^2/g	

Aqueous solutions of 1mM PTA or PdTA were prepared and dosed into several 50-ml flasks. The pH values of all these solutions were adjusted using HCl or NaOH between pH value of 0.5 and 13.5. PHC solution were prepared over the pH range of 0.5-10 using HCl or NaOH. Since PdTC solution can be precipitated without the presence of excess of Cl^-, PdTC salt was dissolved in DI water to make 1mM solution and 5.6 times excess Cl^- ions were added through the use of HCl to ensure stability of the complex in

solution over the required pH range [66]. HNO_3 and NH_4OH were used to adjust the pH of the PdTC solutions from 0.5 to 5, being careful to maintain a maximum pH value of 5 with NH_4OH since the anionic palladium chloride complex converts to cationic Pd ammine complex which will not electrostatically adsorb over the support surface [66]. For the co-SEA uptake survey, a mixture of 1mM of Pt and 1mM Pd solution was used.

A high PZC support was weighed out to obtain the desired 1000 m^2/L surface loading (SL) in 50 mL of solution. The low PZC support was weighed out for 500 m^2/L surface loading with 50mL solutions.

$$\text{SL}\ (\text{m}^2/\text{L}) = \frac{\text{mass of solid}\ (\text{g}) \times \text{oxide surface area}\ (\text{m}^2/\text{g})}{\text{Volume of solution}\ (\text{L})}$$

Each support powder was added to 50mL of each pH adjusted solution and shaken for 1 hour. Final pH values were measured and 5mL of slurry solution was filtered for Inductively Coupled Plasma (ICP, Perkin-Elmer Optima 2000DV) analysis. Initial solutions which were not contacted with support, at each pH value, were also measured with ICP to establish initial concentrations. Pt and Pd calibration standards were diluted from a 10,000 ppm Pd and 10,000 ppm Pt stock solutions. The calibration curves were obtained for 200 and 500ppm of Pt and Pd solutions.

Adsorption data is plotted with the final pH values along the x-axis and platinum (or palladium) adsorption along the y-axis as Γ (μmol/m^2). The optimal final pH was obtained by the above adsorption experiments.

$$\Gamma(\mu mol/m^2) = (Conc_{inital} - Conc_{final})(mg/L)\frac{10^6\,(\mu mol/mol)}{Surface\,Loading\,(m^2/L) * Mw\,of\,Metal\,(g/mol) * 1000\,(mg/g)}$$

To synthesis the amount of catalyst needed for characterization and reactivity evaluation, the adsorption survey experiment was simply scaled up to 1L at optimal pH;

3.0 g of silica or 5.9 g of oxC was added into 1 mM PTA solution or 1 mM PdTA solution. After shaking 1 hour, the slurry was filtered, dried and reduced to make Pt/SiO_2, Pd/SiO_2, Pt/oxC and Pd/oxC. Pt/Al_2O_3, Pd/Al_2O_3, Pt/C and Pd/C were also made by same process with either 1 mM PHC solution or 1 mM PdTC solution.

Samples prepared by co-SEA were produced in the same manner with mixed solution of 1 mM Pt and 1 mM Pd at the optimal uptake pH. All samples were dried at room temperature overnight and then reduced for 1hr with $10\%H_2$/He at the appropriate temperature based on TPR with a ramp rate 2.5°C /min.

4.1.2 Characterization

A. XRD

Powder XRD measurements were made using a Rigaku MiniFlexII bench-top system. XRD patterns were compared to reference spectra using PDXL 2.0 (Rigaku Corporation) software. The radiation source was Cu Kα radiation (λ = 1.5406 Å) at operating condition of 30kV and 15mA. All spectra were taken at a scan rate of 0.5^o/min and sampling width of 0.02^o.

B. TPR

Micromeritics Autochem ll 2920 used for TPR, the flow rate was 50cc of 10% H2/He, the temp range from 25°C to 800°C and ramp rate was 5°C/min. TCD signal recorded every 0.1sec. Mass spec used fixed-bed quartz reactor and dried in He at 110 °C for 60 min then, the sample was cool down to RT and TPR profiles were obtained by flowing 1% H2/Ar gas mixture form 25 to 500 °C with a ramp of 5 °C/min.

C. STEM and EDXS

Scanning transmission electron microscopy (STEM) at USC was used to obtain

images of co-SEA and co-DI catalysts with a JEOL 2100F 200kV FEG-STEM/TEM equipped with a CEOS Cs corrector on the illumination system. The geometrical aberrations were measured and controlled to provide less than a $\pi/4$ phase shift of the incoming electron wave over the probe-defining aperture of 17.5 mrad. High angle annular dark-field (HAADF) STEM images were acquired on a Fischione Model 3000 HAADF detector with a camera length such that the inner cut-off angle of the detector was 50 mrad. The scanning acquisition was synchronized to the 60 Hz AC electrical power to minimize 60Hz noise in the images and a pixel dwell time of 15.8μs was used.

The JEM-ARM200CF at the U. Illinois at Chicago was used for images and elemental mappings of seq-SEA and co-DI catalysts. The JEM-ARM200CF is a probe aberration corrected 200kV STEM/TEM with a cold field emission source with 0.35eV energy resolution. For HADF imaging at 200kV this instrument has a resolution of less than 0.08nm. STEM images can be collected from up to four of the five STEM detectors simultaneously. For microanalysis the microscope is equipped with an Oxford X-max 80 SDD X-ray detector. Probe size 1A, probe current 14 Pa, 20um aperture. 256 pixel resolution, pixel dwell time is microseconds, using oxford instruments X-Max TLE 100mm^2 detector with about 0.7 Sr solid angle of collection, most of maps collected within 5min, short collection time to ensure core-shell maintains integrity.

D. Catalytic Activity: Oxidation of Diesel Exhausted Gas

JMTC in the UK has evaluated several Pt/Pd catalysts for abatement of a model diesel exhaust mixture. They used 0.1g catalyst in a ‘Diesel 4HC' test. Gas composition is 5% CO_2, 5% H_2O, 14% O_2, 1500ppm CO, 150ppm NO, 40ppm CH_4, 37ppm propylene, 26ppm decane and 16ppm toluene in N_2 carrier. The bed of catalyst pellets is maintained

at 110°C before ramping at 10°C/min to 500°C. Gas flow through the bed is 2L/min. Aging treatment are calcination at 500°C for 2hrs, and at 750°C for 10hrs.

4.1.3 Results and Discussion

A. Uptake survey of single metal adsorption by SEA

In figure 4.2a the maximum adsorption of cationic Pt ammine on silica is observed to be 1.0 μmol/m^2 and Pd ammine maximum adsorption is 1.3 μmol/m^2, both with volcano shaped uptake patterns typical of SEA. On oxC (figure 4.2b), Pd ammine adsorption is slightly increased when compared to silica, whereas the maximum adsorption density of Pt is the same as on silica. Because the PZC of oxC is lower than silica, the adsorption plateaus are wider than for silica.

The maximum adsorption density of Pt chloride anions is about 2.0 μmol/m^2 on alumina and 1.8 μmol/m^2 on carbon (figure 4.2c and d). The adsorption of Pd chloride is considerably different between alumina and carbon. Carbon absorbs significantly more Pd chloride than alumina; maximum Pd adsorption is 1.0 μmol/m^2 on carbon, and 0.6 μmol/m^2on alumina.

a)

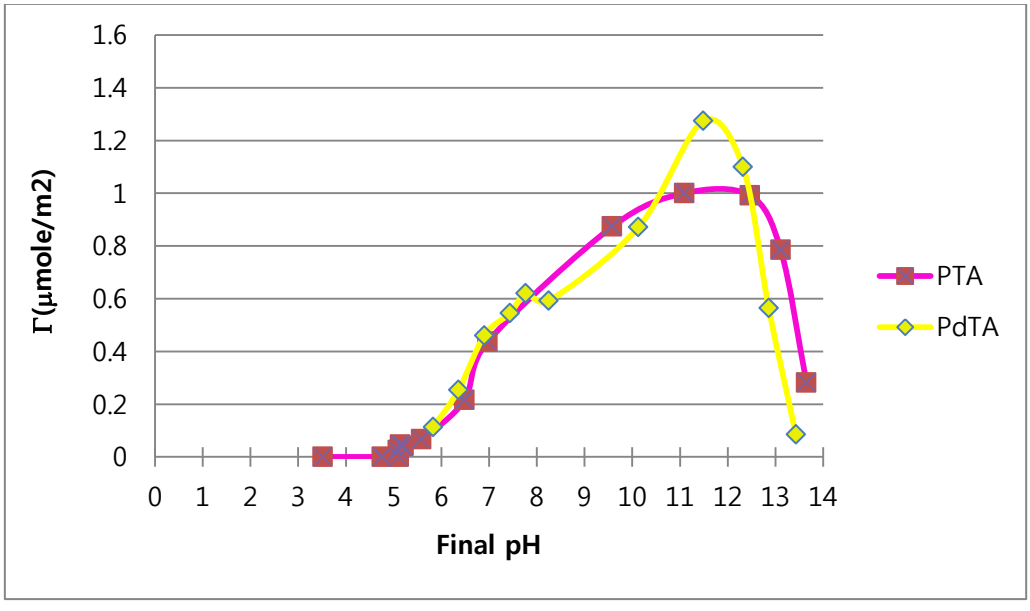

b)

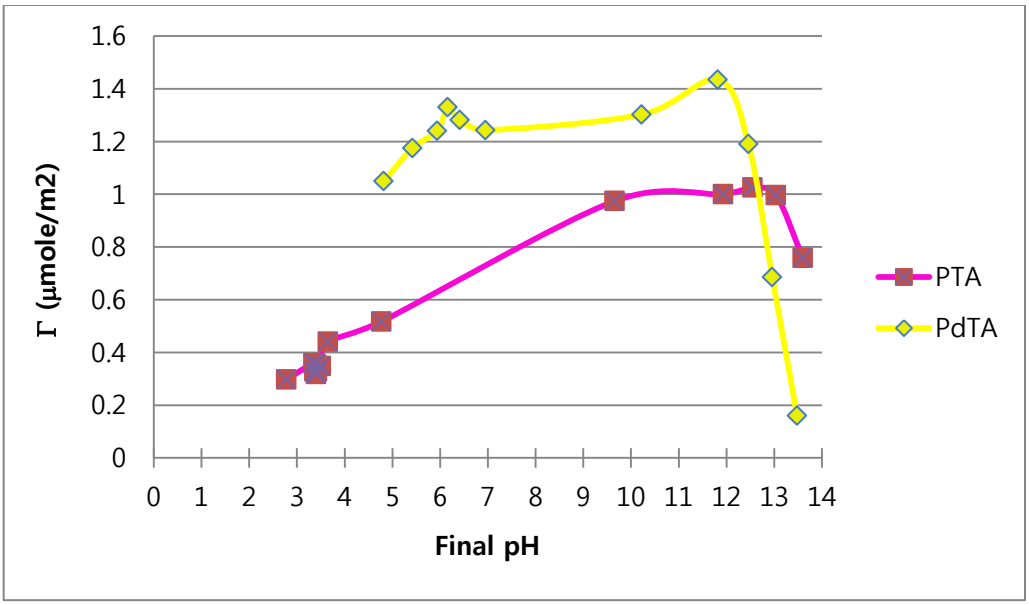
1.6
1.4
1.2
1
0.8
0.6
0.4
0.2
0
Γ (µmole/m2)
0 1 2 3 4 5 6 7 8 9 10 11 12 13 14
Final pH
PTA
PdTA

c)

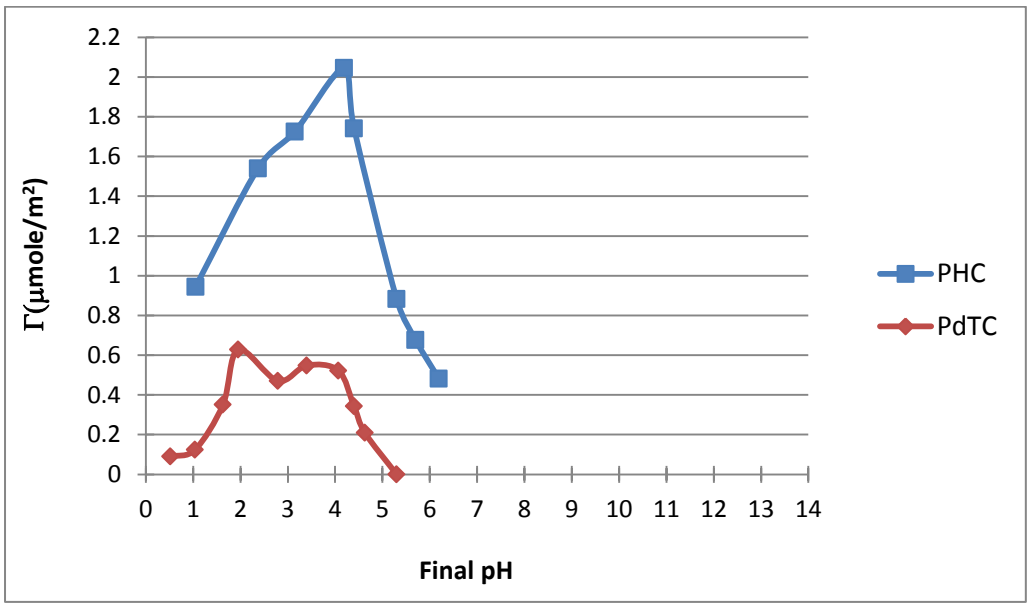
2.2
2
1.8
1.6
1.4
1.2
1
0.8
0.6
0.4
0.2
0
Γ(µmole/m²)
0 1 2 3 4 5 6 7 8 9 10 11 12 13 14
Final pH
PHC
PdTC

d)

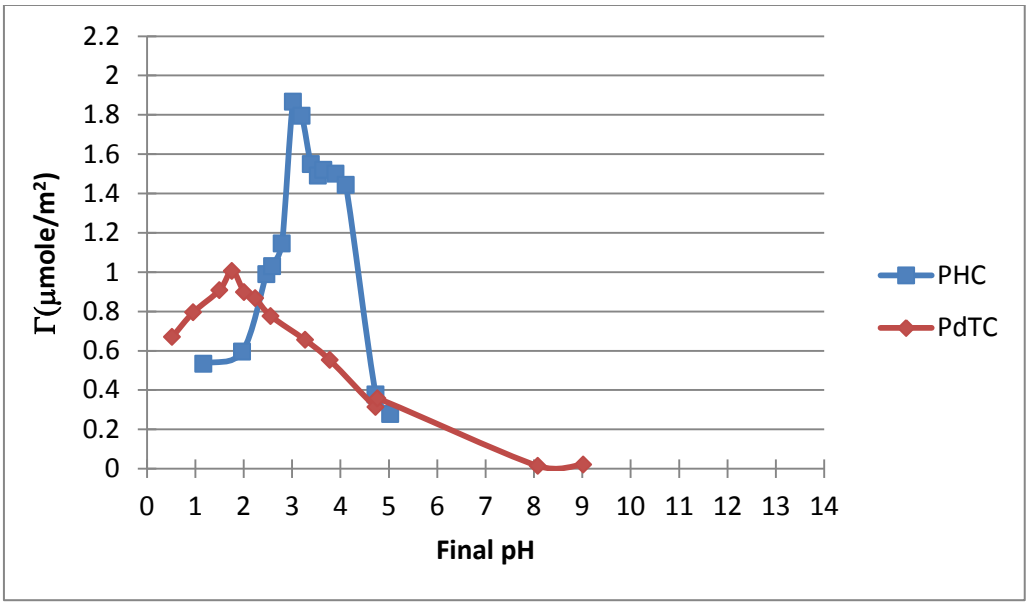

Figure 4.2 Single metal adsorption on a) SiO_2 b) oxC c) Al_2O_3 d) C

B. Uptake survey of two metal adsorption by co-SEA

The uptake of metals from a mixture of Pd and Pt ammines is shown in figure 4.3a. Pd cations dominate Pt cations when adsorption occurs at medium pH, while Pt cations dominate Pd cations when adsorption occurs at high pH. Maximum total metal adsorption density over silica is 1.3 μmol/m^2, the same as single metal Pt maximum adsorption (figure 4.2a). Figure 4.3b shows Pt and Pd cations are more evenly adsorbed though Pd pre-dominates slightly at neutral pH over oxC. Both contribute to increase of total metal adsorption density (1.9 μmol/m^2). The higher adsorption densities may arise from the sharing of hydration sheaths between two metals.

The anionic precursors (figure 4.3.c and d) exhibit different trends from the cationic ones. Total metals maximum adsorption density is always lower than single metal adsorption; total maximum adsorption density on alumina is 1.24 μmol/m^2 and 1.1 μmol/m^2 on carbon but single metal Pt maximum on alumina is 1.64 μmol/m^2 and 2.0

μmol/m^2 (figure 4.2c and d). PHC generally dominates over PdTC in the adsorption process at all acidic pHs. Therefore, total metals adsorption does not occur at a value higher than that of the case of a single metal.

a)

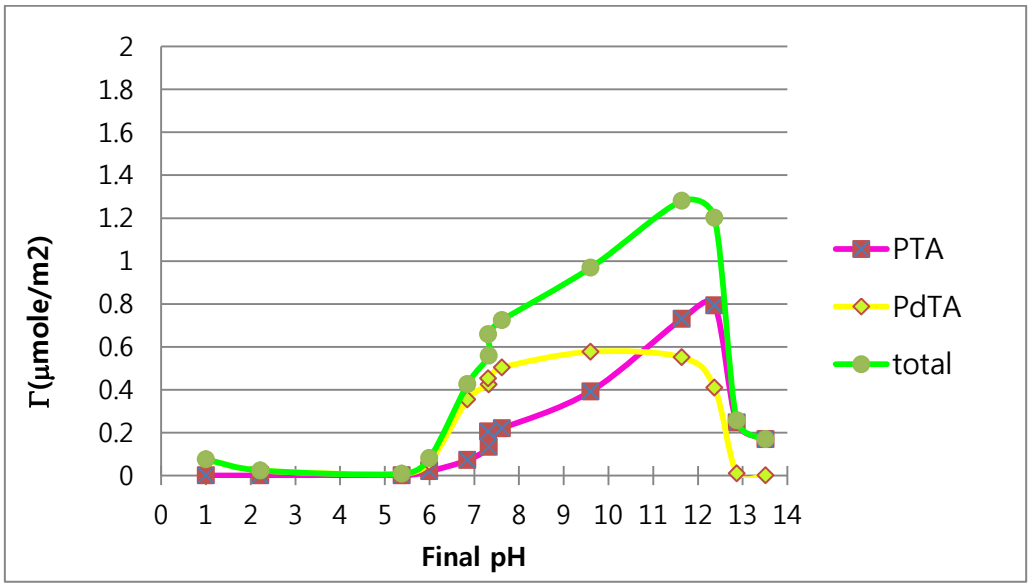

b)

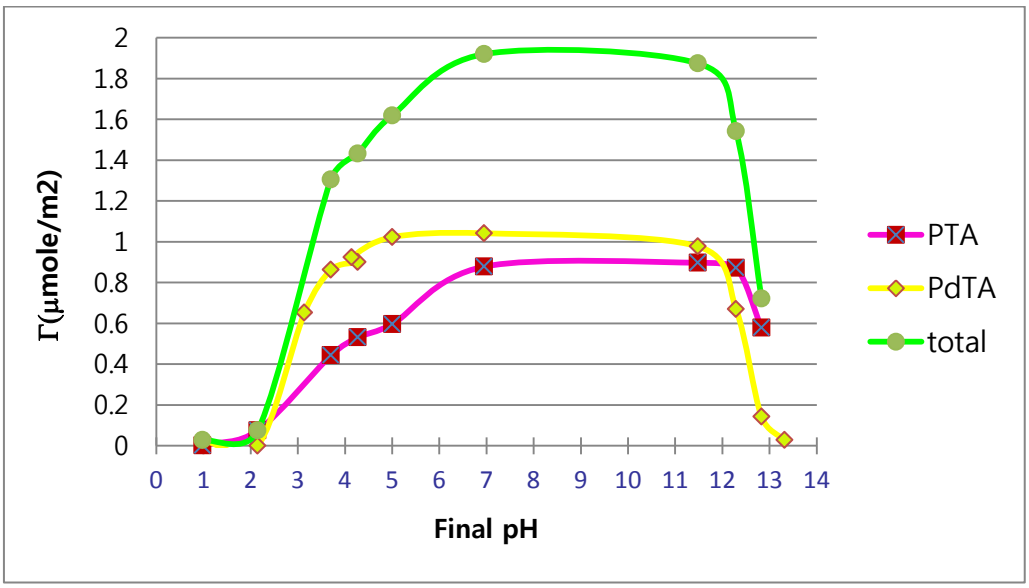

c)

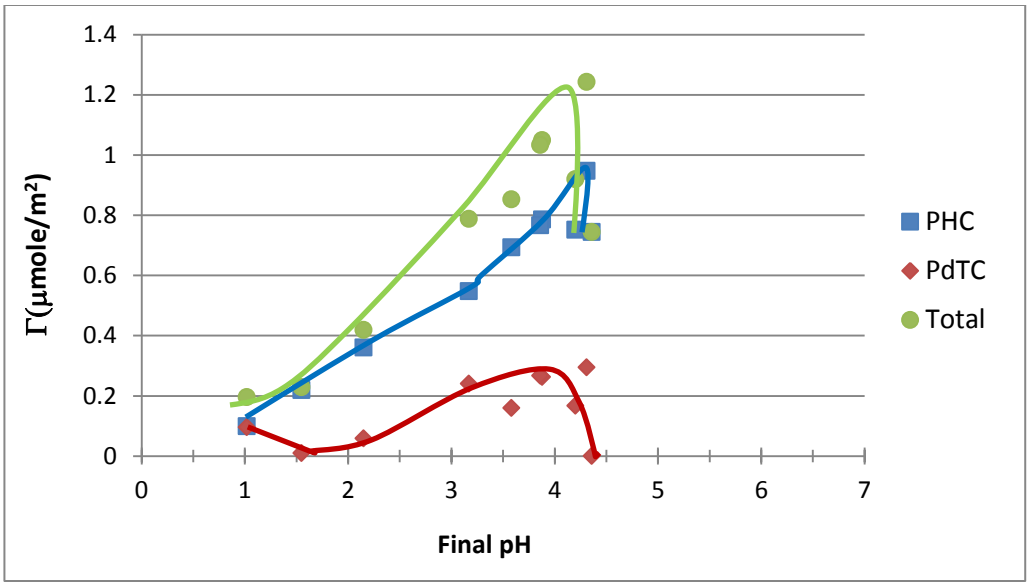

d)

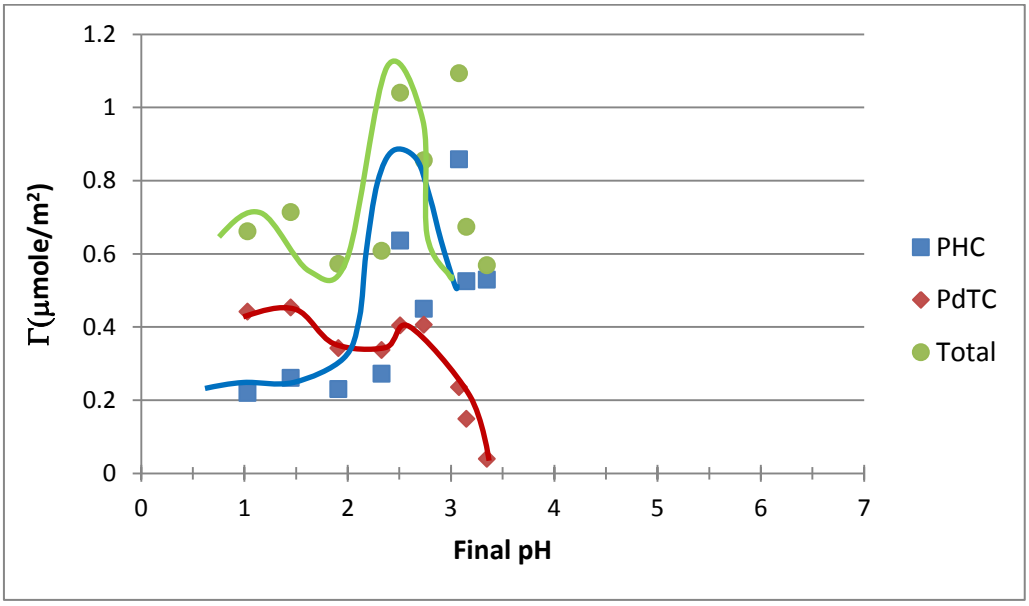

Figure 4.3 Two metal co-SEA adsorption on a) SiO_2 b) oxC c) Al_2O_3 d) C

Table 4.2 summarizes the metal loading of each catalysts prepared at the pH of maximum uptake. The results of co-SEA with cation precursors show that higher wt% can be produced versus single metal SEA, but anion precursors do not adsorb more densely in combination and this leads to co-SEA with chloride precursors yielding bimetallic catalysts with lower metal weight loading than single metal SEA.

Table 4.2 Metal wt% of each catalyst by ICP result

Support	Type	Pt wt%	Pd wt%
silica	Single Pt SEA	5.0	-
	Single Pd SEA	-	4.0
	Pt-Pd co-SEA	4.5	2.0
oxC	Single Pt SEA	3.0	-
	Single Pd SEA	-	2.5
	Pt-Pd co-SEA	3.0	1.8
alumina	Single Pt SEA	11	-
	Single Pd SEA	-	2.1
	Pt-Pd co-SEA	5.3	1.6
C	Single Pt SEA	8.3	-
	Single Pd SEA	-	2.7
	Pt-Pd co-SEA	4.0	1.0

C. Temperature Programmed Reduction (TPR)

Temperature programmed reduction results for all catalysts listed in table 4.2 are shown in figure 4.4. Figure 4.4a shows that PdTA on silica can be reduced at lower temperature (180^{o}C) than PTA (210^{o}C) and the reduction temperature of co-SEA sample is as low as PdTA, likely from H_2 spillover from Pd. Over oxidized carbon (figure 4.4b) the methanation of carbon occurs at elevated high temperature near 620^{o}C for the metal free support, but after Pt and Pd adsorption, the methanation temperature decreased to near 450^{o}C and the reduction temperature also can be reduced to a value lower than the single metal reduction temperature. The mass spectrogram of ammonia in figure 4.4c, for the PdTA sample in figure 4.4b, confirms that the decomposition of PdTA has a double peak.

PHC on alumina reduced at 210^{o}C (figure 4.4d) and PdTC reduced completely at 150^{o}C. But co-SEA exhibits only one peak near 180^{o}C, while co-DI has one peak near 180^{o}C and another small peak near 210^{o}C. This suggests that co-SEA on alumina produced alloyed particles and co-DI produced both alloyed and Pt only particles. Figure

4.4e does not manifest the alloy effect on co-SEA because the Pt wt% is much higher than that of Pd.

a)

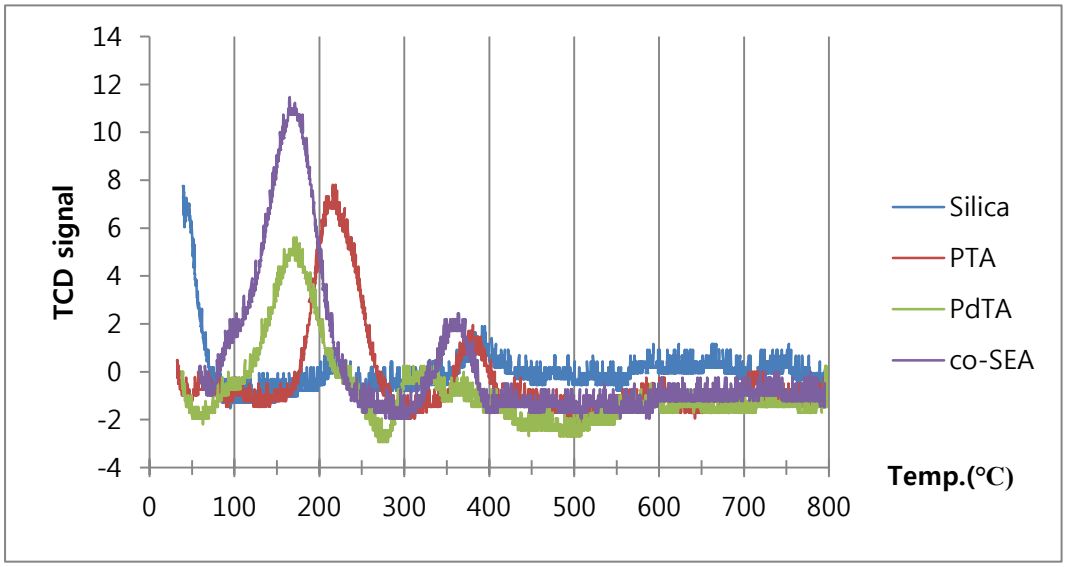

b)

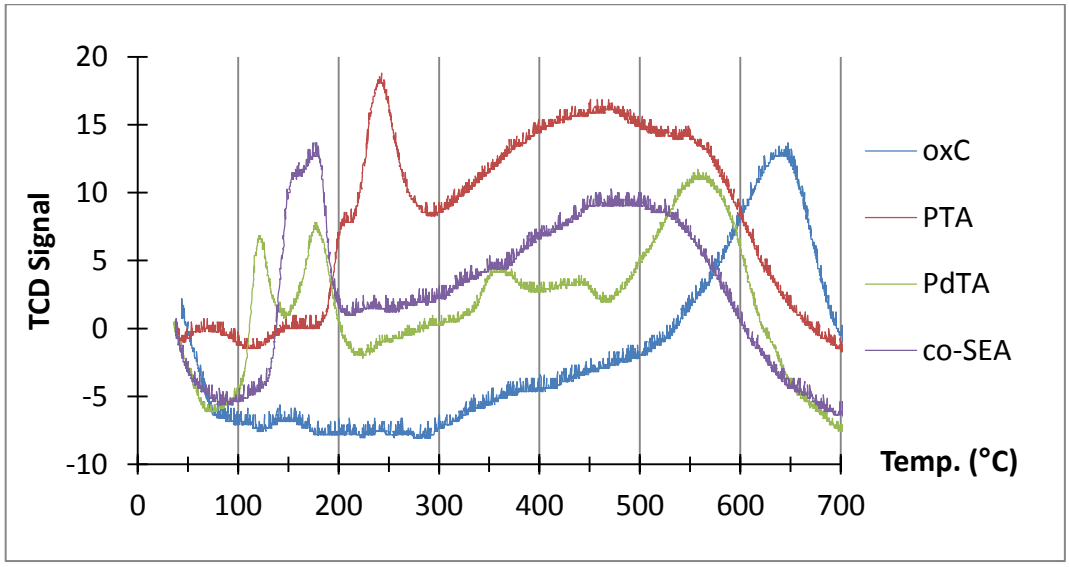

c)

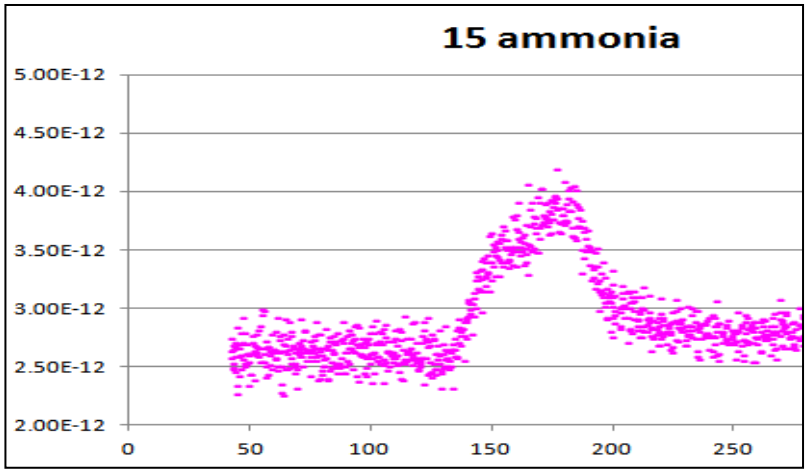

d)

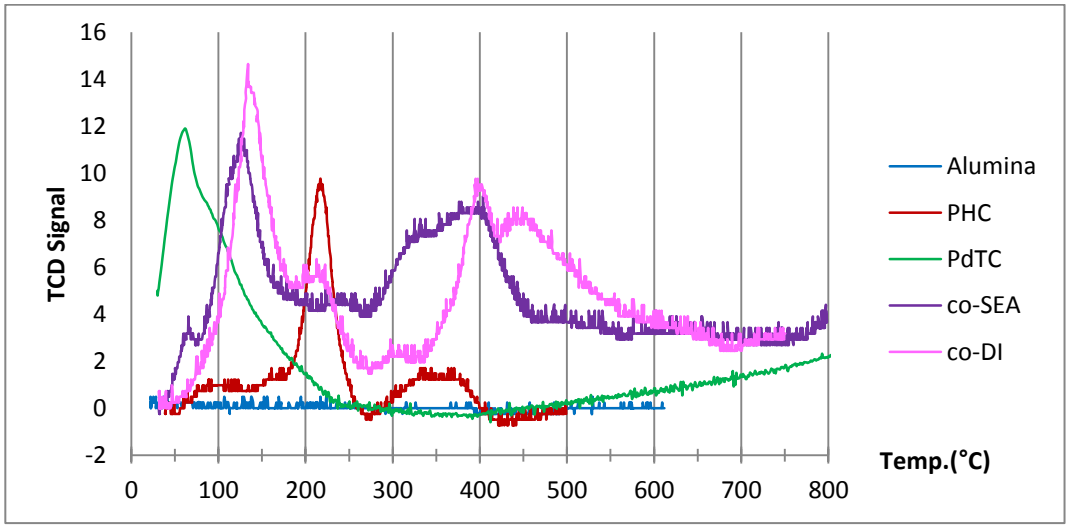

e)

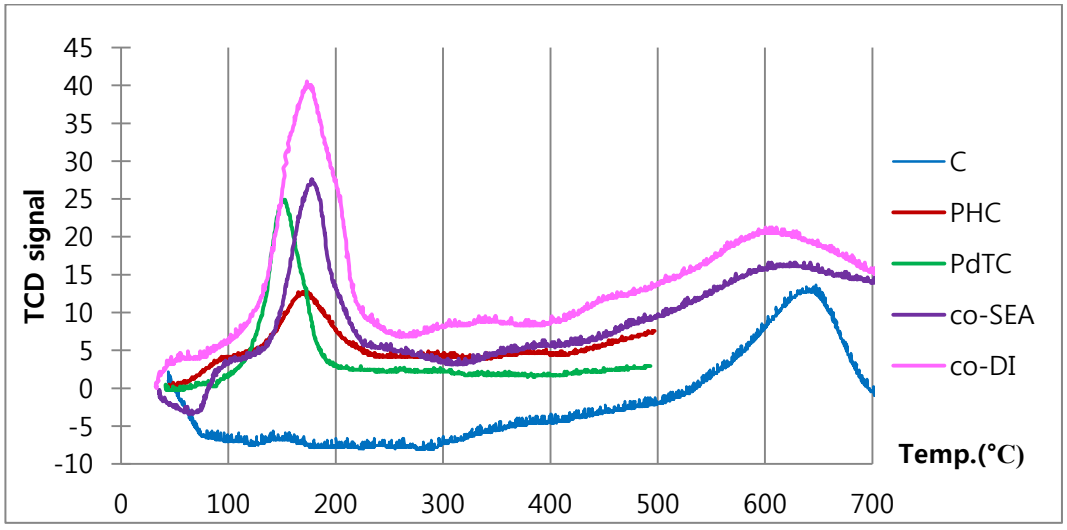

Figure 4.4 TPR results over a) silica b) oxC c) Mass-spec of PdTA on oxC d) alumina e) C

D. X-ray Diffraction (XRD)

Catalysts were reduced at the appropriate temperature based on TPR results in figure 4.4. The four series of catalysts, consisting of individual Pt and Pd nanoparticles prepared by SEA, and Pt/Pd bimetallic particles prepared by co-SEA and co-DI, over the four supports; silica, oxC, alumina and unoxidized C, were next characterized by powder XRD. These results are shown in figure 4.5.

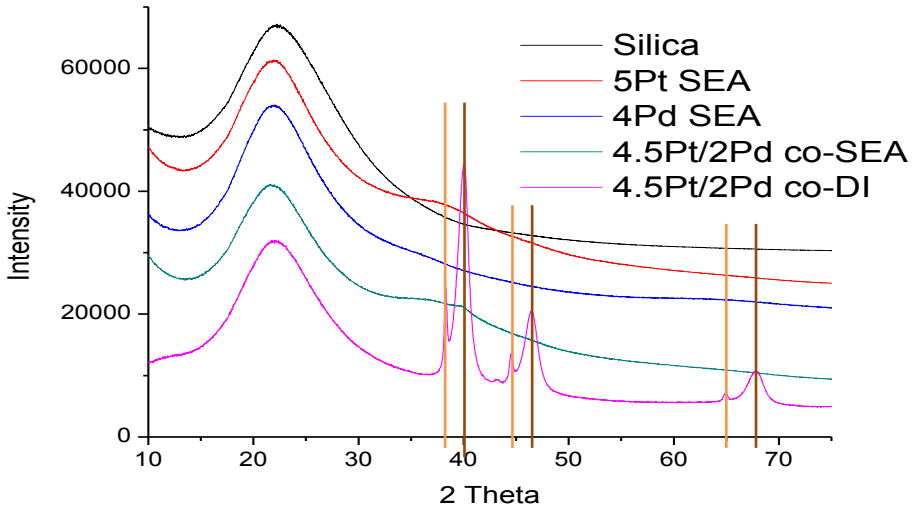

a)

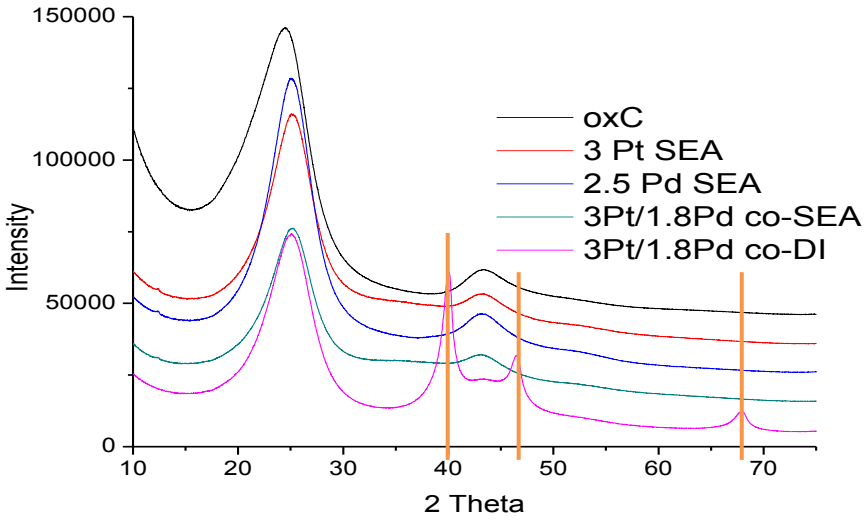

b)

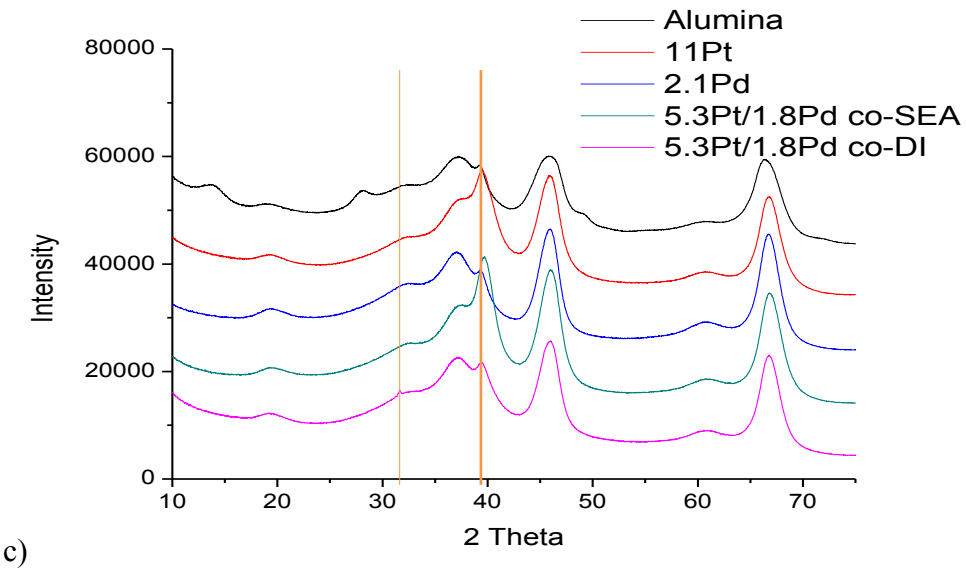

c)

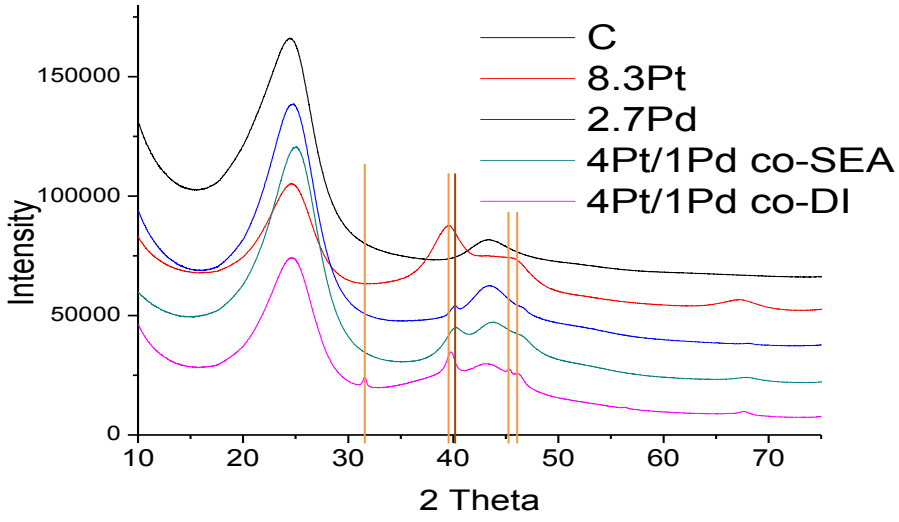

d)

Figure 4.5 XRD result a) Silica b) oxC c) Alumina d) C

In figure 4.5a, wide Pt_3O_4 (210) and (211) peaks are only detected over both silica supported monometallic Pt catalyst synthesized by SEA and bimetallic Pt-Pd catalyst produced by co-SEA. Using the Scherrer equation, the estimated particle sizes of monometallic Pt and co-SEA are determined to be 1.3nm. No Pd crystal peaks appear over either SEA or co-SEA cases.

Over oxC, neither Pt nor Pd crystalline peaks are detected (figure 4.5b). The metal

particles may be too small to be detected by XRD or the metal phase is still amorphous, although TPR (figure 4.4) suggests reduction temperature is low enough to reduce the metal precursors. Pt particle size may be smaller on oxC than silica because of the interaction between Pt cation and the oxC support may be stronger than on silica.

The high PZC supports, alumina and unoxidized C, exhibit the CEDI effect (chapter 2) in co-DI samples. The PHC precursor has a low inherent pH which induced charge on the high PZC surfaces. Particles are smaller than the cationic cases (figure 4.5 a and b) but multiple phases are detected by XRD analysis; crystalline Pt oxide, Pd and Pt-Pd alloy. Meanwhile, co-SEA has only one fcc crystal phase, that of the Pt-Pd alloy.

E. Scanning Transmission Electron Microscopy (STEM)

High resolution z-contrast images, EDXS line scans, and EDXS nanoparticle maps of the four sets (silica, oxC, alumina, and C supported) of co-SEA and co-DI catalysts are given in figure 4.6. The average particle size from image analysis of these catalysts is compared to XRD results in Table 4.3. On SiO_2, co-SEA particles (figure 4.6a) have average size of 1.1nm, consistent with XRD (1.2 nm), and are speckled in appearance. Inn these z-contrast images, the brighter atoms in the particles are most certainly individual Pt atoms (as opposed to, say, vertical columns of Pd), while the darker atoms are Pd. The homogeneity of the alloying is evident by the even speckling of the particles. Maps of individual nanoparticles were not possible given the insulating (and therefore unstable) nature of the silica in the electron beam, however line scans across particles, as seen in figure 4.6a, additionally confirm the simultaneous presence of Pt and Pd. This was found to be the case in all of the four particles line-scanned. Turning to the co-DI silica sample in the lower portion of figure 4.6a, although the average particle size was

calculated by image analysis (table 4.3) to be 4.7nm, some of particles are large (~50nm), agglomerated and non-uniform. The small sampling size of STEM is the reason for the discrepancy in the size estimates of STEM and XRD (20 nm). Furthermore, EDXS scans of the large metal agglomerates revealed that parts of the agglomerates are Pd rich and others are Pt rich.

In Figure 4.6b, the co-SEA catalyst supported on oxC is seen to be well dispersed with uniformly distributed 1.0 nm (consistent with XRD) particles. The conductive carbon supports are sufficiently stable in the electron beam so that individual nanoparticle maps can be obtained; a representative map (one of four obtained) again reveals the homogeneity of alloying of Pt and Pd in the nanoparticle. The co-DI particles on oxC are once again nonuniform in size, shape, and distribution. The small sampling size of STEM explains the discrepancy of the STEM size estimate (2.0 nm) to XRD (18 nm).

STEM analysis of the alumina supported materials is shown in figure 4.6c. The co-SEA sample once again possesses well dispersed, uniformly distributed particles, with a STEM-estimated particles size (1.7 nm) in good agreement with XRD (2.0 nm). A representative line scan (one of x) again reveals the simultaneous presence of both metals. While the co-DI sample was seen by XRD to have relatively small particle size (3.0 nm) by the CEDI effect as mentioned previously, STEM imaging reveals that the metals can still aggregate over the alumina support with co-DI. The distribution of nanoparticles appears to be much more uniform with co-SEA.

Stem imaging of the unoxidized carbon-supported nanoparticles is given in figure 4.6d. Co-SEA with the anionic chloride precursors over unoxidized carbon appears to be essentially parallel to co-SEA with cationic ammine precursors over oxidized carbon in

figure 4.6a. STEM particle size with co-SEA on C is 1nm, in reasonable agreement with XRD (1.5 nm); the particles are relatively well dispersed and evenly distributed, whereas the small sampling size explains the discrepancy of the co-DI STEM size estimate (1.1 nm) with XRD (4.0 nm). In the entire STEM analysis, the small sample size is less of a problem for the co-SEA-derived nanoparticles because the size distributions are relatively tight. Finally, the representative nanoparticle maps in figure 4.6d reveal relative homogeneity of alloying in both the co-SEA and co-DI samples, the latter occurring likely due to the CEDI effect.

Table 4.3 Average particle size (nm) analysis

Support	Silica		oxC		Alumina		C	
Method	co-SEA	co-DI	co-SEA	co-DI	co-SEA	co-DI	co-SEA	co-DI
XRD	1.2	20	<1.5	18	2.0	3.0	1.5	4.0
STEM	1.1	4.7	1.0	2.0	1.7	2.0	1.0	1.1

a)

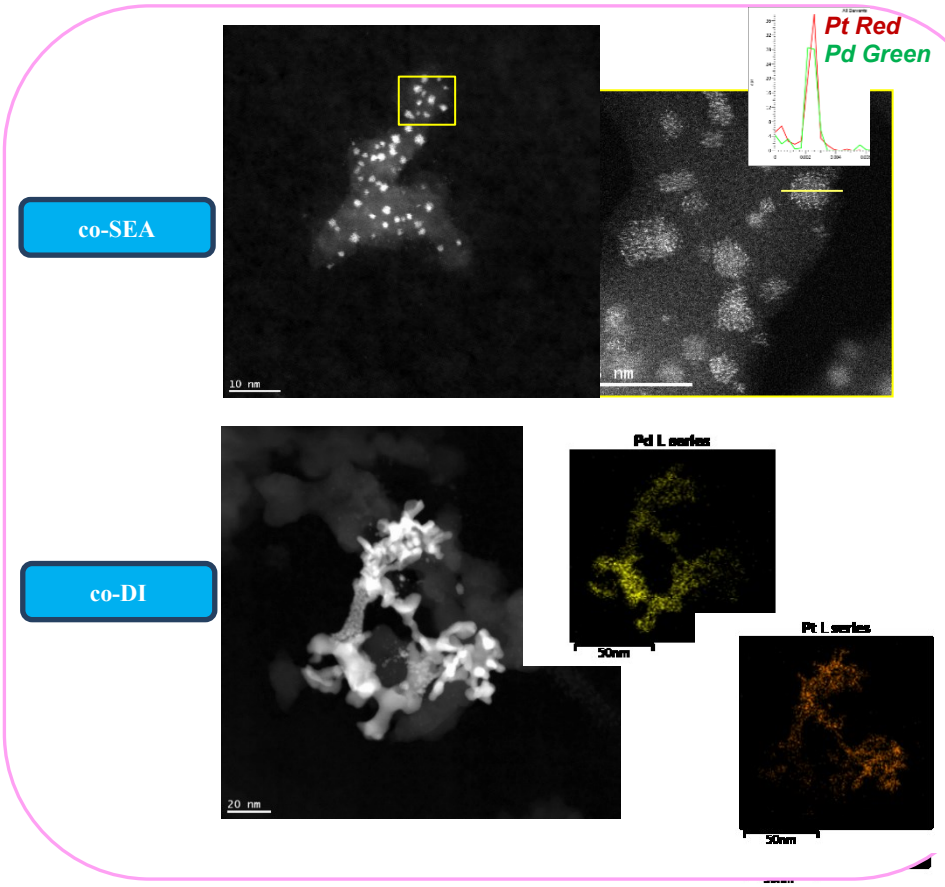
co-SEA
Pt Red
Pd Green
10 nm
nm
co-DI
Pd L series
50nm
Pt L series
50nm
20 nm

b)

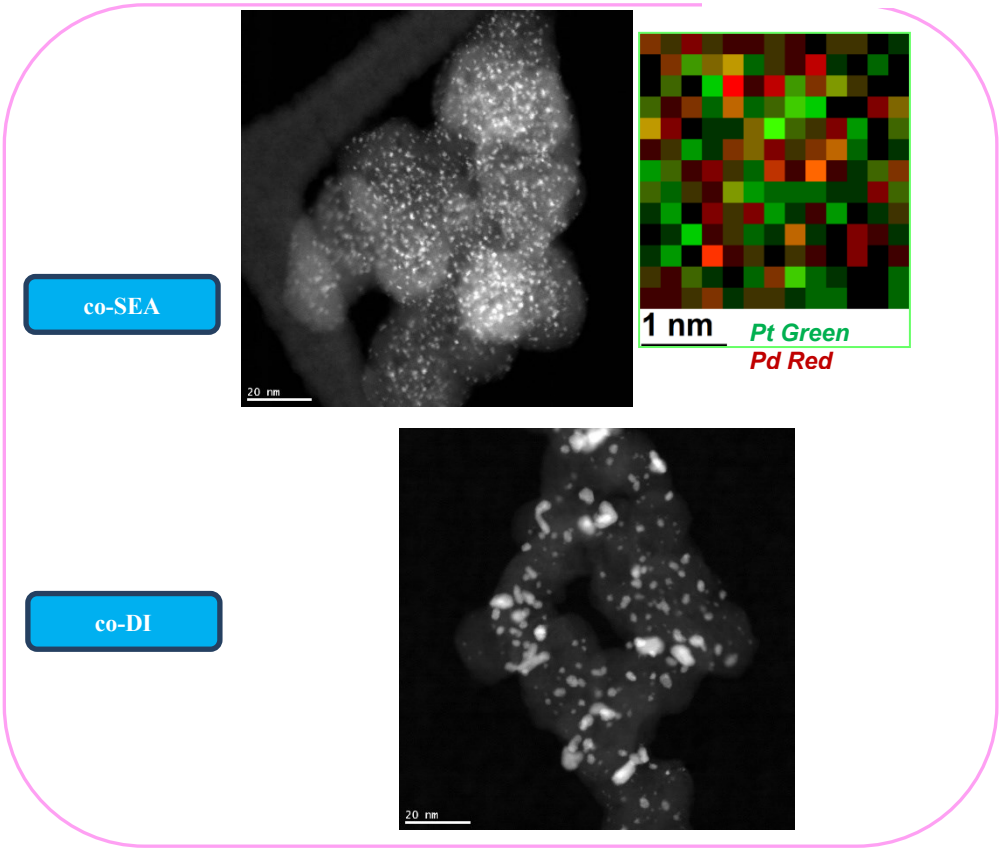
co-SEA
20 nm
1 nm
Pt Green
Pd Red
co-DI
20 nm

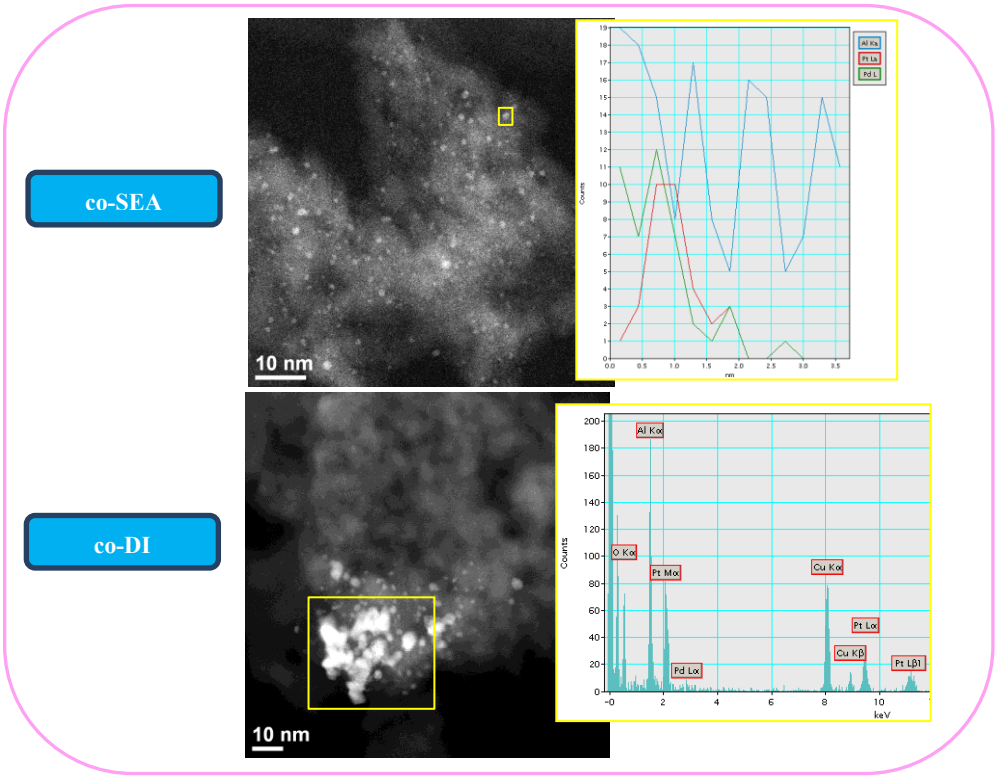

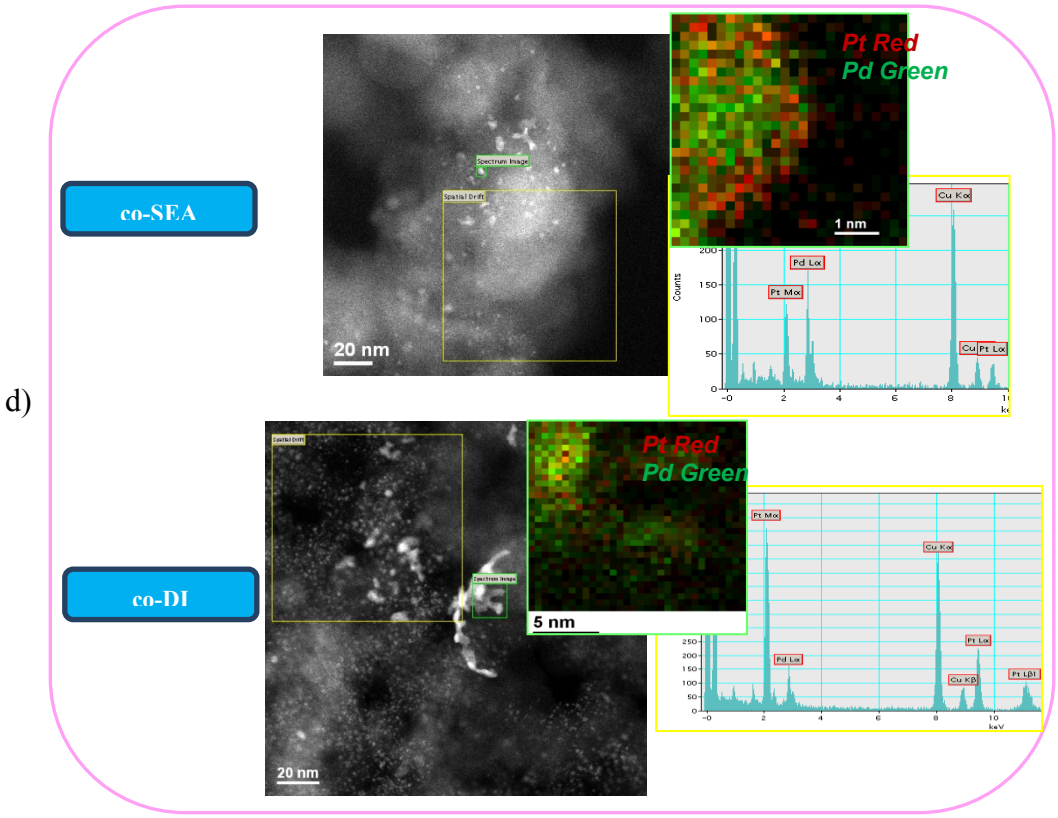

Figure 4.6 STEM and EDXS a) silica b) oxC c) alumina d) C

4.2 ALUMINA OR SILICA SUPPORTED Pd/Pt CORE-SHELL BIMETALLIC CATALYST BY SEQ-SEA

4.2.1 Experiments

A. Uptake survey of seq-SEA

In the preceding section, co-SEA has been used to synthesize homogeneously alloyed nanoparticles. In this section, attention is turned to core/shell morphologies. Recalling figure 4.1, a second metal precursor, the shell metal, will be adsorbed onto the first supported metal oxide, or the core metal. PHC has been used for Pt shells on SEA-derived Pd/SiO_2, PTA for Pt shells on SEA-derived Pd/alumina and PdTA for Pd shells on SEA-derived Pt/alumina.

The first step in the application of seq-SEA is to determine the optimal pH leading to maximum metal 2 loading on the metal 1 oxide. To this end, adsorption surveys were conducted in pH ranges appropriate for the PZCs of the metal 1 oxide and oxide support. An uptake survey of Pt (or Pd) 200ppm precursor is conducted with the same methodology as in section 4.1.1. The only difference is calculation of the appropriate amount of 4wt%Pd/SiO_2 (or 2wt%Pd/Al_2O_3 or 6wt%Pt/Al_2O_3) for a desired 1000 m^2/L (or 500 m^2/L) surface loading. For seq-SEA, only the Pd oxide surface area (metal 1 oxide) is used to calculate the area of adsorption. For example, it is assumed that all PdO particles are hemispherical and the average diameter is 1.0 nm on SiO_2 (confirmed by STEM). The surface area of each PdO is $4\pi r^2/2 = 1.57nm^2$ and the volume of each PdO is $2\pi r^3/3 = 0.26nm^3$. Bulk PdO density is 8.3 g/cm^3. The number of PdO particles in 1 gram of PdO/SiO_2 is calculated as

$$\frac{\#\ of\ PdO}{1g\ of\ PdO/SiO2} = \frac{0.04g\ PdO}{Volume\ of\ PdO/EA} * \frac{1}{Density\ of\ PdO} * (\frac{1m}{100cm})^3 * (\frac{10^9 nm}{1m})^3$$

*# of PdO * 1.57nm^2(Surface Area of each PdO) = SA of PdO in 1g of PdO/ SiO_2*

In this calculation, $1.85*10^{19}$ particles of PdO exist in 1g of PdO/SiO_2 and their total surface area (SA) in1g of PdO/SiO_2 is 29.1m^2/g. After finding out the SA of all PdO nanoparticles, the 34.4 grams of PdO/SiO_2 is needed for 1000 m^2/L (SL) of PdO.

(1000m^2/L)/(SA of PdO in 1 g of PdO/SiO_2) = (1000m^2/L)/(29.1m^2/g) = 34.4g/L

B. Catalyst synthesis

The PZC of PtO_2 is determined to be 1.0 as shown in chapter 3. The versatility of sequential SEA can be demonstrated by synthesizing in parallel Pd shell/Pt core over high PZC supports, and Pt shell/Pd core over low PZC supports. The first scheme is illustrated in figure 4.7a. For Pt cores, Pt anions can be electrostatically adsorbed onto Al_2O_3, which has a high PZC. After reduction, the ultrasmall Pt nanoparticles spontaneously oxidize to become supported PtO_2 particles. Because PtO_2 has an extremely low PZC, Pd cations selectively adsorb over deprotonated PtO_2 surface instead of protonated alumina surface, and will then form a core-shell structures after reduction. The scheme illustrated in figure 4.7b can work if the PZC of PdO is higher than the PZC of support materials that is, if PdO can adsorb anions at low pH.

At the optimal pH, metal 2 precursor solution deposits onto appropriate metal 1 oxide over support. After shaking for 1 hour, the slurry is filtered, dried at room temp for 48hrs and then reduced for 1hr with 10%H_2/He at appropriate temperature and the ramp rate is 2.5°C /min.

(a) High PZC support

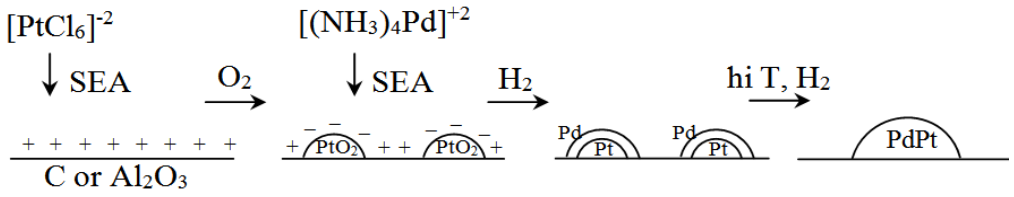

(b) Low PZC support

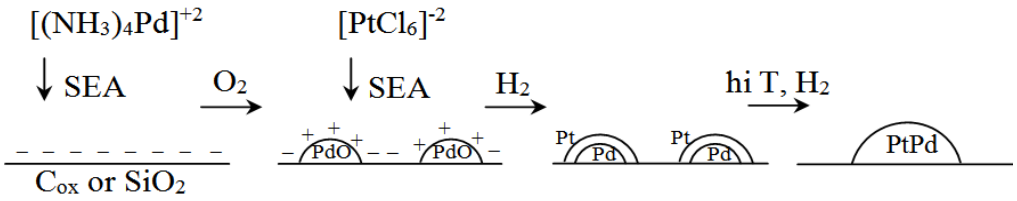

Figure 4.7 Sequential SEA for the synthesis of a) Pt core@Pd shell particle and b) Pd core@Pt shell particle.

A drawback of SEA is illustrated in figure 4.8. The surface coverage of a metal 2 precursor shrinks significantly as it reduces and loses its hydration layer(s) and ligand sphere. Therefore, in a single SEA shell application, only a fraction of a monolayer can be synthesized. Sequential SEA cycles (adsorption, reduction, reoxidation of the core metal) can be employed to build up the loading of the shell metal.

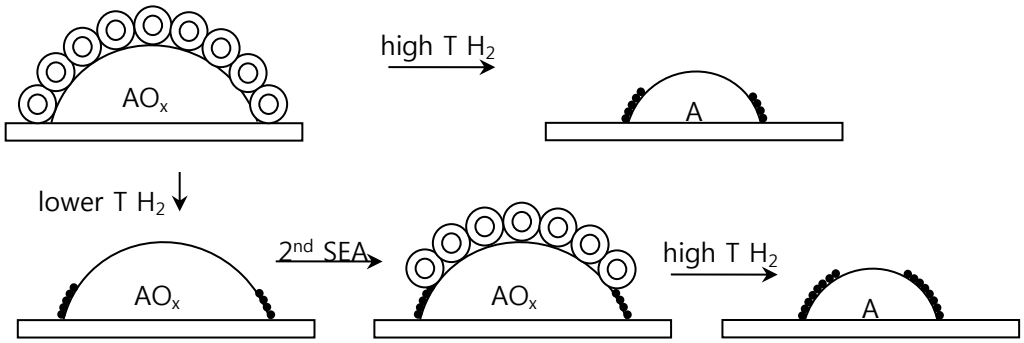

Figure 4.8 SEA/reduction cycles to build shell metal loading

4.2.2 Result and Discussion

A. Uptake survey for selective adsorption

Uptake surveys of PdTA over alumina, pure Pt oxide, and Pt/alumina are shown in figure 4.9a. Alumina has almost no uptake of PdTA but there is a broad and notably high uptake of PdTA over a pH range from 3 to 11 on pure PtO_2. The PdTA uptake graph over Pt/A catalyst is similar to the one over pure PtO_2. Pt particles in Pt/alumina catalyst are assumed to be so small that they spontaneously oxidize in air.

In same way, PTA can be adsorbed onto PdO instead of alumina, as shown in figure 4.9b. Pure PdO has high uptake of PTA in the basic pH range and Pd/alumina catalyst also exhibits the typical volcano shape. Alumina shows small but significant uptake of PTA but the PZC of alumina is higher than that of PdO (as chapter 3, the PZC of $PdO \cdot H_2O$ is 4), therefore PTA can has increased electrostatic interaction with the PdO surface compared to alumina.

a)

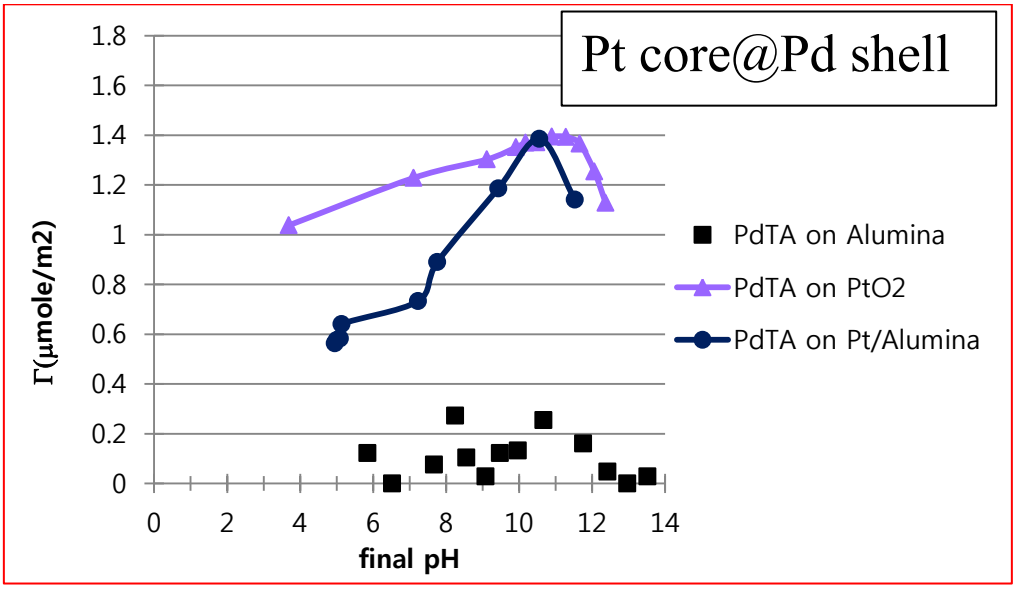

b)

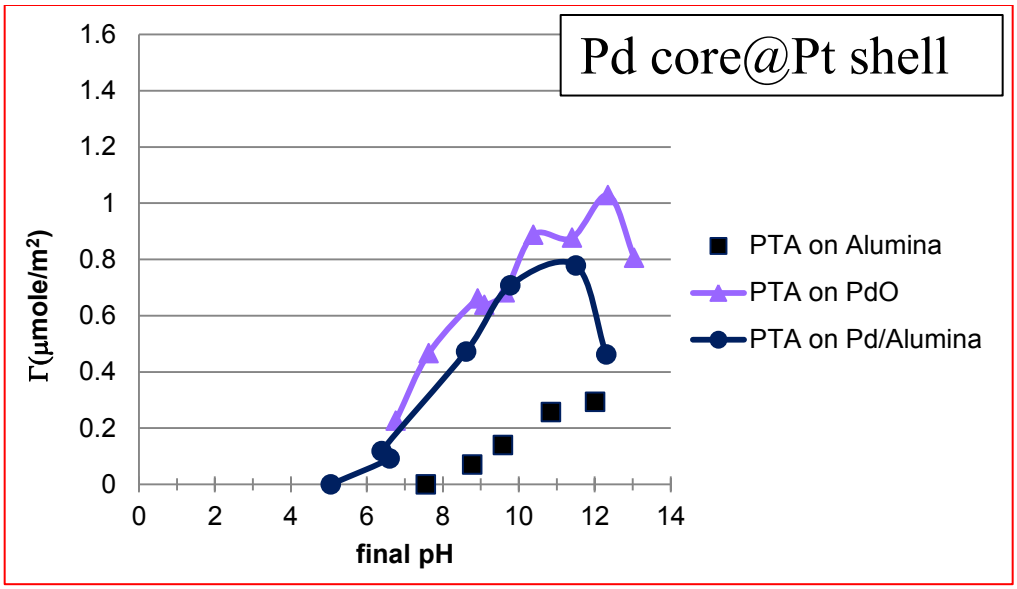

c)

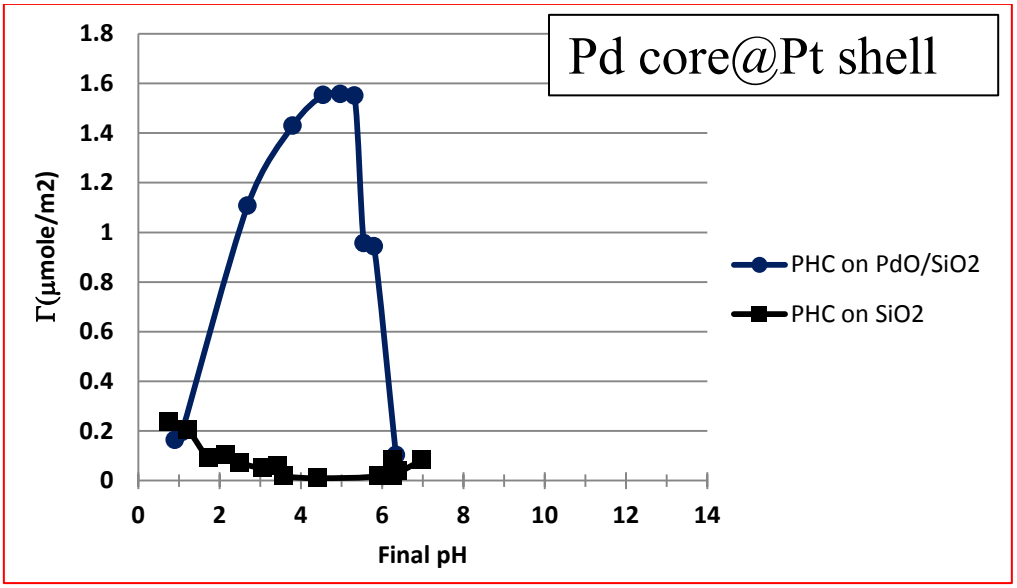

Figure 4.9 Uptake graph a) PdTA b) PTA c) PHC

Figure 4.9c shows an ideal uptake volcano chart of PHC over PdO/silica catalyst but no adsorption over silica, suggesting that the Pt anion precursor should be selectively adsorbed onto the PdO surface of a Pd/SiO_2 catalyst. Curiously, the adsorption trend of the PHC suggests that the PZC of the PdO is 7, which was the PZC measured for unhydrated PdO; however for commercially available $PdO \cdot H_2O$, the value has been measured as 4.0 and that value was consistent with adsorption trend of cations onto PdO

in chapter 3.

From the adsorption surveys of figure 4.9, the optimal pHs for selective adsorption of the shell metal onto the core metal were determined to be 5.0 for PHC adsorption onto PdO/silica, 9.8 for PTA on PdO/alumina, and 10.6 for PdTA on PtO_2/alumina. Three cycles of seq-SEA were used to increase the loading of the shell metal; the weight loadings of these catalysts are summarized in table 4.4.

Table 4.4 Metal wt% of PT/Pd core shell catalysts

Support	**Type**	**Pt wt%**	**Pd wt%**
Silica	1st seq-SEA	0.44	4
	2ND seq-SEA	0.8	
	3RD seq-SEA	1.0	
Alumina	1st seq-SEA	6	0.55
	2nd seq-SEA		1.0
	3rd seq-SEA		1.28
	1st seq-SEA	0.1	2
	2nd seq-SEA	0.21	
	3rd seq-SEA	0.33	

B. XRD

Powder XRD patterns of the core/shell catalysts are compared to DI-prepared catalysts of the same nominal composition in Figure 4.10. The Pd@Pt (Pt shells on Pd cores) on silica patterns are shown in Figure 4.10a. Particles produced by seq-SEA are a

single fcc phase and the size has not changed after repeating SEA 3 times; the average size was determined to be 2.0 nm. In contrast to seq-SEA, particles by co-DI are larger and the crystal patterns reveal a mixture of various phases; PtO_2, PdO and Pt/Pd alloy.

XRD patterns of the Pt@Pd alumina supported catalysts in figure 4.10b are similar to the set of silica catalysts. The 3rd seq-SEA particle size increased to 3.0 nm, compared with 1.5nm for the 1st seq-SEA, but only one fcc phase is found. The co-DI catalyst, which has the same wt% with the 3rd seq-SEA contains agglomerated alloyed particles and Pt oxide. The particle size of the co-DI catalyst is again somewhat small due to the CEDI effect, similar to the co-DI catalysts shown in figure 4.5c.

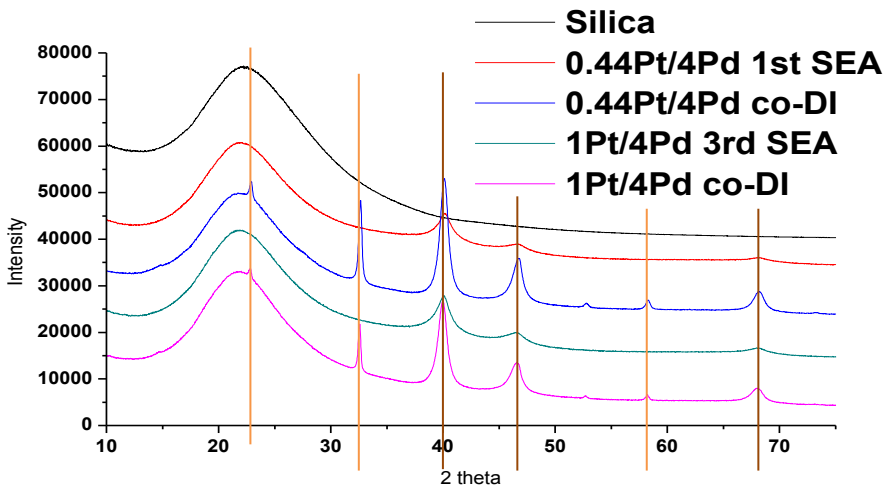

a)

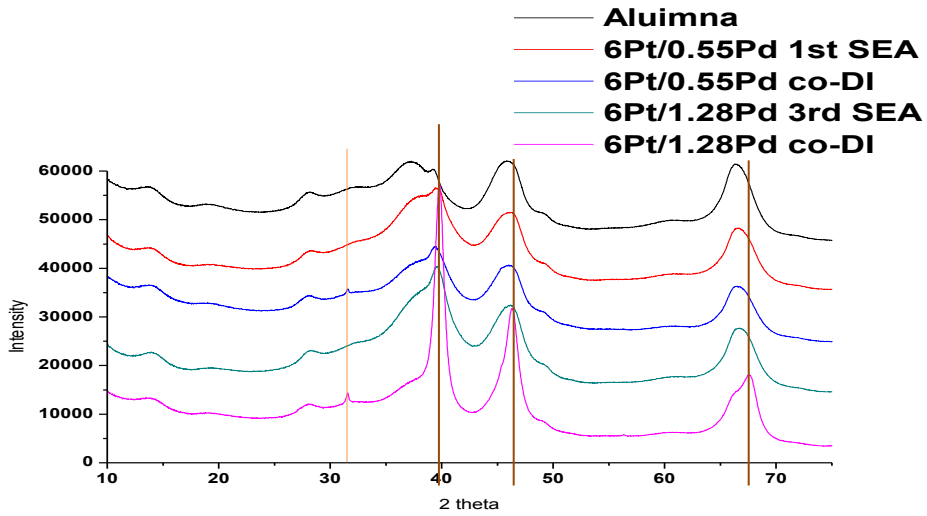

b)

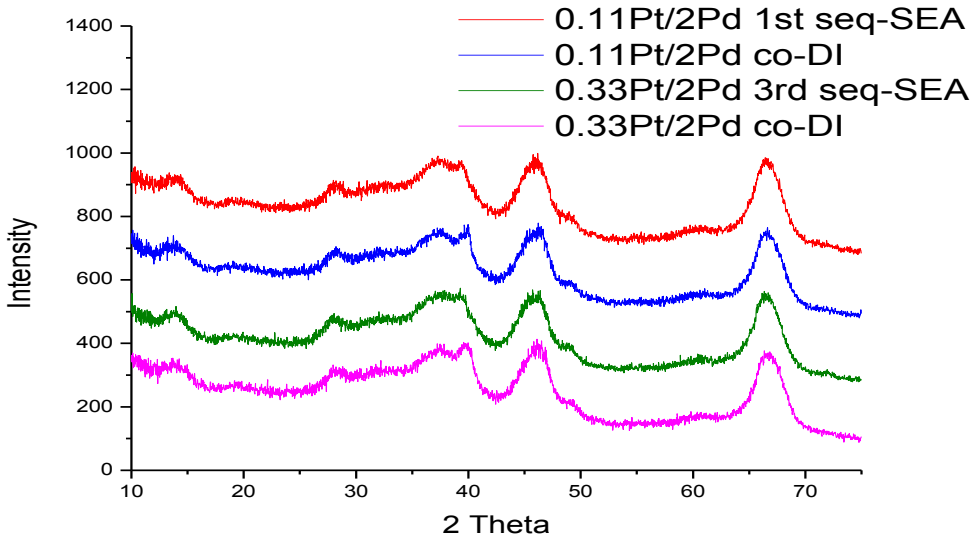

c)

Figure 4.10 XRD patterns of seq-SEA vs co-DI a) Pd@Pt/SiO_2 b) Pt@Pd/A c) Pd@Pt/A

Figure 4.10c shows XRD patterns of the Pd@Pt alumina catalysts. No obvious crystal peaks are detected on the seq-SEA samples, implying that average particle sizes are less than 2nm. There is a peak near 40^o of the co-DI samples, attributable to either Pd or Pt(111) or a Pt-Pd alloy. There is insufficient signal to definitely identify the peak.

C. STEM and EDXS

STEM and EDXS analysis of the core/shell catalysts and corresponding co-DI catalysts of the same composition is given in figure 4.11. The Pd@Pt/silica samples are shown in figure 4.11a. High resolution z-contrast images reveal an uneven, relatively unstructured layer of Pt atoms (brighter spots) around structured Pd cores. EDXS maps support a Pd core@Pt shell structure, as the Pt maps of individual particles are wider than the corresponding Pd maps. The particles of 1Pt/4Pd/silica by co-DI in figure 4.11b are large, agglomerated and some parts are Pd rich while others are Pt rich, consistent with XRD showing a mixture of phases (figure 4.10a).

Images and maps of the 1.28Pd/6Pt/alumina catalyst synthesized by seq-SEA are shown in figure 4.11c. EDXS maps appear to confirm the existence of partial Pd shells on the Pt cores. The average particle size is near 3 nm, the same as XRD analysis (figure 4.10b). The 1.28Pd/6Pt/alumina by co-DI could not be analyzed by EDXS because high numbers of Pt atoms are easily charged by x-ray beams and moved during analysis. The Pt particles of seq-SEA catalyst are partially covered by Pd atoms and those particles may be more stable under the beam. Average particle size of co-DI on alumina (figure 4.11d) is small (less than 2nm) because most of the particles are very small, this may be attributed to the CEDI effect, but agglomerated large particle still exist, creating to a bimodal particle size distribution.

STEM analysis of the 0.33Pt/2Pd/alumina core/shell catalyst by seq-SEA (figure 4.11e) gave an average particle size of 2 nm, similar to co-DI (figure 4.11f). High resolution z-contrast images reveal the presence of Pt atoms on the Pd surface, similar to figure 4.11a. EDXS maps also suggest the decoration of Pd cores with Pt atoms. The

EDXS map of the co-DI particle also suggests the co-location of Pt and Pd, however presence of Pt on the particle surfaces is not as evident in the the high resolution image.

Catalyst	STEM image	Mapping of Pt & Pd
a) 1Pt/4Pd/ silica by seq-SEA	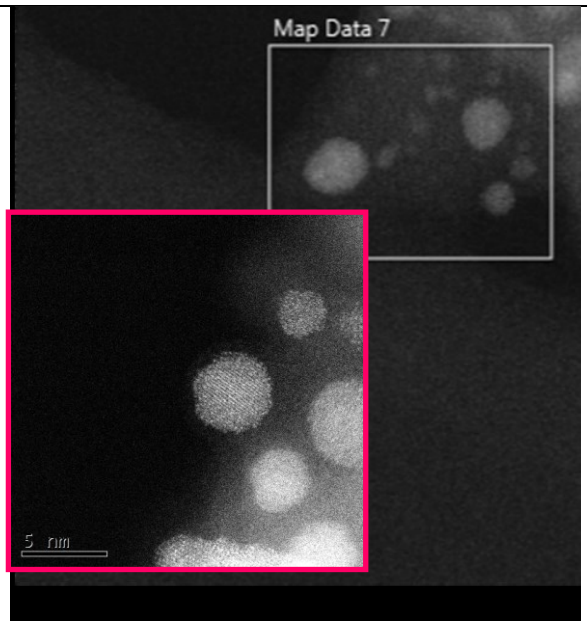	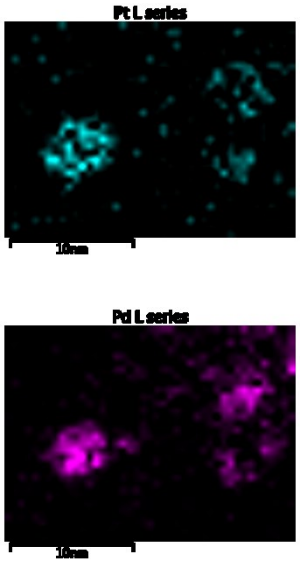
b) 1Pt/4Pd/ silica by co-DI		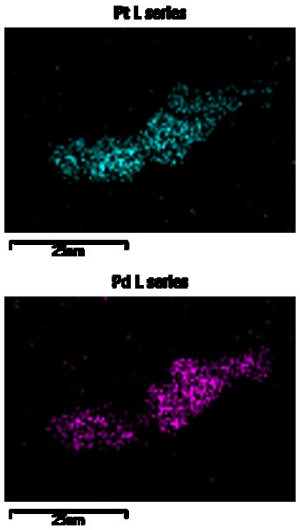

c) 1.28Pd/6Pt /alumina by seq-SEA	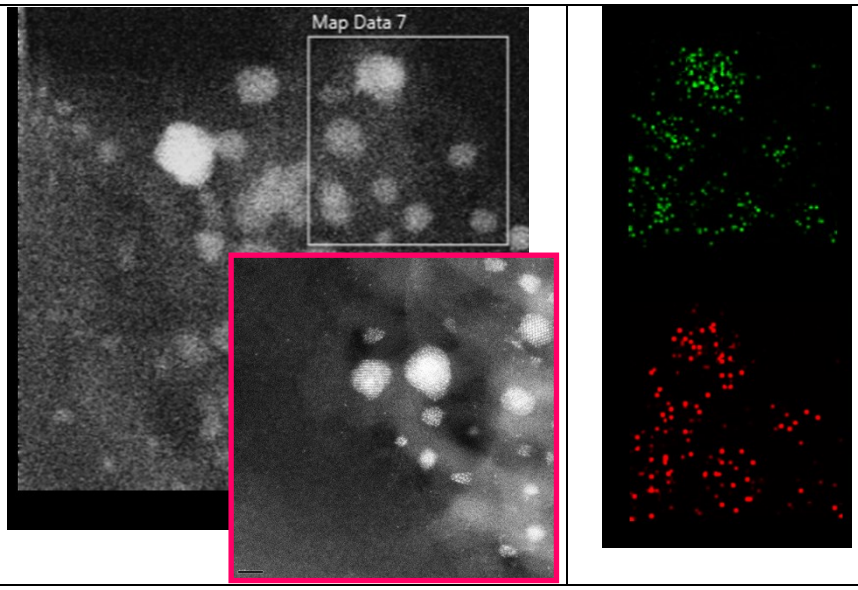
d) 1.28Pd/6Pt /alumina by co-DI	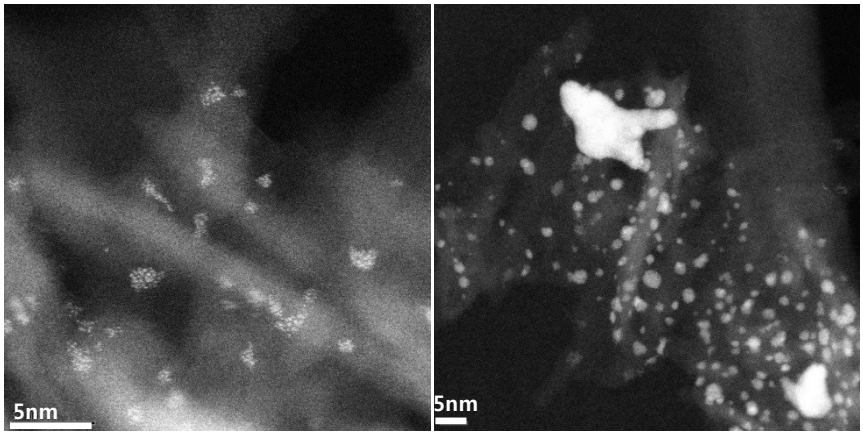

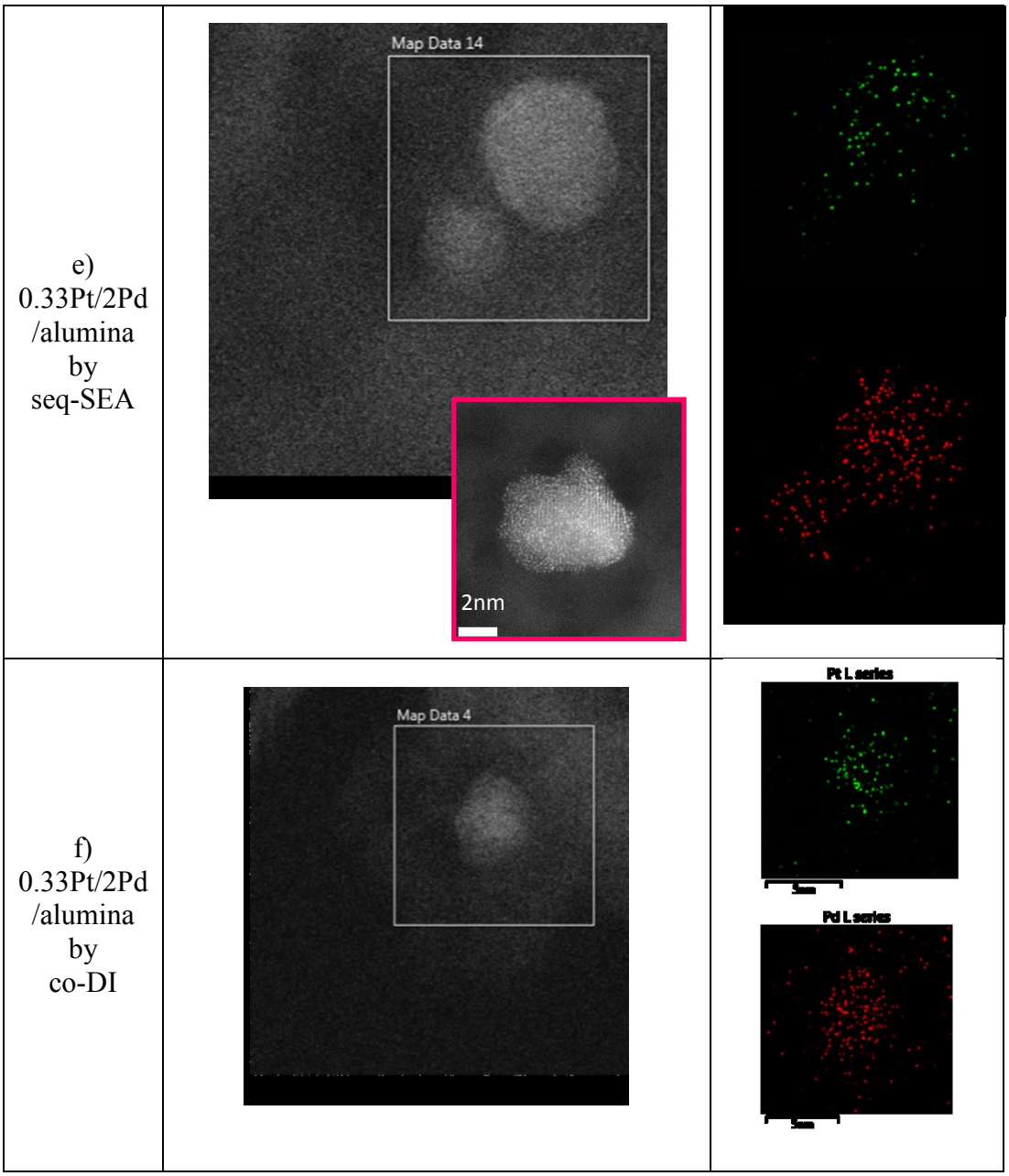

Figure 4.11 STEM and EDXS of seq-SEA vs co-DI a) 1Pt/4Pd/silica by seq-SEA and b) by co-DI, c) 1.28Pd/6Pt/alumina by seq-SEA and d) by co-DI, e) 0.33Pt/2Pd/alumina by seq-SEA and f) by co-DI.

D. Catalytic Activity : Oxidation of Diesel Exhaust

USC's collaboration with Johnson Matthey will involve the future evaluation of a number of the co-SEA, seq-SEA, and co-DI Pt/Pd catalysts synthesized to date. A preliminary look at JM's evaluation has been obtained by their testing of two catalysts;

the 1wt%Pt/4Pd/SiO_2 Pd@Pt core/shell catalyst synthesized by three SEA cycles, and the co-DI catalyst with identical metal loadings. The light-off curves for CO, total hydrocarbons (THCs), and NO conversion for these two catalysts are shown in figure 4.12 as a function of aging conditions.

a)

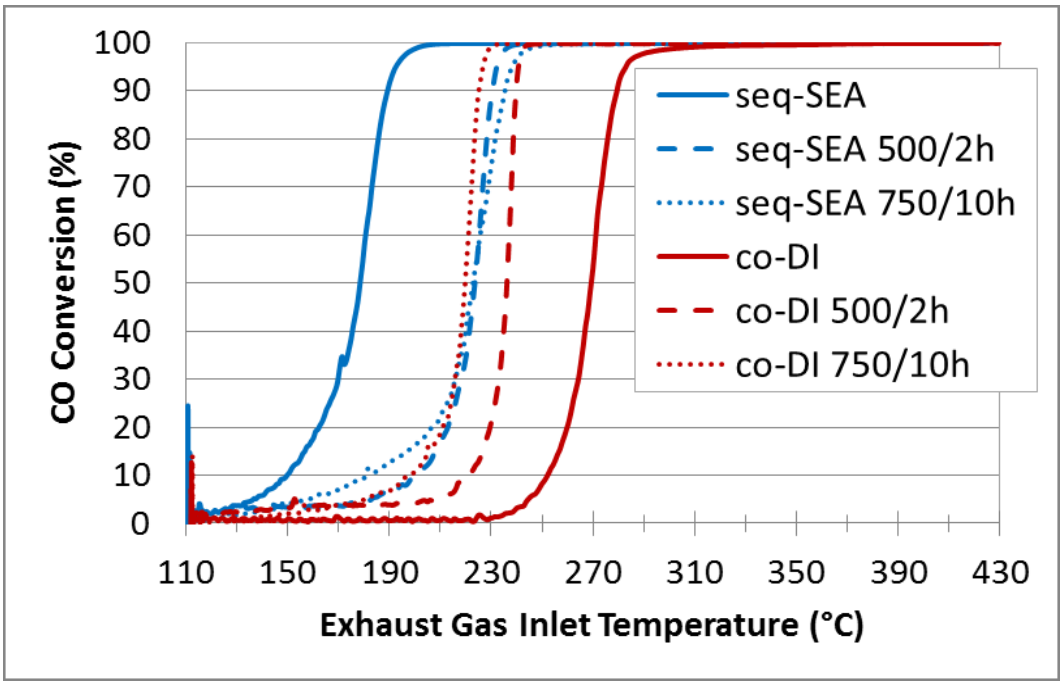

b)

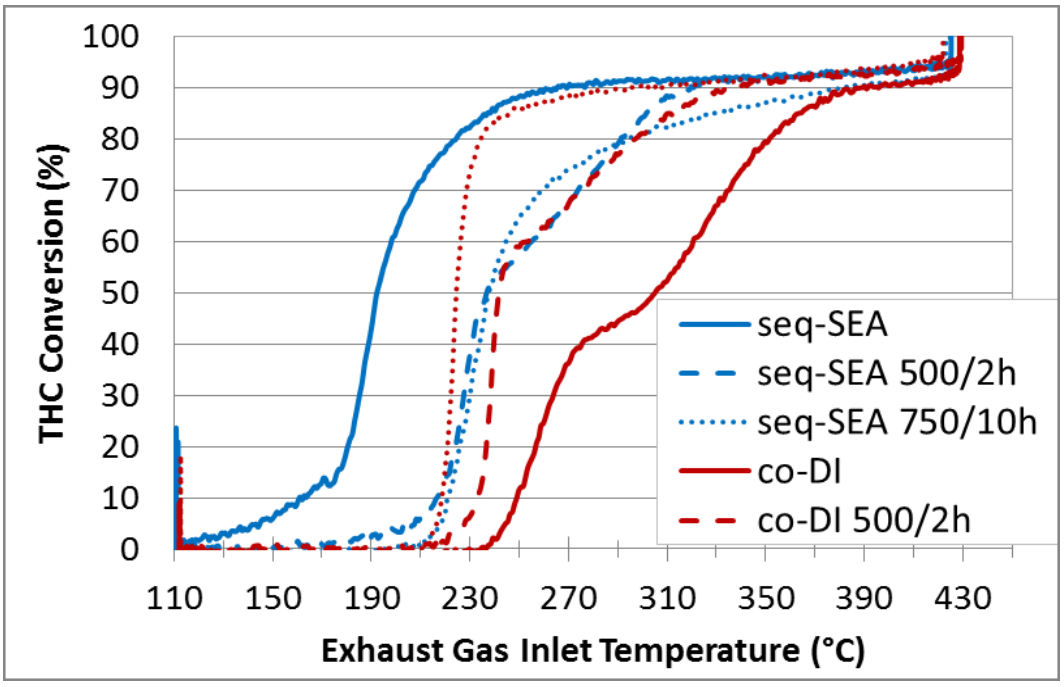

c)

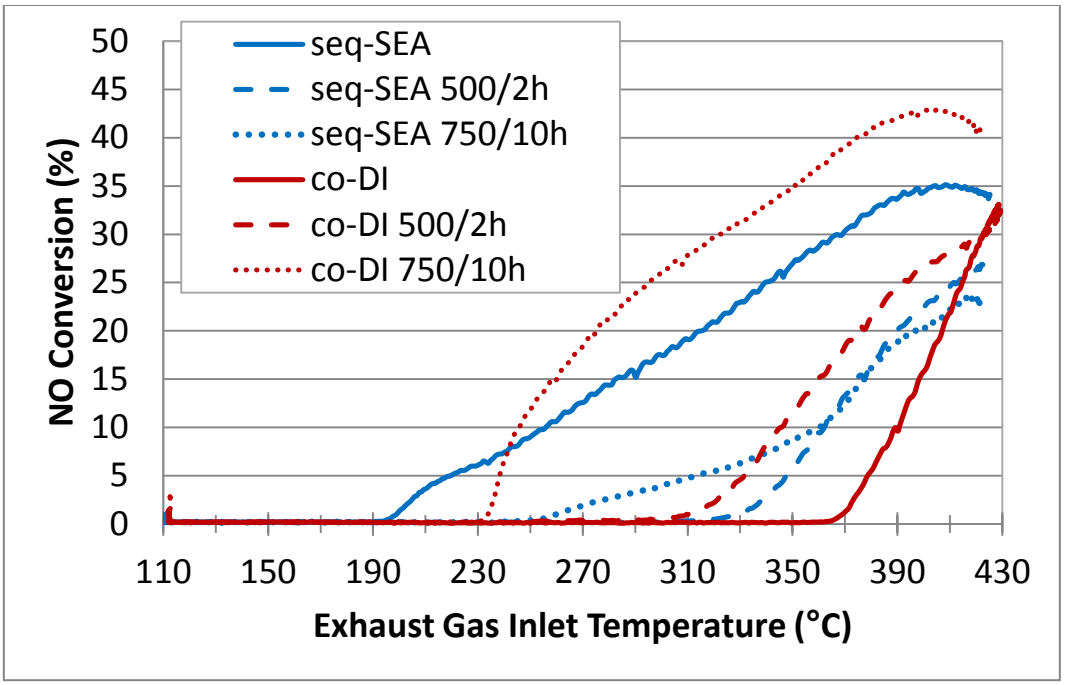

Figure 4.12 Catalytic Activity for DOC a) CO b) THC and c) NO.

Figure 4.12a shows that the activity of the fresh seq-SEA catalyst was much higher than that for the co-DI catalyst, having a light-off temperature of 179°C compared to 267°C for the co-DI catalyst. After aging at 500°C for 2hrs, however, the light-off curve of the seq-SEA catalyst moves to higher temperature, and the co-DI moves down to lower temperatures. After aging at 750°C for 10hrs, the CO light-off curves virtually overlap. It is clear that silica does not anchor the nanoparticles at even the milder calcination temperature and the higher temperature treatments are sufficient to achieve equilibrium particle size and composition. (Post reaction samples will be returned to USC for future characterization.) Alumina supported catalysts may exhibit better stability.

Trends in the THC light-off temperature, seen in figure 4.12b, are similar. The THC light-off temperature of seq-SEA is initially 192°C, whereas co-DI is 302°C. But after thermal treatments, the THC light-off temperature of the seq-SEA sample increases and that of the co-DI sample decreases, such that after the 750°C, 10 h treatment the co-DI

light-off temperature is actually lower than the seq-SEA sample. The same trends are also seen in NO conversion, which is not expected to be high as the feed stream contains a great excess of oxygen. The light-off curve for the co-DI, 500°C 2 h treatment appears to be spurious.

It cannot presently be ascertained to what extent the large difference in initial activity is due to metal dispersion on the one hand, or intimate Pt-Pd contact on the other. A comparison of the seq-SEA sample with a control catalyst featuring a physical mixture of two SEA-prepared, well dispersed single metal catalysts, with nearly identical overall metal active area, will enable this effect to be isolated. The deactivation of the seq-SEA catalyst may primarily be sintering, and the activation of the co-DI catalyst may be wetting. Post-reaction characterization by XRD and STEM will help answer these questions.

The entire set of catalysts synthesized for evaluation at JM is listed in table 4.5. Samples number 5 and 6 were those already tested. Only oxide supports have been used as carbon would be unstable in this reaction. Silica supported bimetallic catalysts have been prepared with co-SEA for homogeneous alloys, and by seq-SEA with Pt shells on Pd cores, with 1 and 3 SEA cycles of Pt shell application. As controls, co-DI samples at the same nominal compositions have been prepared, and a physical mixture of SEA-prepared single metals with high single metal dispersion will be used to eliminate the difference in metal dispersion and isolate the effect of intimate Pd-Pt contact in the co-SEA and seq-SEA samples. For alumina, the same variety of sample is prepared, with either Pt shells and Pd cores, or Pd shells and Pt cores.

Table 4.5 The list of catalysts that are being evaluated at JMTC for DOC evaluation.

	Catalyst	Pt wt%	Pd wt%	Type	Method
1	0.44 Pt/ 4.0 Pd by seq-SEA	0.44	4	Pd@Pt	1st seq-SEA
2	0.44 Pt/ 4.0 Pd by co-DI	0.44	4	Alloy	co-DI
3	0.44 Pt/ 4.0 Pd by PM-SEA	0.44	4	Pd + Pt	PM(SEA+ SEA)
4	0.56 Pt/ 3.2 Pd by co-SEA	0.56	3.2	Alloy	co-SEA
5	1.0 Pt/ 4.0 Pd by seq-SEA	1	4	Pd@Pt	3rd seq-SEA
6	1.0 Pt/ 4.0 Pd by co-DI	1	4	Alloy	co-DI
7	1.0 Pt/ 4.0 Pd by PM-SEA	1	4	Pd + Pt	PM(SEA+ SEA)
8	4.5 Pt/ 2.0 Pd by co-SEA	4.5	2	Alloy	co-SEA
9	4.5 Pt/ 2.0 Pd by co-DI	4.5	2	Alloy	co-DI
10	4.5 Pt/ 2.0 Pd by PM-SEA	4.5	2	Pd + Pt	PM(SEA+ SEA)
11	0.55 Pd/ 6.0 Pt by seq-SEA	6	0.55	Pt@Pd	1st seq-SEA
12	0.55 Pd/ 6.0 Pt by co-DI	6	0.55	Alloy	co-DI
13	0.55 Pd/ 6.0 Pt by PM-SEA	6	0.55	Pd + Pt	PM(SEA+ SEA)
14	1.28 Pd/ 6.0 Pt by seq-SEA	6	1.28	Pt@Pd	3rd seq-SEA
15	1.28 Pd/ 6.0 Pt by co-DI	6	1.28	Alloy	co-DI
16	1.28 Pd/ 6.0 Pt by PM-SEA	6	1.28	Pd + Pt	PM(SEA+ SEA)
17	1.58 Pd/ 5.3 Pt by co-SEA	5.3	1.58	Alloy	co-SEA
18	0.11 Pt/ 2.0 Pd by seq-SEA	0.11	2.0	Pd@Pt	1st seq-SEA
19	0.11 Pt/ 2.0 Pd by co-DI	0.11	2.0	Alloy	co-DI
20	0.11 Pt/ 2.0 Pd by PM-SEA	0.11	2.0	Pd + Pt	PM(SEA+ SEA)
21	0.33 Pt/ 2.0 Pd by seq-SEA	0.33	2.0	Pd@Pt	3rd seq-SEA
22	0.33 Pt/ 2.0 Pd by co-DI	0.33	2.0	Alloy	co-DI
23	0.33 Pt/ 2.0 Pd by PM-SEA	0.33	2.0	Pd + Pt	PM(SEA+ SEA)

4.3 CONCLUSIONS

Three preparations of bimetallic catalysts, co-SEA, seq-SEA and co-DI, were demonstrated with Pd and Pt precursors on silica, alumina, and carbon support. co-SEA yields well dispersed homogeneous Pt-Pd alloy particles, while co-DI gives large, agglomerated, inhomogeneous particles, which can be improved somewhat if the

precursor solution is highly acidic or basic to produce the CEDI effect. With seq-SEA, core@shell structures can be prepared by selectively adsorbing a second metal onto a first metal oxide. Shell metal loading can be increased by additional cycles of SEA, which gives some flexibility at catalyst composition in exchange for more synthesis steps.

An initial assessment of catalytic activity for diesel exhaust oxidation showed much higher initial activity of seq-SEA catalysts than for co-DI catalysts, but the highly dispersed SEA-derived materials appeared to sinter quickly on the silica support. Future studies with other supports and other core/shell and homogeneously alloyed morphologies will enable a better correlation of rational synthesis to structure and function.

CHAPTER 5

CARBON SUPPORTED Au-Pd BIMETALLIC CATALYSTS FOR BENZYL ALCOHOL OXIDATION

Combinations of noble metals such as Au and Pd in bimetallic catalysts have important applications such as the selective oxidation of alcohols, the carbonyl products of which serve as important and versatile intermediates for the synthesis of fine chemicals [68]. There are many studies of aerobic catalytic oxidation for the formation of alcohols into carbonyl compound utilizing one or both of these metals [68-76]. Until very recently, most of the attention for oxidation of alcohols to carbonyl compounds focused on supported Pd catalys [68,70,77,78]. Gold has also been shown to be an effective catalyst for the selective oxidation of alkenes and alcohols [71,79]. Gold promoted bimetallic catalysts have significant influence on selectivity. Chen and co-workers reported that the role of Au is to isolate single Pd sites that facilitate the coupling of critical surface species to product, while inhibiting the formation of undesirable reaction by-product [80]. A combination of Pd with Au promotes both the activity and selectivity for the benzyl alcohol oxidation [81-83]. Au-Pd bimetallic catalyst supported by activated carbon not only improved catalytic activity and selectivity to the benzaldehyde, but also enhanced the resistance to poisoning [83].

In spite of the intricate interactions believed necessary of the two metals, the synthesis of Au/Pd nanoparticles is far from optimized. Supported Au-Pd catalysts are most often prepared by co-impregnation (referred to here as co-dry impregnation or co-

DI) and precipitation [72,82,84-91] In co-DI, both metals are added to the amount of solution just necessary to fill the pore volume of the support. Precipitation is effected by adding base (NaOH) to adjust pH to 9 in a slurry of the two acidic precursors and support. These preparation methods make no or relatively little provision for 1) high metal dispersion which imparts high activity per mass of metal or 2) metal-metal interactions, which produce high selectivity. More precise control of size and composition of Au-Pd nanoparticles can be achieved by colloidal techniques [69,72,73,83,84], but this methodology is relatively complex, leads to problems of removing the organic scaffold, and is difficult to scale [92].

In this chapter we demonstrate a simple, rational, repeatable, scalable seq-SEA to synthesize Au-Pd bimetallic nanoparticles of very high dispersion and with more intimate interactions between the two metals. seq-SEA steps for supported bimetallic Au-Pd nanoparticle synthesis is illustrated in figure 5.1. First, Pd anionic precursor adsorbed on protonated carbon surface by SEA and after reduced and calcined, well dispersed PdO particles are over carbon surface. At optimal pH, PdO surface is negatively charged when the carbon surface is positively charged because of the PZC differences between PdO and carbon. The surrounding protonated carbon support gives the ability to selectively adsorb gold cations onto the deprotonated PdO particles, and not on the carbon.

In this way we have improved the benzyl alcohol oxidation activity of a 2.5wt%Au/2.5wt%Pd/carbon (referred to hereafter as 2.5Au/2.5Pd/C) catalyst prepared by co-DI by a factor of ten, using 25 times less Au.

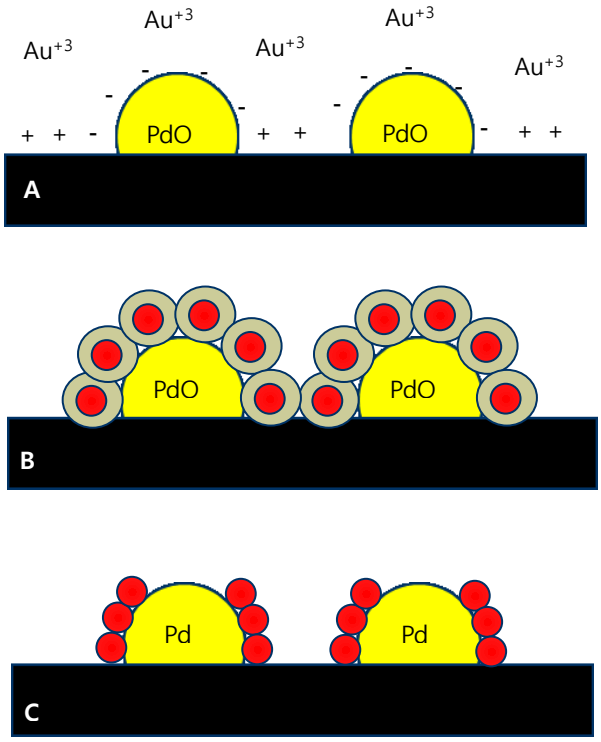

Figure 5.1 Schematic of seq-SEA. (A) At optimal pH, the core metal oxide (PdO) is negatively charged and support carbon is positively charged. (B) Au cation precursor is adsorbed on the negatively charged PdO surface with a hydration sheath. (C) After reduction with H_2, Au is reduced as a partial shell over reduced Pd core.

5.1 EXPERIMENTS

5.1.1 Materials

The carbon support was Darco G-60 (C, surface area: 738m^2/g, PZC: 8). Palladium tetrachloride (PdTC, $[PdCl_4]^{-2}$) and Gold biethylenediamine (AuBen; $[Au(en)_2]^{+3}$) were used as metal precursors. Also, pure palladium oxide was purchased from Fluka, Inc.

5.1.2 Catalysts Preparation

2.5Pd/C was synthesized first by SEA to prepare nanoparticles of the core Pd. After reduction, the ultrasmall Pd particles oxidized upon exposure to air. Two loadings of gold (0.1 and 0.5Au) were applied to the PdO nanoparticles by a second SEA application which we term sequential SEA (seq-SEA). At high pH, the high PZC carbon will adsorb

less cations than PdO which has the lower PZC as chapter 3, so that in principle, gold cations of AuBen can be selectively adsorbed onto the PdO nanoparticles. Core-shell Pd@Au morphologies will result after the Au precursors on the Pd oxide nanoparticles are reduced. For comparison with past literature reports, another catalyst with the commonly employed loadings of 2.5Au and 2.5Pd [85,86,88-91] was prepared by co-DI. Others at 0.1 and 0.5Au were prepared by DI of the gold onto the well dispersed, SEA-prepared 2.5Pd/C. All catalysts were reduced at 150 °C as determined by temperature programmed reduction.

5.1.3 Catalysts Characterization

A. XRD

Powder XRD measurements were made using a Rigaku MiniFlexII bench-top system. XRD patterns were compared to reference spectra using PDXL (Rigaku Corporation) software. The radiation source was Cu Kα radiation (λ = 1.5406 Å) at operating condition of 30kV and 15mA. All spectra were taken at a scan rate of 0.5^{o}/min and sampling width of 0.02^{o}.

B. CO chemisorptions

10% Carbon monoxide (balanced He) chemisorptions was used to determine the accessible Pt surface (Micromeritics ASAP 2920) at 40°C. The samples were first dried at 150 °C in a He flow for 1 h and subsequently reduced in a H_2 flow at 150 °C for 1 h (ramp = 10°C/min).

C. STEM and EDXS

The microscope used in this study was a TITAN 80-300 with ChemiSTEM Technology (FEI Company; Hillsboro, USA). It was equipped with a CEOS GmbH

(Heidelberg, Germany) CESCOR spherical aberration probe corrector capable of generating a sub-Ångstrom electron probe (0.8 Å) at an accelerating voltage of 200 keV. The ChemiSTEM system comprises a design that includes a high-brightness emission source (X-FEG Schottky) for enhanced beam current, and the integration of four, windowless(30 mm^2) FEI-designed silicon drift detector(s) (SDD) into the objective lens for a total collection area and solid angle of 120 mm^2 and 0.7 sr, respectively, for enhanced detectability.

Particle chemistry was determined by using centering the probe on individual particles and collecting the X-rays for a period no longer than 30 sec. For larger crystallites areal scans were collected to encompass the signals generated by the entire particle. Chemical maps were collected over selected regions of interest comprised of multiple particles. Collection times varied between 10 – 20 minutes with a dwell time set at 8 μs/pixel and cut off energy slit of 20 keV.

Prior to STEM imaging each sample was reduced under hydrogen flow at 150 ^oC for 1 hour and then exposed to air for 48 hours to ensure a skin of PdO would form over a metallic Pd core and removal of any residual ligands. The bimetallic Au-Pd catalysts were reduced at 100^oC for 1 hour at a ramp rate of 0.5^oC/min.

D. Reactivity Test (Benzyl Alcohol Oxidation)

Dr. Hutching's group (Cardiff University, UK) tested all the catalysts for benzyl alcohol oxidation with a 100ml scale batch reactor(Autoclave Engineers Inline MagneDrive lll). The vessel was charged with benzyl alcohol 40ml and 25mg of catalysts. The pressure was maintained 10bar of O_2, the temperature was 140°C via a sampling pipe, ensuring that the volume purged before sampling was higher than the tube volume, and

the analyzed by GC using a DB-Wax column.

5.2 RESULT AND DISCUSSION

5.2.1 Uptake Survey and Selective Adsorption

In figure 5.2a, the uptake curve exhibits the volcano shape expected of electrostatic adsorption [20], with uptake increasing as pH is lowered from the carbon's PZC, (8.5),

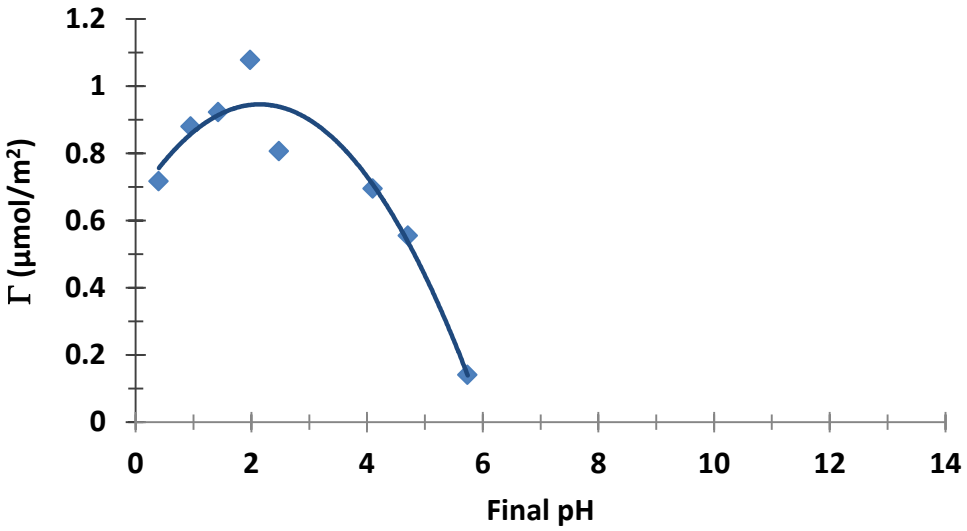

a)

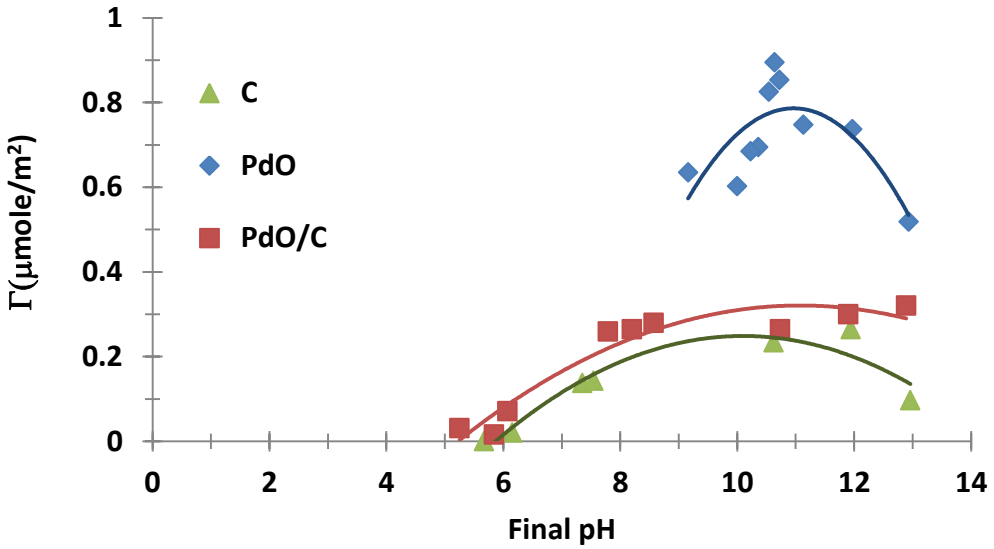

b)

Figure 5.2 Metal uptake surveys, a) PdTC on Darko G60 carbon, b) AuBen on ca rbon, PdO, and PdO/carbon
but then decreasing at the lowest pH range as ionic strength increases.

The pH of the strongest electrostatic interaction occurs at a pH of 2.0, (initial pH 2.0) at which condition a large quantity of catalyst was synthesized by simply scaling up the volume. The uptakes of across pH range of 2-13 were measured over the G60 carbon support, over pure PdO, and over PdO/G-60 (figure 5.2b). The uptake of the Au cation onto carbon is relatively low. This data is consistent with earlier data for Pt cation uptake on high PZC carbon [20]; the high PZC carbon materials do not possess the functional groups which accrue a significant negative charge at high pH and so do not strongly adsorb cations. We have measured the PZC of PdO to be 4 in chapter 3, and the uptake of the AuBen cation onto it exhibits a high pH volcano with a maximum at a pH of about 10.5. The fraction of the PdO in the PdO/carbon material is small such that the increased Au uptake on the PdO/carbon is small, except at pH 13, where it appears the adsorption of Au is most selective. Consequently, this pH 10.5 was used for the subsequent synthesis of larger amounts of catalyst.

5.2.2 Catalysts Characterization

A. XRD

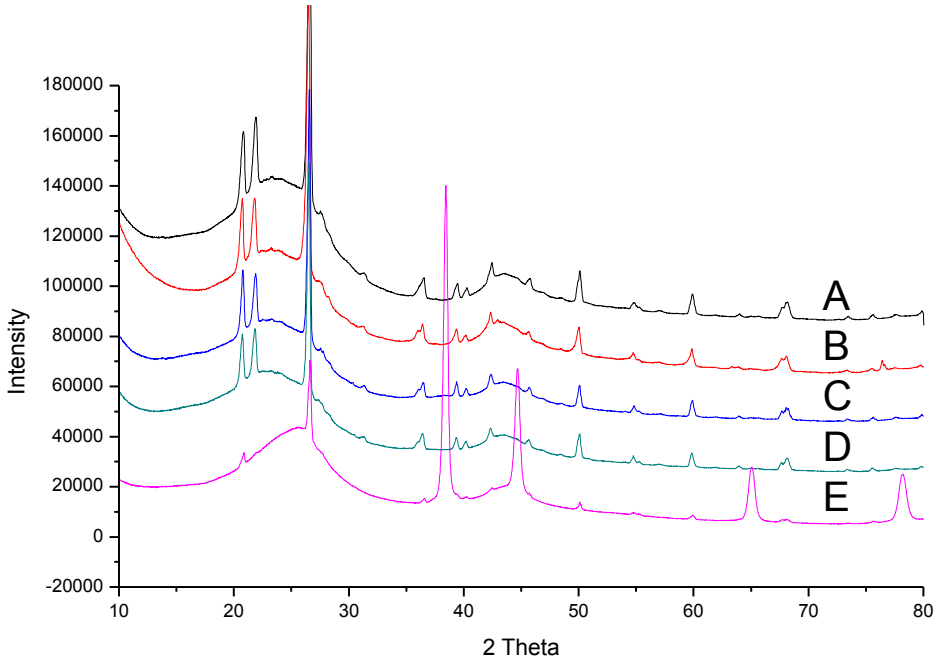

Figure 5.3 X-ray Diffraction patterns of (**A**) Carbon support, (**B**) 2.5Pd/C by SEA, (**C**) 0.5Au/2.5Pd/C and (**D**) 0.1Au/2.5Pd/C by seq-SEA (**E**) 2.5Au/2.5Pd/C by co-DI.

An initial measure of the synthesis effectiveness was provided by powder XRD, the results of which are given in figure 5.4. The pure carbon black support exhibits characteristic graphitic peaks. In no XRD pattern of the SEA prepared samples, including the Au-free, 2.5Pd/C and the 0.1 and 0.5Au on 2.5Pd/C, were any crystalline peaks for the metals observed. The limit of detection of this XRD instrument which features a newest-generation, high sensitivity silicon slit detector is close to 1 nm. In contrast, for the 2.5Au/2.5Pd/C co-DI sample sharp peaks of fcc Au were seen. The particle size of this Au or Au-rich phase calculated from the Scherrer equations is about 220 Å. No separate Pd-rich phase was detected by XRD for the co-DI preparation.

B. STEM and EDXS

A much more refined characterization of particle size and individual nanoparticle

composition was achieved by STEM. From *Z*-contrast images of the 2.5Pd/C material (representative image in figure 5.4a), the average particle size is 7.7 Å.

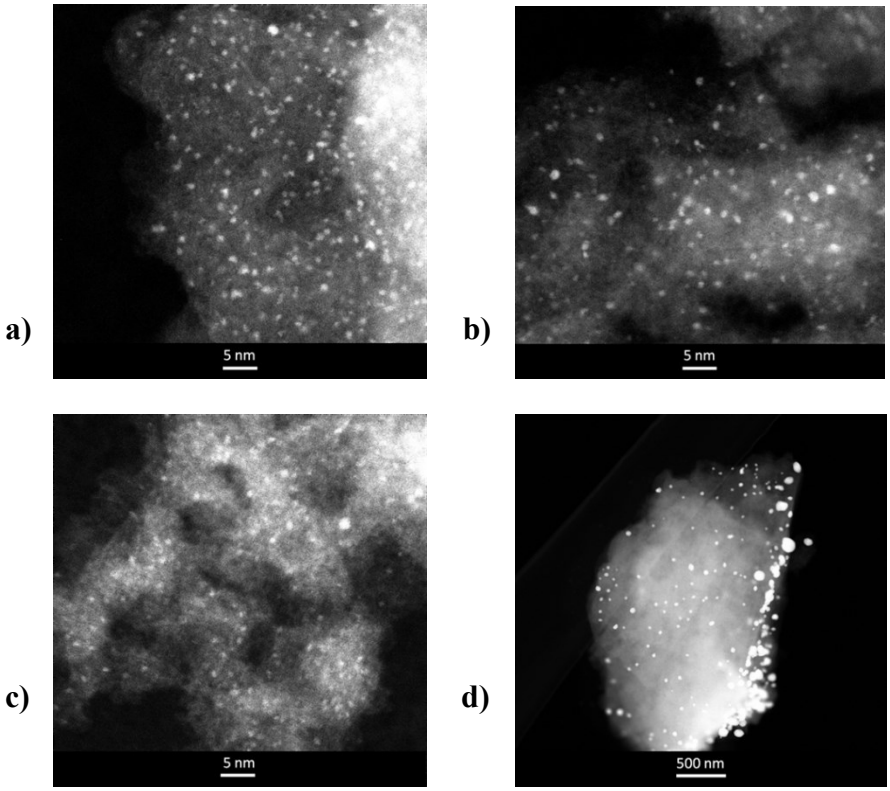

Figure 5.4 STEM images of **a)** 2.5Pd/C by SEA, b) 0.1Au/2.5Pd/C and c) 0.5Au/2.5Pd/C by seq-SEA, and d) 2.5Au/2.5Pd/C by co-DI.

Analysis of the 0.1 and 0.5Au on Pd/C by seq-SEA (representative images in figure 5.4b and c), showed that the average particles size increased slightly to 8.2 and 8.4 Å respectively. These small sizes explain the lack of detection by XRD. Particles are not only uniform in size but are also well-distributed over the carbon support. In contrast, the metal particles prepared by co-DI (figure 5.4d) have much larger size, with much broader size distributions, and are much less homogeneously distributed on the surface than the SEA-prepared samples. The STEM estimate of average particle size is 480Å, about twice

that of the XRD estimate. Differences between the experimental results can be explained by the sampling where STEM is only able to evaluate a small portion of the sample while XRD is a bulk analytical technique. Consequently, number of particles examined with STEM imaging may not be representative of the overall sample, particularly when the sample has heterogeneity

Imaging and high resolution elemental mapping with energy dispersive x-ray (EDX) spectroscopy are shown in figure 5.5. Representative chemical maps of Au on C (5.5b) and Pd on C (5.5c) of the region imaged in figure 5.5a. This sample was prepared by seq-SEA with metal loadings of 0.1Au and 2.5Pd. Comparison of Figure 5.5a with the Pd and C chemical map in figure 5.5c, for example, shows a clear correlation between Pd particles and Pd X-ray signals. Limited co-location of Au with Pd is seen by comparing the chemical maps in figure 5.5b and c. This could be either because the amount of Au on particles is below detection limits (< 2-3 atoms) or because there are no Au adatoms present.

The composition of individual nanoparticles in both the seq-SEA prepared 0.1Au/2.5Pd and 0.5Au/2.5Pd series was determined and plotted as a function of particle size in figure 5.5f. The particle size given in this plot and also in figure 5.5g are classified approximate due to the use of a defocused probe during chemical analysis, limiting resolution to ~1.4 Å. Figure 5.5f reveals a correlation between composition and particle size. While some smaller Pd particles appear to have no detectable Au, larger particles contain proportionately more.

A representative image of the 2.5Au/2.5Pd co-DI-prepared catalyst is shown in figure 5.5d. The high intensity Au core (Z_{Au} = 197) is coated by a low intensity Pd shell

(Z_{Pd} = 106), consistent with other characterization of Au/Pd bimetallic nanoparticles prepared by co-DI [85,87,88,91]. Moiré fringes arise from the small differences in the Au and Pd lattices. Chemical maps and linescans across the particles (Figure 5.5e) also reveal the Pd shell-Au core morphology. Individual particle compositions plotted versus size (Figure 5.5g) reveal the presence of some very small, Au-free Pd particles, but mainly very large Au rich particles with Pd shells.

It is surmised from this analysis that the co-DI sample exhibits mainly a Pd catalytic surface, a large fraction of which is supported on large Au particles. The Pd shell may be thin enough to be electronically effected by the underlying gold. The seq-SEA nanoparticles appear to feature Au moieties on the Pd surface to a much higher degree than the co-DI sample. It might be anticipated that Au atoms or clusters deposited on the Pd surface will have dramatically different effects on catalytic kinetics, than the underlying core of Au present in the DI-prepared samples.

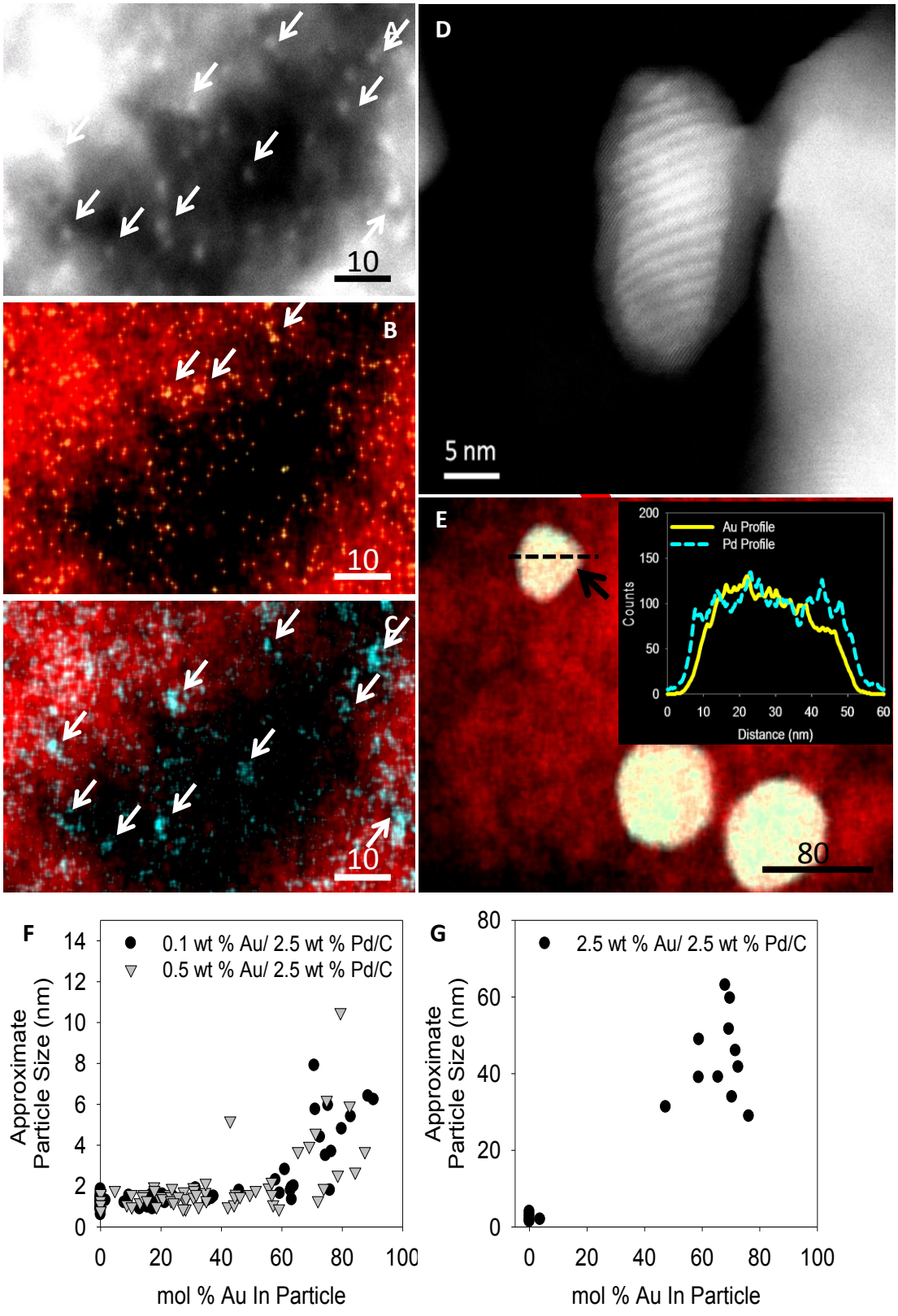

Figure 5.5 (**A** to **C**) Chemical mapping of 0.1Au/2.5Pd/C by seq-SEA. (A) shows STEM image, (B) and (C) indicate carbon to red, yellow to Au and blue to Pd. (**D** and **E**) STEM

image of core-shell particle (D) and chemical mapping and line scanning (E) of 2.5Au/2.5Pd/C by co-DI. (**F** and **G**) The graphs of mole % of Au vs size of particles. (F) shows the particles which are produced by seq-SEA, (G) by co-DI.

C. Particle size analysis

As summarized in Table 5.1, particle size based on STEM analysis agrees with XRD result with every catalyst.

Table 5.1 Particle size analysis

Samples	Number of Particles Examined by STEM	Mean Size by STEM (Å)	Mean size by XRD (Å)	Dispersion (CO Uptake) (%)	Mean Size by CO-Chemi-sorption (Å)
0.1Au-2.5Pd/C	3706	8.2±4.0	< 20	33	30
0.5Au-2.5Pd/C	3354	8.4±3.7	<20	24	42
2.5Pd/C	3629	7.7±2.4	<20	35	29
2.5Au-2.5Pd/C	158	480±470	220	28	36

However, carbon monoxide chemisorption data is not matched with the other analysis data. Based on STEM and XRD, co-DI catalyst should have lower dispersion (2~4%) than actual (28%). The reason cab be explained with Figure 5.5d and e. Although the Au-Pd particle size is large, CO dispersion was better than expected because Pd exists in the form of a thin shell over the Au core. The X-ray diffraction pattern of co-DI (figure 5.3e) can also be explained because the Pd layer may be too thin to be detected, compared with the large size of Au crystals. Core-shell particles may form during calcination of the co-DI catalyst [17]. Pd may be segregated at the particle surface to become PdO during the calcination but Au is easily agglomerated with high temperature.

The Pd-only catalyst also has a same discrepancy with CO chemisorption. The

dispersion should be 100% based on the STEM and XRD analysis but the measured dispersion by CO chemisorption was 35%. Krishnankutty and Vannice suggest that it may be more facile for carbon can migrate onto and into the Pd crystallites during the higher temperature reduction or evaluation periods when Pd is in contact with a clean, highly disordered carbon surface [93]. Their Pd/C catalysts also had lower calculated dispersion by both H_2, O_2 titration and CO chemisorption than the dispersion by STEM since the surface of Pd particles are partially or fully covered by carbon. The chemisorption discrepancy notwithstanding, the trend in uptake by CO is relatively lower after Au is added by seq-SEA because Au partially covers the Pd surface. This suggests that the second metal (Au) adsorbed onto the surface of the first metal (Pd) by SEA, and not on carbon.

D. Benzyl alcohol Oxidation

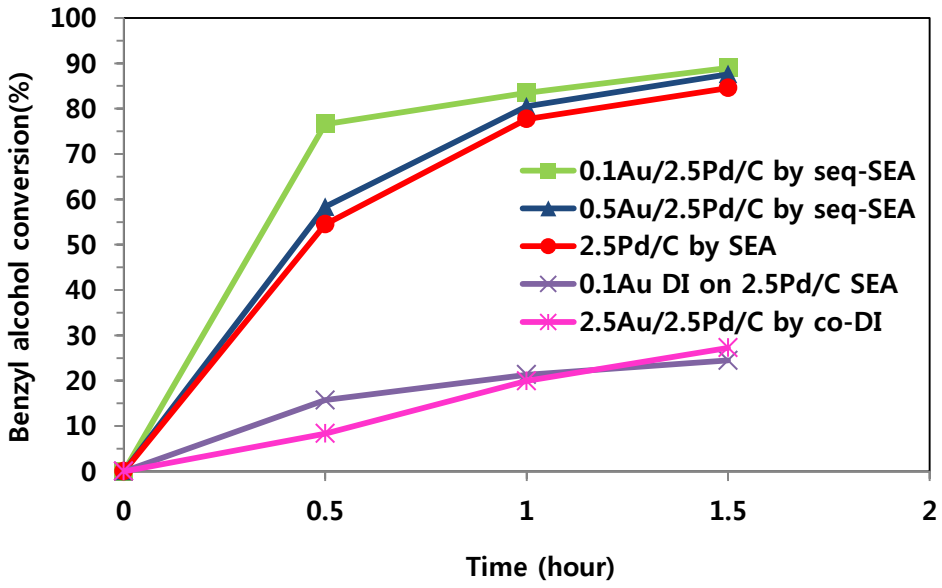

Figure 5.6 Benzyl alcohol conversion (%) with the reaction time at 140°C and 10bar pO_2.

Catalytic activity for benzyl alcohol oxidation is shown in Figure 5.6. As a

benchmark, the catalyst commonly prepared by co-DI with 2.5Au/2.5Pd is seen to have the lowest activity of all samples. The Pd-only SEA-prepared catalyst with 8 Å particles is about 6 times as active as the benchmark; thus a great improvement in activity is brought about simply by dispersing the Pd to a high extent. The seq-SEA prepared 0.1Au/2.5Pd catalyst has at least ten times higher activity (comparing conversions at 0.5 h) than the benchmark, with 25 times less the amount of Au. With the electrostatic deposition of more Au, (0.5Au/2.5Pd) the activity diminished to about the level of the Pd-only catalyst. The lower activity of the higher Au loading can be explained by increasing Au blockage of the Pd surface, whereas the promotion of Pd by the lower Au loading might be explained by an electronic effect in which the surface Au atoms reduce oxygen poisoning over the Pd surface [83]. Geometric effects relating to the balance of adsorption and β-H elimination over terrace and edge/corner sites [82] is less likely as the ultrasmall particles (8 Å, or clusters of about 20 atoms) do not possess an appreciable fraction of terrace sites.

Curiously, when we added 0.1Au by DI to the 2.5Pd catalyst synthesized by SEA, the activity fell far below the Pd-only SEA-prepared catalyst. It was subsequently found by XRD analysis (figure 5.7) that the DI procedure used for adding the Au caused the Pd phase to sinter - peaks of sintered Pd (particle size about 15 nm) were seen in XRD. A further control experiment with a metal-free HCl solution suggested that this is likely due to the acidity of the tetrachloroautate acid DI solution, into which Pd likely redissolved as Pd(II) choride and redeposited without support interaction. The presence of residual chloride could also diminish activity.

The selectivity of the catalysts to various products is given in Table 5.2. As

expected the main product formed is the aldehyde as this is the primary product. However as the reaction time increases for the SEA-prepared catalysts the selectivity to benzoic acid, the sequential oxidation product, is enhanced. This is not observed for the catalyst prepared by impregnation and shows the higher oxidation activity of the smaller nanoparticles produced by this method. Toluene is formed by a transfer

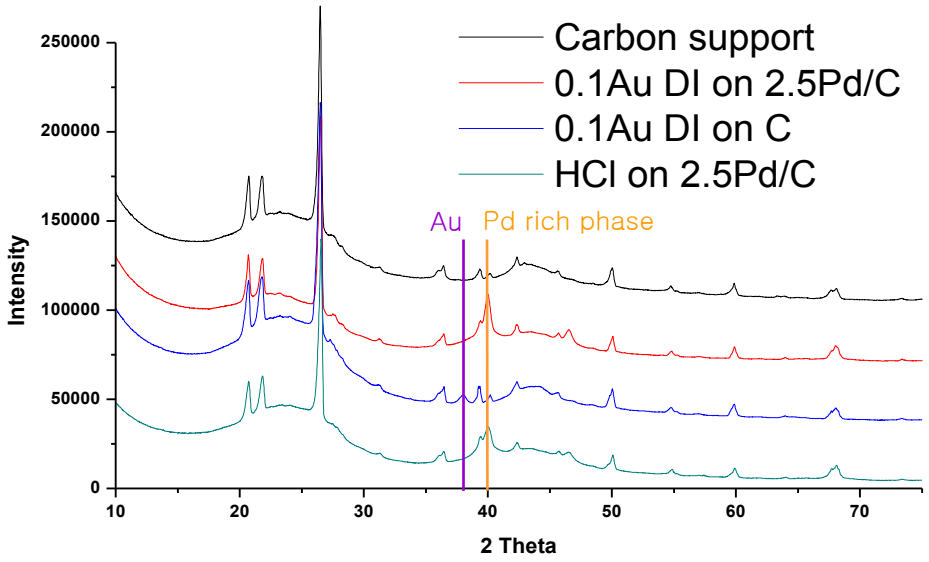

Figure 5.7. X-ray Diffraction patterns of 0.1wt% Au DI catalysts. Au and Pd (111) peaks are indicated.

hydrogenation process and this is not particularly affected by the preparation method. The catalysis results indicate the conversion activity enhancement is the main advantage of the SEA method.

Table 5.2 Selectivity table

	Selectivity (%)								
	Benzaldehyde			**Benzoic Acid**			**Toluene**		
Time (hour)	**0.5**	**1**	**1.5**	**0.5**	**1**	**1.5**	**0.5**	**1**	**1.5**
0.1 % Au-2.5 % Pd/C	66	59	45	2	15	31	30	24	21
0.5 % Au-2.5 % Pd/C	72	64	48	1	14	34	25	19	16
2.5 % Pd/C	75	69	57	2	11	27	21	18	13
2.5 % Au-2.5 % Pd/C	77	71	70	3	3	5	20	24	23

5.3 CONCLUSION

Sequential SEA is a simple method involving control of solution pH to achieve well dispersed core metal particles followed by selective adsorption of a second metal onto the first metal oxide. The approach is inherently applicable to commercially viable, high surface area support materials. The rational synthesis of bimetallic metal particles by sequential strong electrostatic adsorption can dramatically improve catalyst reactivity; in this case, raising activity of Pd/Au/C for benzyl alcohol oxidation by more than a factor of ten with 25 times less gold. Intimate contact of metals also results in more effective utilization of the metals, which is critical for expensive noble metals such as gold and palladium.

REFERENCES

[1] Davis B.H., Ertl G., Knozinger H., Weitkamp J., Handbook of Heterogeneous Catalysis, 1997

[2] Brunelle, J. P., Preparation of catalysts by metallic complex adsorption on mineral oxides, *Pure Appl. Chem*. 50, 1978, 1211

[3] Heise, M.S., and Schwarz, J.A., Preparation of metal distributions within catalyst supports 1. Effect of pH on catalytic metal profiles, *J. Coll. Interf.Sci*. 107, 1985, 51

[4] Heise, M.S., and Schwarz, J.A., Preparation of metal distributions within catalyst supports 2. Effect of ionic strength on catalytic metal profiles, *J. Coll. Interf.Sci*. 113, 1986, 55

[5] Heise, M.S., and Schwarz, J.A., Preparation of metal distributions within catalyst supports 3. Single component modeling of pH, ionic strength, and concentration effects, *J. Coll. Interf. Sci*. 123, 1988, 237

[6] Schwarz, J.A., Heise, M.S.,Preparation of metal distributions within catalyst supports: IV. Multicomponent effects, *J. Colloid Interface Sci*. 135, 1990, 461-467

[7] Park, J., Regalbuto, J.R., A simple, accurate determination of oxide PZC and strong buffering effect of oxide sufaces at incipient wetness, *J. Colloid Interface Sci*. 175, 1995, 239-252

[8] Surface and Nanomolecular Catalysis, Chapter 6: A Scientific Method to Prepare Supported Metal Catalysts, Richards, R. editor, Taylor and Francis/CRC Press, 2006

[9] Schreier, M., and Regalbuto, J.R., A Fundamental Study of Pt Ammine Impregnation of Silica 1. The Electrostatic Nature of Pt Adsorption, *J. Catal*.225, 2004, 190

[10] Hao, X., and Regalbuto, J. R., A Further Simplification of the Revised Physical Adsorption (RPA) Model*, J. of Colloid Interface Sci*. 267, 2003, 259

[11] Agashe, K.B. and J.R. Regalbuto,A Revised Physical Theory for Adsorption of Metal Complexes at Oxide Surfaces, *J. Colloid Interface Sci*. 185, 1997, 174-189

[12] Silvana Braun, Lucia G. Appel, Vera L. Camorim, and Martin Schmal, Thermal spreading of MoO_3 onto Silica supports, *J. Phys. Chem. B*, 2000, *104*, 6584-6590

[13] S. Noh, J. A. Schwarz, Estimation of the point of zero charge of simple oxides by mass titration, *J. Colloid Interface Sci*.130, 1989, 157-164

[14] Malini Pasupong, Master thesis 2011, University of Illinois at Chicago

[15] Jiao, L., and Regalbuto, J.R., The Synthesis of Highly Dispersed Noble and Base Metals on Silica via Strong Electrostatic Adsorption: I. Amorphous Silica, *J. Catalysis* 260, 2008, 329

[16] Jiao, L., and Regalbuto, J.R., The Synthesis of Highly Dispersed Noble and Base Metals on Silica via Strong Electrostatic Adsorption: II. Mesoporous Silica, *J. Catalysis* 260, 2008, 342

[17] T. E Feltes, L. Espinosa-Alonso, E. de Smit, L. D'Souza, R. J. Meyer, B. M Weckhuysen, J. R. Regalbuto , Selective Adsorption of Manganese onto Cobalt for Optimized Mn/Co/TiO2 Fischer-Tropsch Catalysts, *J. Catalysis* 270, 2010, 95

[18] D'Souza, L., Regalbuto, J.R., Miller, J.T., and Kropf, A.J., Preparation of silica- and carbon-supported cobalt by electrostatic adsorption of Co(III) hexaammines*, J. Catalysis*, 248, 2007, 165

[19] D'Souza, L., Regalbuto, J.R., and Miller, J.T., Preparation of carbon supported cobalt by electrostatic adsorption of [Co(NH3)6]Cl3*, J. Catalysis* 254, 2008, 157

[20] Catalyst Preparation: Science and Engineering, Chapter 13: Strong Electrostatic Adsorption of Metals onto Catalyst Supports, Regalbuto, J.R., ed., Taylor and Francis/CRC Press, 2007

[21] Schreier, M., Timmons, M., Feltes, T., and Regalbuto, J.R., The Determination of Surface Charging Parameters for a Predictive Metal Adsorption Model, *J. Colloid Interface Sci.* 348, 2010, 571

[22] Hao, X., and Regalbuto, J.R., Method for Preparing Highly Loaded, Highly Dispersed Platinum Metal on a Carbon Substrate, U.S. Patent 7,312,174, filed Sept. 9, 2003, issued December 25, 2007

[23] Park, C., Fenter, P., Sturchio, N., and Regalbuto, J.R., Probing outer-sphere adsorption of aqueous metal complexes at the oxide-water interface with resonant anomalous x-ray reflectivity, *Physics Review Letters* 94, 2005, 076104/1

[24] J. S. Noh, J. A. Schwarz, Estimation of surface ionization constants for amphoteric solids, *J. Colloid Interface Sci*. 1990, *139*, 139-148

[25] S. Subramanian, J.S. Noh, J.A. Schwarz, Determination of the point of zero charge of composite oxides, *J. Catalysis* 114, 1988, 433-439

[26] Job, N., Lambert, S., Preparation of highly loaded Pt/carbon xerogel catalysts for Proton Exchange Membrane fuel cells by Strong Electrostatic Adsorption method, *Catalysis Today* 150, 2010, 119-127

[27] Zhao, Y., Feltes, T. E., Regalbuto, J.R., R. J. Meyer, Klie, R., An analytical scanning transmission electron microscopy study of the support effects on Mn-promoted Co Fisher-Tropsch catalysts, *Catalysis Science&Technology* 1, 2011, 1483-1489

[28] Beard, K.D., Van Zee, J.W., and Monnier, J.R., Preparation of carbon-supported Pt-Pd electrocatalysts with improved physical properties using electroless deposition methods, *Appl. Catal. B Env*. 88, 2009, 185

[29] Alayoglu, S., Nilekar, A., Ru-Pt core-shell nanoparticles for preferential oxidation of carbon monoxide in hydrogen, *Nature Materials* 7, 2008, 333-338

[30] Alayoglu, S., Eichhorn, B., Rh-Pt bimetallic catalysts: Synthesis, characterization, and catalysis of core-shell, alloy, and monometallic nanoparticles, *J. Am. Chem. Soc.* 3, 2008, 810-815

[31] Smolentseva, S., Kusema, B., Selective oxidation of arabinose to arabinonic acid over Pd-Au catalysts supported on alumina and ceria, *Appl. Catal. A: Gen*. 392, 2011, 69-79

[32] Hao, X., Quach, L., Korah, J.,andRegalbuto, J. R., The Engineering of Pt Impregnation onto Oxides and Carbon*, J. Molecular Catalysis* 219, 2004, 97

[33] Castellazzi, P., Groppi, G., Forzatti, P., Effect of Pt-Pd ratio catalytic acitivity and redox behavior of bimetallic Pt-Pd/Al_2O_3 catalysts for CH_4 combustion, *Appl. Catal. B:Env*. 95, 2010, 303-311\

[34] Nomura, K., Noro, K., Pd-Pt bimetallic catalyst supported on SAPO-5 for catalytic combustion of diluted methane in the presence of water vapor, *Catalysis Letters* 53, 1998, 167-169

[35] Persson, K., Ersson A., Cataltic combustion of methane over bimetallic Pd-Pt catalysts: The influence of support materials, *Appl. Catal. B:Env*. 66, 2006, 175-185

[36] Micheaud, C., Marecot, P., Preparation of alumina supported Pd-Pt catalysts by surface redix reactions. Activity of complete hydrogen oxidation, *Appl. Catal. A:Gen*. 171, 1998, 229-239

[37] Strobel, R., Grunwaldt, J.D., Flame-made alumina supported Pd-Pt nanoparticles:structural properties and catalytic behavior in methane combustion, *Catalysis Letters* 104, 2005, 9-15

[38] Lapisardi, G., Urfels, L., Superior catalytic be havior of Pt-doped Pd catalysts in the complete oxidation of methane at low templerature, *Catalysis Today* 117, 2006, 564-

568

[39] Deganello, G., Duca, D., Pumice-supported Pd-Pt bimetallic catalysts:Synthesis, structural characterization, and liquid-phase hydrogenation of 1,3-cyclooctadiene, *J. Catalysis* 151, 1995, 125-134

[40] Castillo, N., Perez, R., Structural analysis of Pt-Pd nanoparticles dispersed on titanium dioxide to evaluate cyclo-olefines reactivity, *J. Alloys and Compounds* 495, 2010, 453-457

[41] Guillon, E., Lynch, J., Charcterization of bimetallic Pt systems:application to the reduction of aromatics in presence of sulfur, *Catalysis Today* 65, 2001, 201-208

[42] Fujikawa, T., Idei, K., Ohki, K., Mizuguchi, H., and Usui, K., Kinetic behavior of hydrogenation of aromatics in diesel fuel over silica-alumina-supported bimetallic Pt-Pd catalyst, *Appl. Catal. A Gen*. 205, 2001, 71

[43] Jan, C., Lin, T., Aromatics reduction over supported Pt catalysts. 3. Efeects of catalysts precursors and pretreatment conditions on the performance of Pd-promoted Pt catalysts, *Ind. Eng. Chem. Res.* 35, 1996, 3893-3898

[44] Lee., J., Rhee, H., Sulfur tolerance of zeolite beta-supported Pd-Pt catalysts for the isomerization of n-Hexane*, J. Catalysis* 177, 1998, 208-216

[45] Blomsma, E., Martens, J.A., Isomerization and hydrocracking of heptane over bimetallic bifunctional Pt/Pd H-beta and PtPd/USY zeolite catalysts, *J. Catalysis* 165, 1997, 241-248

[46] Loiha, S., Fottinger, K., Catalytic enhancement of Pt supported on zeolite beta for toluene hydrogenation by addition of Pd, *J. Industrial and Engineering Chem*. 15, 2009, 819-823

[47] Jongpatiwut, S., Li, Z., Competitive hydrogenation of poly-aromatic hydrocarbons on sulfur-resistance bimetallic Pt-Pd catalysts, *Appl. Catal. A: Gen*. 262, 2004, 241-253

[48] Pawelec, B., Mariscal, R., Hydrogenation of aromatics over supported Pt-Pd catalysts, *Appl. Catal.A: Gen.* 225, 2002, 223-237

[49] Navarro, R.M., Pawelec, B., Hydrogenation of aromatics on sulfur-resistance Pt-Pd bimetallic catalysts, *J. catalysis* 189, 2000, 184-194

[50] Elangovan, S.P., Bischof, C., Isomerization and hydrocracking of n-decane over bimetallic Pt-Pd clusters supported on mesoporous MCM-41 catalysts, *Catalysis Letters* 80, 2002, 35-40

[51] Kim, H.S., Kim, T.W., Koh, H.L., Lee, S.H., and Min, B.R., Complete benzene

oxidation over Pt-Pd bimetal catalyst supported on γ-alumina: influence of Pt-Pd ration on the catalytic activity, *Appl. Catal. A Gen*. 280, 2005, 125

[52] Yu, Z., Liao, S., Hydrogenation of nitroaromatics by polymer-anchored bimetallic Pd-Ru and Pd-Pt catalysts under mild conditions*, J. Molecular Catal. A: Chem.* 120, 1997, 247-255

[53] Sharma, R., Zhou, B., Catalytic destruction of volatile organic compounds using supported Pt and Pd hydrogphobic catalysts, *Ind. Eng. Chem. Res*. 34, 1995, 4310-4317

[54] Papageorgopoulos, D.C., Keijzer, M., CO tolerance of Pd-rich Pt Pd carbon-supported electrocatalysts, *J. Electrochem. Soc*. 149, 2022, A1400-1404

[55] Ji, X., Lee, K., Nanocrystalline intermetallics on mesoporous carbon for direct formic acid fuel cell anodes, *Nature Chemistry* 2, 2010, 286-293

[56] Masato Ohashi, Kevin D. Beard, Shuguo Ma, Douglas A. Blom, Jean St-Pierre, John W. Van Zee, John R. Monnier, Electrochemical and structural characterizationof carbon-supported Pt–Pdbimetallic electrocatalysts prepared by electroless deposition, *ElectrochimicaActa* 55, 2010, 7376–7384

[57] Liu, C., Shao, Z., Hydrodeoxygentaion of benzofuran over silica-alumina supported Pt,Pd, and Pt-Pd catalysts, *Energy Fuels* 26, 2012, 4205-4211

[58] Roucoux, A., Schulz, J., and Patin, H., Reduced transition metal colloids: a family of reusable catalysts?, *Chem. Rev*. 102, 2002, 3757

[59] Bonnemann, H., and Richards, R. M., Nanoscopic metal particles – synthetic methods and potential applications, Eur. *J. Inorg. Chem*. 2001, 2455

[60] Scott, R. W. J., Wilson, O. M., and Crooks, R. M., Synthesis, characterization, and applications of dendrimer-encapsulated nanoparticles, *J. Phys. Chem. B* 109, 2005, 692

[61] Peng, X., Pan, X., and Rempel, G.L., Bimetallic dendrimer-encapsulated nanoparticles as catalysts: a review of the research advances, *Chem. Soc. Rev*., 37, 2008, 1619

[62] Liu, D.X., Lopez-de Jesus, Y.M., Monnier, J.R., and Williams, C.T., Preparation , characterization, and kinetic evaluation of dendrimer-derived bimetallicfPt-Ru/SiO2 catalysts, *J. Catalysis* 269, 2010, 376

[63] Kulp, C., Chen, X., Puschof, A., Schwamborn, S., Somsen, C., Schuhmann, W., and Bron, M., Electrochemical synthesis of core-shell catalysts for electrocatalytic applications, *ChemPhysChem* 11, 2010, 2854

[64] Rebelli, J., Detwiler, M., Ma, Synthesis and characterization of Au-Pd bimetallic catalysts prepared by electroless deposition, *J. Catalysis* 270, 2010, 224

[65] Espinosa, G., Del Angel, G., Barbier, J., Bosch, P., lara, V., and Acosta, D., Catalytic behavior and active sites structure of PtAu/Al2O3 bimetallic catalysts prepared by surface redox reactions, *J. Molc. Catal. A. Chem*. 164, 2000, 253

[66] E. Kratzer. Thesis 2006. The Synthesis of Carbon Supported Palladium Catalysts by Strong Electrostatic Adsorption. In Chemical Engineering.Univeristy of Illinois at Chicago, Chicago

[67] Moralng, A., Neuhausen, U., Bimetallic Pt/Pd diesel oxidation catalysts structural characterization and catalytic behavior, *Appl. Catal. B: Env*. 60, 2005, 191-199

[68] Mori, K., Hera, T., Hydroxyapatite-supported Pd nanocluster: a highly active heterogeneous catalyst for selective oxidation of alcohols by use of molecular oxygen, *J. Am. Chem. Soc*. 126, 2004, 10657-10666

[69] Meenakshisundaram, S., Nowicka, E., Oxidation of alcohols using supported Au and Au-Pd nanoparticles*, Faraday Discuss*. 145, 2010, 341-356

[70] Schultz, M., Adler, R., Using mechanistic and computational studies to explain ligand effects in the Pd-catalyzed aerobic oxidation of alcohols, *J. Am. Chem. Soc*. 127, 2205, 8499-8507

[71] Dimitratos, N., Lopez-Sanchez, J.A., Solvent free liquid phase oxidation of benzyl alcohol using Au supported catalysts prepared using a sol immobilization technique, *Catalysis Today* 122, 2007, 317-324

[72] Lopez-Sanchez, J.A., Dimitratos, N., Reactivity studies of Au-Pd supported nanoparticles for catalytic applications, *Appl. Catal. A:Gen*., 391, 2011, 400-406

[73] Tiruvalam, R.C., Pritchard, J.C., Aberration corrected analytical electron microscopy studies of sol-immobilized Au+Pd, Au{Pd} and Pd{Au} catalysts used for benzyl alcohol oxidation and hydrogen peroxide production, *Faraday Discussions* 152, 2011, 63-86

[74] Sheldon, R.A., Arends, I.W.C.E., New developments in catalytic alcohols oxidations for fine chemicals synthesis, *Catalysis Today* 57, 2000, 157-166

[75] Nishimura, T., Onoue, T., Pd(OAc)2-catalyzed oxidation of alcohols to aldehydes and ketones by molecular oxygen, *Tetrahedron Letters* 39, 1998, 6011-6014

[76] Ferreira, Eric., Stoltz, B., The Pd-catalyzed oxidative kinetic resolution of secondary alcohols with molecular oxygen, J. Am. Chem. Soc. 123, 2001, 7725-7726

[77] Wang, X., Wu, G., Supported Pd catalysts for solvent-free benzyl alcohols selective

oxidation: Effects of calcination pretreatments and reconstruction of Pd sites, *Appl. Catal. B:Env*. 115-116, 2012, 7-15

[78] Conley, N., Labios, L., Aerobic alcohol oxidation with cationic Pd complexes:Insights into catalyst design and decomposition, *Organometallics* 26, 2007, 23

[79] Hughes, m., Xu, Y., Tunable Au catalysts for selective hydrocarbon oxidation under mild conditions, *Nature* 437, 2005, 1132-1135

[80] Chen, M., Kumar, D., The promotional effect of Au in catalysis by Pd-Au, *Science* 310, 2005, 291-293

[81] Echae, D., Edwards, J., Solvent-free oxidation of primary alcohols to aldehydes using Au-Pd/TiO2 catalysts, *Science* 311, 2206, 362-365

[82] Chen, Y., Wang, H., Formation of monometallic Au and Pd and bi,etallic Au-Pd nanoparticles confined in mesopores via Ar glow-discharge plasma reduction and their catalytic applications in aerobic oxidation of benzyl alcohol, *J. Catalysis* 289, 2012, 105-117

[83] Dimitratos, N., Villa, A., Pd and Pt catalysts modified by alloying with Au in the selective oxidation of alcohols, *J. Catalysis* 244, 2006, 113-121

[84] Miedziak, P., Sankar, M., Oxidation of benzyl alcohol using supported Au-Pd nanoparticles, *Catalysis Today* 164, 2011, 315-319

[85] Edwards, J., Edwin Ntainjua N, Direct synthesis of H_2O from H_2 and O_2 over Au, Pd, and Au-Pd catalysts supported on acid-pretreated TiO2, *Angew. Chem. Int. Ed*. 48, 2009, 8512-8515

[86] Pritchard, J., He, Q., The effect of catalyst preparation method on the performance of supported Au-Pd catalysts for the direct synthesis of hydrogen peroxide, *Green Chemistry* 12 , 2010, 915-921

[87] Edwards, J., Solsona, B., Switching off hydrogen peroxide hydrogenation in the direct synthesis process, *Scienc*e 323, 2009, 1037-1041

[88] Hutchings, Graham. J., Supported Au and Au-Pd catalysts for selective synthesis, *Catalysis Today* 138, 2008, 9-14

[89] Edwin Ntainjua N, Piccinini, M., Efeect of halide and acid additives on the direct synthesis of hydrogen peroxide using supported Au-Pd catalysts, *ChemSusChem* 2, 2009, 575-580

[90] Piccinini, M., Edwin Ntainjua N, Effect of reaction conditions on the performance of Au-Pd/TiO2 catalyst for the direct synthesis of hydrogen peroxide, *Phys. Chem.*

Chem. Phys. 12, 2012, 2488-2492

[91] Edwards, J., Hutchings, G. J., Pd and Au-Pd catalysts for the direct synthesis of hydrogen peroxide, *Angew. Chem. Int. Ed*. 47, 2008, 9192-9198

[92] Toshima, N., Harada, M., Catalytic activity and structural analysis of polymer-protected Au-Pd bimetallic clusters prepared by the simultaneous reduction of HAuCl4 and PdCl2, *J. Phys. Chem* 96, 1992, 9927-9933

[93] Krishnankutty, N., Vannice, A., The effect of pretreatment on Pd/C catalysts, *J. Catalysis* 155, 1995, 312-326

[94] C. Hwang, C. Yeh, Platinum-oxide species formed by oxidation of platinum crystallites supported on alumina, *J. Molecular Catalysis A: Chem*. 112, 1996, 295-302